DISSERTATIONS IN
FORESTRY AND
NATURAL SCIENCES

MIKAEL TURUNEN

Spectroscopic Characterization of Bone Composition

Alterations during Bone Formation, Maturation and Aging

PUBLICATIONS OF THE UNIVERSITY OF EASTERN FINLAND
Dissertations in Forestry and Natural Sciences

UNIVERSITY OF
EASTERN FINLAND

MIKAEL TURUNEN

Spectroscopic Characterization of Bone Composition

Alterations during Bone Formation, Maturation and Aging

Publications of the University of Eastern Finland
Dissertations in Forestry and Natural Sciences
No 118

Academic Dissertation
To be presented by permission of the Faculty of Science and Forestry for public examination in the Auditorium L1 in Canthia Building at the University of Eastern Finland, Kuopio, on September, 6, 2013,
at 12 o’clock noon.

Department of Applied Physics

Kopijyvä
Kuopio, 2013
Editor: Prof. Pertti Pasanen, Prof. Pekka Kilpeläinen
Prof. Kai Peiponen, Prof. Matti Vornanen

Distribution:
University of Eastern Finland Library / Sales of publications
P.O. Box 107, FI-80101 Joensuu, Finland
tel. +385-50-3058396
http://www.uef.fi/kirjasto

ISBN: 978-952-61-1194-0 (printed)
ISSNL: 1798-5668
ISSN: 1798-5668
ISBN: 978-952-61-1195-7 (pdf)
ISSNL: 1798-5668
ISSN: 1798-5676

Author's address:
University of Eastern Finland
Department of Applied Physics
P.O.Box 1627
70211 KUOPIO
FINLAND
email: mikael.turunen@uef.fi

Supervisors:
Adjunct Professor Hanna Isaksson, Ph.D.
University of Eastern Finland
Department of Applied Physics
email: hanna.isaksson@solid.lth.se

Professor Jukka Jurvelin, Ph.D.
University of Eastern Finland
Department of Applied Physics
email: jukka.jurvelin@uef.fi

Reviewers:
Henrik Birkedal, Ph.D.
Aarhus University
Department of Chemistry
Langelandsgade 140
8000 Aarhus C
Denmark
email: hbirkedal@chem.au.dk

Eleftherios Paschalis, Ph.D.
Ludwig Boltzmann Institute of Osteology
Hanusch Hospital
Heinrich Collin-Str. 30
A-1140 Vienna
Austria
email: eleftherios.paschalis@osteologie.at

Opponent:
Professor Marjolein van der Meulen, Ph.D.
Cornell University
Department of Mechanical and Aerospace Engineering
219 Upson Hall
Ithaca, NY 14853
United States of America
email: MCV3@cornell.edu

ABSTRACT

Bone has a complex hierarchical structure and its shape, composition and architecture constantly change, not only during bone maturation processes and aging, but also in response to altered mechanical loading. Thus, bone is a dynamic tissue exhibiting continuous changes in its quality.

In this thesis, the normal maturation and age related changes in molecular composition, collagen architecture and trabecular bone microarchitecture were evaluated using several quantitative techniques. Fourier transform infrared (FTIR) and Raman microspectroscopy techniques as well as biochemical analysis were used to characterize the composition of cortical rabbit bone from the newborn stage until skeletal maturity was reached. Polarized light microscopy (PLM) was used to assess the collagen fiber organization in the tissue. Additionally, differences between composition and microarchitecture of trabecular bone in the human femoral neck, trochanter major and calcaneus were studied. Furthermore, FTIR and small angle X-ray scattering (SAXS) were used to determine the composition and mineral structure, *i.e.* mineral plate thickness, pre-dominant orientation and degree of orientation, in rat femur fracture callus with these parameters being compared to the surrounding cortical bone. Finally, parameters from different techniques that reflected the same characteristics, *e.g.* FTIR vs Raman, or that provided complementary information, *e.g.* FTIR and SAXS, were comprehensively compared.

The spectroscopic techniques could describe the rapid compositional changes during early maturation of bone, *e.g.* increase in collagen content and mineralization. In human samples, bone tissue composition changed with age, however, after skeletal maturity a slower pace was recorded. The composition and microarchitecture varied between anatomical locations. This could be linked to differences in the loading environments. During fracture repair, mineralization, collagen maturity and degree of orientation were lower and acid phosphate substitution was higher in the callus tissue compared to the cortical bone, all indicators of an immature and less organized bone. Thus, FTIR and SAXS were sensitive techniques to assess the composition and mineral structure of newly formed bone tissue. The present results suggest that caution is required when similar parameters of bone composition from different techniques are compared.

In this thesis, specific age-related changes in composition, microarchitecture and mineral structure could be characterized. The normal changes related to maturation, aging and bone growth are important factors of bone quality. It is anticipated that the methods assessed in this thesis will be used in the future to improve the assessment of bone quality and to increase the understanding of characteristics of bone diseases, *e.g.* osteoporosis.

National Library of Medicine Classification: QT 36, WE 102, WE 200

Medical Subject Headings: Bone and Bones; Bone Development; Fractures, Bone; Bony Callus; Aging; Molecular Structure; Collagen; Minerals; Spectroscopy, Fourier Transform Infrared; Spectrum Analysis, Raman

Yleinen suomalainen asiasanasto: : luu; luunmurtumat; kehitys; kypsyminen; ikääntyminen; koostumus; rakenne; kollageenit; mineraalit; spektroskopia

To Minna & Eljas

Acknowledgements

This study was carried out during the years 2009-2013 in the Department of Applied Physics at the University of Eastern Finland.

I would like to express my gratitude to my supervisors for their professional guidance during this thesis project. I am grateful to my principal supervisor adjunct professor Hanna Isaksson for her creativity, ideas, endless hours helping me and being a mentor during the beginning of my research career. I would like to thank my second supervisor professor Jukka Jurvelin for providing me the opportunity to work in his top class research group, Biophysics of Bone and Cartilage (BBC).

I am grateful to the official reviewers of this thesis, associate professor Henrik Birkedal and Eleftherios Paschalis, for their professional review and encouraging comments. I would also like to thank Ewen MacDonald for linguistic review.

I would like to express my deepest gratitude to all of my coauthors for their significant contributions to the studies. Particularly, I want to thank Lassi Rieppo for his immeasurable help in spectroscopic analyses during my thesis project.

I want to thank everyone in BBC group. It has been a pleasure and a privilege to work under great stimulating atmosphere. Especially, I would like to thank Mika Mononen and Janne Mäkelä for endless shared studying hours, discussions and friendship. I would also like to thank my fellow students Jukka Lipponen and Jouni Pääkkönen for support during this project. I also want to express my gratitude to all my friends who have supported me during the past years.

I would like to acknowledge the staff of Department of Applied Physics, Department of Biomedicine and SIB Labs for their help during this project.

For financial support the strategic funding of University of East-

ern Finland, University of Eastern Finland grant (projects 5741, 61/627/2005, 25/627/2006), Academy of Finland (projects 127198, 113112, 213548, 216231, 200970, 1105595, 128863), the European Commission (projects 219980, FRACQUAL-293434), the Swedish Agency for Innovation Systems, the Swedish Research Council through the Linnaeus Center Organizing Molecular Matter, MAX IV laboratory, the Foundation of Greta and Johan Kock, Kuopio University Hospital (EVO project 5031342), Emil Aaltonen foundation and National Doctoral Programme of Musculoskeletal Disorders and Biomaterials (TBDP) are acknowledged.

I am grateful to my parents, Päivi and Heikki, my little brothers Patrik and Niklas for their continuous support, encouragement and love throughout my life.

Finally, I owe my deepest gratitude to my beloved Minna for endless love and understanding for the long working hours. And our little miracle Eljas, you always bring the smile on my face.

Kuopio, August 2013

Mikael Turunen

ABBREVIATIONS

APS	acid phosphate substitution
BA	biochemical analysis
BaF_2	Barium-Fluoride
BMD	bone mineral density
BMP	bone morphogenetic protein
BP	bisphosphonate
BV/TV	bone volume fraction
CCD	charge-coupled device
CT	X-ray computed tomography
C/M	carbonate/matrix ratio
C_B/M	type-B carbonate/matrix ratio
C/P	carbonate/phosphate ratio
C_B/P	type-B carbonate/phosphate ratio
CV%	coefficient of variation
D	direct
DA	degree of anisotropy
deH-DHLNL	dehydro-dihydroxylysinonorleucine
deH-HLNL	dehydro-hydroxylysinonorleucine
deH-HHMD	dehydro-histidinohydroxymerodesmosine
DoO	degree of orientation
dp	depolarizer
d-Pyr	deoxypyrisinoline
DXA	dual energy X-ray absorption
EDTA	ethylene diaminotetraacetic acid
FTIR	Fourier transform infrared
FWHM	full width at half maximum
HA	hydroxyapatite
HHL	histidinohyrdoxylysinonorleucine
HP	hydroxylysyl-pyridinoline
HPLC	high-pressure liquid chromatography
IR	infrared
mc	monochromator
M/M	mineral/matrix ratio

NA	numerical aperture
NaCl	Sodium chloride
p	polarizer
PBS	Phosphate buffered saline
PEN	pentosidine
PF	peak fitting
PI	parallelism index
PLM	polarized light microscopy
PMMA	polymethylmetacrylate
Pyr	pyridinoline
RMS	root mean square
ROI	region of interest
RPA	random phase approximation
SAXS	small angle X-ray scattering
SD	standard deviation
SMI	structural model index
T	mineral plate thickness
Tb.N	trabecular number
Tb.Sp	trabecular separation
Tb.Th	trabecular thickness
UV	ultraviolet
XLR	collagen cross-link ratio
XRD	X-ray diffraction
ZnSe	Zinc-Selenide
ZO	Zolendronate
µCT	micro-computed tomography

SYMBOLS AND NOTATIONS

A	absorbance or microscope specific constant
A_0	background area
A_1	sum area under two Gaussian curves
a & b	optical system specific constants
B	birefringence
C	scale factor
c	speed of light or molecule concentration
$D(T, T_{av})$	Schultz-Zimm distribution
E	energy of radiation
E_e	electronic energy of a molecule
E_v	vibrational energy of a molecule
E_r	rotational energy of a molecule
E_t	total energy of a molecule
$\vec{E}$	electric field
h	Planck constant
I	transmitted/penetrated/passed intensity
I_0	incident intensity
$I(q)$	1-dimensional scattering pattern
$I(q, \theta)$	2-dimensional scattering pattern
l	optical path length or section thickness
k	constant approximately equal to unity
N	total number of atoms in a system
n	number of samples
P	Porod constant
PI	parallelism index
$\vec{P}$	induced dipole moment
$\bar{p}$	electric dipole moment
$P(q)$	form factor
$P_{av}(q)$	average scattering
P_{frac}	effective structure factor

Q	electric charge or Porod invariant
q	q-range
$\bar{r}$	distance of the charge from a reference point
S_0	Stokes parameter, total intensity of light
S_1	Stokes parameter, amount of linear/horizontal polarization
S_2	Stokes parameter, amount of $+45^\circ$ or -45° polarization
S_3	Stokes parameter, amount of right or left circular polarization
$\frac{S}{V}$	total interfacial area per unit volume
T	transmittance or mineral plate thickness
t	time
x	distance travelled in matter
α	polarizability of a molecule or rotation angle or fractal dimension of fluctuations
λ	wavelength
μ	linear attenuation coefficient
ν	frequency or adjustable RPA parameter
$\bar{\nu}$	wavenumber
$\bar{\nu}_0$	wavenumber of incident radiation
$\bar{\nu}_M$	wavenumber of scattered radiation
ω	phase shift
$\Delta\rho$	scattering length density difference
σ	molecular absorption coefficient
ϕ	volume fraction or angle between polarizing axes
φ	degree of orientation
θ	diffraction angle
χ	scattering angle
Ψ	orientation angle of the polarization ellipse or scattering angle of maximum intensity

LIST OF PUBLICATIONS

This thesis consists of the review of the author's work in the field of medical physics. The following selections of the author's publications are referred to by the Roman numerals:

I M. J. Turunen, S. Saarakkala, L. Rieppo, H. J. Helminen, J. S. Jurvelin and H. Isaksson, "Comparison between infrared and Raman spectroscopy analysis of maturing rabbit cortical bone," *Applied Spectroscopy* **65(6)**, 595–603 (2011).

II M. J. Turunen, S. Saarakkala, H. J. Helminen, J. S. Jurvelin and H. Isaksson, "Age-related changes in organization and content of the collagen matrix in rabbit cortical bone," *Journal of Orthopaedic Research* **30(3)**, 435–442 (2012).

III M. J. Turunen, V. Prantner, J. S. Jurvelin, H. Kröger and H. Isaksson, "Composition and microarchitecture of human trabecular bone change with age and differ between anatomical locations," *Bone* **54**, 118–125 (2013).

IV M. J. Turunen, S. Lages, A. Labrador, U. Olsson, M. Tägil, J. S. Jurvelin and H. Isaksson, "Evaluation of composition and mineral structure of callus tissue in rat femoral fracture," Submitted for publication (2013).

The original articles have been reproduced with permission of the copyright holders. This thesis also contains previously unpublished data.

AUTHOR'S CONTRIBUTION

The publications selected to this dissertation are original research papers on spectroscopic characterization on bone composition. The author has contibuted to the study design and development of spectral analysis and carried out all measurements and analyses, except for the biochemical analyses and micro-computed tomography imaging. The author was the main writer in all studies.

Contents

1 Introduction

The shape, architecture and composition of bone tissue are constantly changing during maturation and aging and in response to altered mechanical loading due to the naturally occurring process of bone formation, modeling and remodeling [1–7]. The composite of collagen fibers and minerals together with the geometry confer on bone its remarkable mechanical properties to withstand high compressive, tensile and shear stresses [8,9]. The skeleton provides the body with its integrity, protects the internal organs and maintains the mineral ion homeostasis of the body [6, 7]. The shape, architecture, composition and mechanical properties all contribute to the bone quality.

Bone tissue is constantly changing during maturation and aging as the shape, microarchitecture and composition are altered in response to mechanical stimuli [2, 3]. The modeling and remodeling of bone are driven by bone resorbing cells, *i.e.* osteoclasts, and bone forming cells, *i.e.* osteoblasts [1,2,7]. Together they try to optimize the bone structure and composition to withstand the stresses experienced by bone during daily actions. Naturally, the mechanical loading of different anatomical locations is different and consequently the microarchitecture and composition is also believed to vary [10].

Bone fracture healing mechanisms are similar to those encountered in bone development [11, 12]. Callus formation is a critical step in fracture healing [12]. Different treatments can be used to to manipulate the cell functions. Bone morphogenetic proteins (BMPs) increase callus formation [13–15], whereas bisphosphonates (BPs) are used to reduce the resorption of bone as these drugs inhibit osteoclast activity [13, 16]. However, these manipulations of the modeling and remodeling may alter the quality of the forming bone.

Bone composition has traditionally been studied using biochemical analysis (BA). Lately, alternative methods like Fourier Transform infared (FTIR) and Raman microspectroscopic techniques have been increasingly used to assess the composition of bone [17–36]. The major advantage of these microspectroscopic techniques is the relatively fast simultaneous spatial analysis of the organic and inorganic composition of bone. The parameters calculated from the infrared (IR) or Raman spectra provide diverse information *e.g.* about mineralization, carbonate substitution, collagen maturity, crystallinity and acid phosphate substitution (APS). These parameters have been shown to alter with age [17, 21, 24, 30–39]. In brief, mineralization, carbonate substitution and collagen maturity increase and APS decreases with aging.

The structure and microarchitecture of bone can be evaluated by a variety of methods. Polarized light microscopy (PLM) can be used to assess the collagen architecture of biological tissue like articular cartilage and bone [3, 40–50]. This technique provides information about the orientation and anisotropy of the collagen fibers. Micro-computed tomography (μCT) has been used to evaluate the microarchitecture of trabecular bone [51–62]. The analysis of the reconstructed images yields metric indices of the trabecular structure, *e.g.* bone volume fraction and thickness of the trabeculae [51, 55, 60, 61, 63]. Mineral structure, *e.g.* size of the mineral particles, can be assessed using small angle x-ray scattering (SAXS) [64–68] and x-ray diffraction (XRD) [69–71] techniques. For example, the size of the mineral particles increases with age [69,70].

In this thesis, age-related changes in bone composition and collagen structure were characterized using BA, FTIR and Raman microspectroscopic techniques and PLM. FTIR and Raman microspectroscopic techniques provide similar but complementary information about the composition of bone. The parameters obtained with both techniques were compared and the reason for agreement or discrepancies was discussed extensively. Additionally, μCT and FTIR microspectroscopy were used to compare the trabecular bone structure and composition, respectively, in human femoral neck, greater trochanter and calcaneus. Moreover, the composition and mineral structure of newly formed callus tissue and intact cortical bone were characterized and compared. In summary, this thesis presents an extensive characterization of bone composition and structure and their changes during maturation, aging and fracture healing. These characteristics provide valuable information about bone quality and its natural changes.

2 Bone

Bone has a complex hierarchical structure [1,2,6,7]. Its architecture, shape and composition are constantly changing during the natural process of bone formation, modeling and remodeling [1–7] where the latter is present throughout life.

2.1 BONE STRUCTURE

Bones can generally be classified into three groups: short, flat and long bones [1]. Short bones have relatively thin cortices and have an uniform size in all directions, *e.g.* vertebral bodies. In flat bones, one dimension is much shorter or longer than the other two, *e.g.* scapula or lamina of a vertebra. Long bones are mainly found in the limbs, *e.g.* femur, tibia and humerus. They have a thick cortical bone wall and the metaphysis and epiphysis are expanded. In mature bones, the bone tissue and the periosteum support the fatty or hematopoietic marrow inside the bone [1]. The vascular system supplies the cells of the marrow, bone tissue and the periosteum with blood and nutrients. It is so elaborate that no cell in any bone type lies more than 300 μm from a blood vessel [1,72,73].

2.1.1 Bone types

Bone can be divided into two types: cortical and trabecular bone (Figure 2.1). These can be further divided into woven and lamellar bone.

CORTICAL BONE

Cortical bone is dense and compact (4-8 % porosity) and surrounds the bone marrow and the trabecular bone, and it accounts for approximately 80 wt% of the mature skeleton [1,6]. In long bones, the cortical bone forms the diaphysis and the thick cortical walls be-

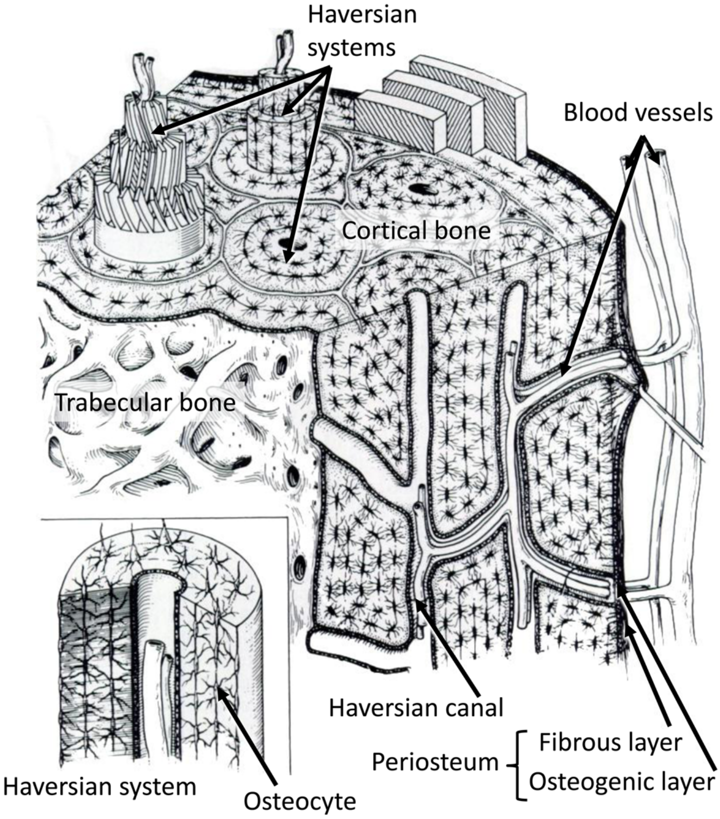

Figure 2.1: Schematic presentation of bone structure, showing the lamellar cortical and trabecular bone, Haversian system, periosteum and blood vessels. (Modified from [1].)

come thinner as they form the metaphysis which consists of tightly packed Haversian systems, *i.e.* osteons, with a central Haversian canal (Figure 2.1). Blood vessels, lymphatic vessels and nerves are formed inside the Haversian systems and supply the cells in cortical bone with nutrients. Bone grows outwards from the osteon like the annual rings in wood. Haversian systems are found in humans and many other higher order species, but do not exist in all small animals, *e.g.* rats [74].

TRABECULAR BONE

Trabecular (or cancellous) bone is a sponge-like bone tissue that has much lower density than cortical bone (50-90 % porosity) (Figure 2.1) [1, 6]. Trabecular bone is formed from individual trabeculae that can be roughly divided into rod-like and plate-like trabeculae (Figure 2.2). Trabecular bone is constantly changing when the architecture adapts to the loading to which the bone is subjected [1, 6, 7, 75]. Trabecular bone has a higher rate of metabolic activity than cortical bone due to its larger surface to volume ratio. Thus the response to a mechanical stimulus occurs much more rapidly than in cortical bone.

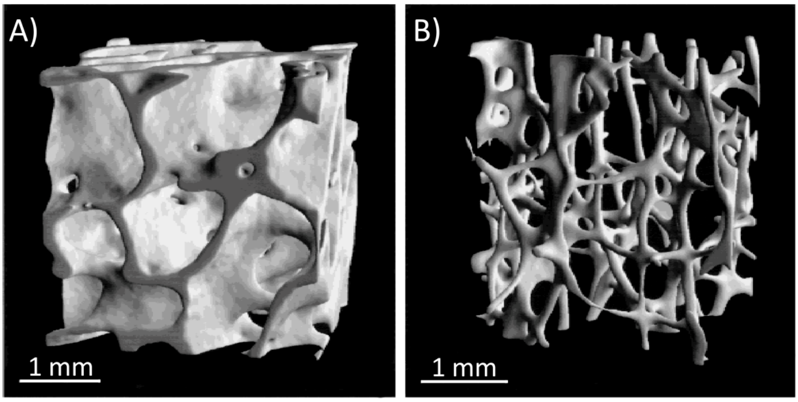

Figure 2.2: Reconstructed μCT images of trabecular bone with mainly plate-like (femur head) A) and rod-like (lumbar spine) trabeculae B). (Adapted from [57], with permission of John Wiley & Sons.)

WOVEN AND LAMELLAR BONE

Woven (primary, immature) and lamellar (secondary, mature) bone can be found in cortical and trabecular bone [1]. Woven bone has a high turnover rate and a less organized structure; it has an irregular pattern of collagen fibrils and its mineralization is more random. Furthermore, the osteocyte (and water) content is higher in woven bone than in lamellar bone which promotes rapid bone formation.

As bone matures, the woven bone becomes replaced by lamellar bone. Lamellar bone is less active than woven bone. Lamellar bone has a regular structure of collagen fibers and mineralization is well organized. This makes the lamellar bone stronger and stiffer than woven bone. The remodeling from woven to lamellar bone plays an important role in fracture healing *i.e.* the initially formed woven bone in the fracture callus is slowly replaced with lamellar bone.

Periosteum

Periosteum covers the external surfaces of bones (Figure 2.1). It has an important role in the blood supply of the bone. The outer layer of the periosteum is dense and fibrous, whereas the inner layer is more vascular and contains cells that can differentiate into osteoblasts. In younger bones, the periosteum is thicker but it becomes thinner with increasing age and thus the osteogenic capacity decreases [1].

2.1.2 Bone cells

Bone cells are responsible for bone formation, resorption, repair of the bone and the control of the mineral homeostasis in the body [1, 7]. These functions are sustained by specialized forms of bone cells that differ in both their morphology and characteristics. The bone forming cells differentiate from mesenchymal stem cells, whereas the bone resorbing cells originate from hematopoetic stem cells [1,7]. The complex network of cells covering the bone surfaces is sensitive to stresses, and mechanical loading stimulates the remodeling and formation of bone [1,7].

Osteoblasts

Osteoblasts are the main bone forming cells [1,7]. They are located on the surface of bone. The main function of osteoblasts is to synthesize new organic matrix of bone but they may also influence the mineralization of the bone matrix. Active osteoblasts can have three fates 1) remain on the bone surface and become bone lining cells, 2) surround themselves with bone matrix and become osteocytes, or 3) disappear from the bone formation site. The bone lining cells are flattened against the bone matrix, whereas osteocytes are embedded into the organic matrix [1,7].

OSTEOCYTES

In the mature human skeleton, more than 90 % of bone cells are osteocytes [1]. They are surrounded with an organic matrix. Osteocytes have a single nucleus and long branching cytoplasmic processes that make contacts with the cytoplasmic processes from other cells (Figure 2.1).

OSTEOCLASTS

Osteoclasts are the main bone resorbing cells. They are multinucleated (3-20 nuclei) with large numbers of mitochondria and lysosomes [1,7]. They participate in the remodeling of bone by resorbing bone tissue and are responsible for creating osteonal resorption cavities (Haversian canals). The high number of mitochondria provide the cells with the necessary energy they require to resorb bone. Osteoclasts bind to the surface of bone, creating a sealed space between the cell and the bone matrix. Then proton-pumps transport protons into the sealed space decreasing the pH which dissolves the bone mineral. The remaining organic matrix is then degraded when the cell secretes acid proteases [1,7].

2.2 BONE COMPOSITION

Bone matrix consists of organic, primarily collagen, and inorganic, *i.e.* hydroxyapatite (HA), components. Over 90 % of the volume of the bone tissue is made up of this matrix [1,6,7,76] with the remainder being made up of cells, blood vessels and water [1]. In brief, the collagen in the organic matrix confers bone with its form, whereas the minerals in the inorganic matrix makes the bone stiff. Together these components determine the biomechanical properties and functional integrity of the bone.

2.2.1 Inorganic matrix

The inorganic matrix of bone serves as an ion reservoir and it occupies about 43 % of the bone volume. Most of the body's minerals can be found in bone; 99 % of calcium, 85 % of phosphorus and 40-60 % of sodium and magnesium [1, 6, 7]. Additionally, significant amounts of impurities like carbonate, phosphate, potassium, citrate and fluoride are also present [76]. The minerals in bone form plate-like or needle-like hydroxyapatite crystals ($Ca_{10}[PO_4]_6[OH]_2$) that also contain carbonate ions and hydrogen phosphate groups [1,7,76]. Thus, the biological apatite is calcium deficient. The composition of these crystals changes, *e.g.* the concentration of carbonate and phosphate increases as a function of the age of the crystal [1, 17, 30, 31, 38, 39]. This means that the biological functions of the crystals are dependent on both the amount of mineral present and the age of the crystals [1].

2.2.2 Organic matrix

The organic matrix of bone is a dense fibrous structure. It occupies about 32 % of the bone volume and approximately 90 % of the organic matrix is formed by type I collagen, accompanied by small amounts of type V and type XII collagens [1, 6, 7, 76, 77]. Non-collagenous glycoproteins and proteoglycans account for the remaining 10 % of the organic matrix. Type I collagen differs from the other collagen types, since it has a unique amino-acid content and relatively thick fibrils. Type II collagen also forms fibers, but is usually found in other tissues, *e.g.* articular cartilage. The non-collagenous proteins may influence the organization of the organic matrix as well as influencing the mineralization of bone [76] and the behavior of the bone cells. Additionally, the organic matrix also contains growth factors that have an important role in controlling bone-cell functions [1].

2.2.3 Collagen cross-links

Collagen cross-links form a complex system which are important for the functional integrity of the tissue [77]. These are formed between collagen fibers as they link the collagen fibers to each other [77]. They can be roughly divided into mature and immature, and enzymatic and non-enzymatic cross-links. Enzymatic cross-links are formed by catalysis of an enzyme whereas non-enzymatic cross-links are formed spontaneously. Immature cross-links can be reduced to mature cross-links either through catalysis of an enzyme or without enzymatic intervention. The major enzymatic cross-links found in type I collagen are dehydro-dihydroxylysinonorleucine (deH-DHLNL), dehydro-hydroxylysinonorleucine (deH-HLNL), dehydro-histidinohydroxymerodesmosine (deH-HHMD), pyridinoline (Pyr), deoxypyridinoline (d-Pyr), histidinohydroxylysinonorleucine (HHL) and pyrrole [77–80]. The first three of these cross-links are reducible, immature, whereas the other four are nonreducible and mature [77,81,82]. Additionally, also pentosidine (PEN), the only characterized non-enzymatic cross-link identified so far [78], can be found in bone [77].

2.3 MINERALIZATION

Soluble calcium and phosphate in the organic matrix of bone forms solid calcium phosphate through a phase transformation; a process exemplified by the formation of ice from water, *i.e.* mineralization of bone [1,83]. Initially, solid calcium phosphate is poorly crystalline apatite [83]. With time, the crystallinity of the apatite increases [1], but it never approaches the highly crystalline state found in naturally occurring geological hydroxyapatite [1,83]. The mineral appears between the collagen fibers in specific hole zone regions. Those are separated by the unmineralized regions of collagen fibrils. Then the mineralization of the matrix continues progressively in the increasing number of hole zone regions. Ultimately, mineral deposits occupy all of the available space within the collagen fibrils [1]. Once the mineralization begins it is a relatively fast process and most of the final mineral forms within hours [1]. Thereafter, mineral continues to accumulate over a prolonged period of time increasing the density of bone. An alternative process has been postulated *i.e.* the initial mineral deposited is in amorphous form [84,85].

2.3.1 Crystallinity

Bone mineral is structurally related to the naturally occurring geologic mineral, hydroxyapatite ($Ca_{10}[PO_4][OH_2]_2$) that undergoes changes in its crystal size and perfection, as well as in the amount of impurities, *e.g.* carbonate and magnesium [1,86]. Generally, the crystal length and perfection increases and crystal thickness decreases with age [86, 87]. In human bone, beyond the age of 25 years only minor changes have been found, but after the age of 50 years, the average length decreases slightly [87]. Crystallinity also increases with tissue age [24,38,39]. Since bone mineral crystals are found between the collagen fibrils, the fibril structure limits the size and orientation of the crystals [86]. The mineral accumulation starts from the nucleation of HA crystals at multiple sites on the collagen fibrils [1]. Nucleation normally originates in locations matching the structure of the crystal being formed [1]. In bone, the extracellular proteins act as nucleators because of their affinity for HA and they also control the growth of the crystals. The size of the crystals are further increased by secondary nucleation, where ions are added to the smallest crystals and each crystal can serve as a branching point for nucleation of new crystals [86].

2.3.2 Carbonate substitution

Apatite has several crystallographic sites where atomic exchanges can occur [88]. In a mineral crystal, *e.g.* hydroxyapatite, the composition is not fixed, but the chemical variations that may occur have to fulfill the overall charge balance and must fit geologically.

Carbonate (CO_3^{2-}) ion fulfills these criteria and can substitute into the hydroxide (OH^-) or phosphate (PO_4^{-3}) site of the HA crystal. These substitutions are called type-A and type- B substitutions, respectively [24,88,89]. Neither of these substitutions fulfill the criteria for an overall charge balance on their own. Thus, their presence explains why biological apatite is calcium deficient. The rates of these substitutions alter with increasing age and changes in the remodeling rate, *e.g.* the type-B substitution, *i.e.* carbonate replaces phosphate, is known to decrease as the crystallinity, *i.e.* the size of the HA crystals, increases [24,88,90,91]. Carbonate substitution has also been shown to decrease with a high remodeling rate [92].

2.4 BONE FUNCTION

The skeleton has many important functions in the body. It protects the internal organs and maintains the mineral ion homeostasis [6,7]. Bones engage in body movements when muscle contraction moves them via the forces exerted on tendons and ligaments [6,7]. The skeleton also provides the body with its integrity, and is posesses remarkable mechanical properties.

In general, it is cortical bone that confers the compressive strength on the bone and it also provides maximum resistance to torsion and bending in the diaphysis of the long bones [1]. The spongy like trabecular bone has approximately a twenty times higher surface area per volume compared to cortical bone [1]. The trabecular bone will permit some deformation under mechanical loading.

The organic matrix gives bone its form and its ability to resist tension whereas the minerals in the inorganic matrix resist compression [1,93]. Together they determine the mechanical properties of bone and alterations in one component will affect the mechanical properties of bone significantly. Thus, the balance between the organic and the inorganic matrices is crucial. In simple terms, the minerals make the bone stiff but brittle and collagen makes the bone flexible but soft. It has been shown that the integrity of the collagen network has a direct impact on the toughness and strength but not on the stiffness of bone [94]. Presumably, also collagen cross-links affect the mechanical properties of bone [77,93]. It has been proposed that the collagen cross-links have an effect on the bending strength and bone toughness but the maturity of the cross-links may not be very important to the mechanical properties of bone [93]. With age, the mechanical integrity of the collagen network deteriorates [95] whereas minerals continue to accumulate [1]. These changes might increase the fracture risk as the bones become more brittle.

2.5 BONE FORMATION

Bone formation, also known as ossification or osteogenesis, is driven by the osteoblast cells that produce bone [2]. Bone formation may occur within cartilage, *i.e.* endochondral formation, within the organic matrix membrane, *i.e.* intramembranous formation, or by deposition of new bone on existing bone, *i.e.* appositional formation [2]. All three types of bone formation follow the same mechanism and can occur throughout life. First, mesenchymal stem cells become osteoblasts and begin to secrete extracellular matrix that starts to mineralize. Osteoblasts surrounded by the mineralized matrix become osteocytes. Thereafter osteoclasts appear and the remodeling process begins. The remodeling process converts immature woven bone into mature lamellar bone and furthermore resorbs and replaces mature lamellar bone [2].

The size and form of the bones are mainly determined by the genome, but also mechanical loading of the bones is known to modify the growth and adaptation of the bone tissue [2]. A failure to form bones with appropriate shape and size leads to skeletal deformity [2]. In bone formation, first woven bone is formed; it has a random organization and is less mineralized compared to lamellar bone. Whitin a relatively short time [5], the bone matrix becomes more organized and mineralized as woven bone is replaced by lamellar bone [1].

2.6 MODELING AND REMODELING

After the embryonic skeleton has been formed, osteoblasts and osteoclasts initiate the modeling and remodeling of each bone [2,7, 12]. In general, during modeling the shape of the bone is altered, whereas remodeling refers to turnover of bone that does not alter the shape. Often these two processes occur simultaneously and their distinction may be difficult. During the growth of the skeleton, the turnover rate is close to 100 % per year in the first year of life but later it declines to approximately 10 % per year in late childhood and usually continues at this rate or lower throughout life [2,7].

Modeling occurs usually during growth, when coordinated resorption and formation of bone modify the shape of the bone [2,7]. When bones grow, especially long bones, the growth of the physes lengthen the bone and the metaphyses must be reshaped to give the typical structure of a long bone [2]. In adults, the bones are fully grown, but remodeling of bones continues also after the skeletal growth has ended. Remodeling can be divided into physiological remodeling and age-related remodeling. Physiological remodeling, *i.e.* removal and replacement of bone at roughly the same location, takes place throughout life without affecting the shape of the bone [2]. Physiological remodeling occurs on the surface of the bone as well as within the bone. Age-related remodeling, or bone loss, is evident mainly in the elderly. With age, the bone mass declines as trabecular number and cortical bone thickness decrease and cortical bone porosity increases [2]. Additionally, adaptive modeling and remodeling affect the bone shape, density and size. Bone tissue is highly adaptive [4] and according to Wolff's law the bone adapts to its mechanical loading environment [3]. Thus, mechanical stimulus of the bones has generally a positive influence on the structure and mechanical properties of bone [2,58,96].

Osteoblasts and osteoclasts work together to reshape the bones to adapt to the loading environment. Osteoclasts resorb bone and osteoblasts form new bone at the site of resorption. During bone modeling, the actions of the osteoblasts and osteoclasts are not linked (Figure 2.3A) and thus rapid changes in the amount and shape of the bones can occur [7]. During bone remodeling, the osteoblasts work together with osteoclasts (Figure 2.3B) and if the remodeling is balanced, the net changes in the amount and shape of bone remain low [7].

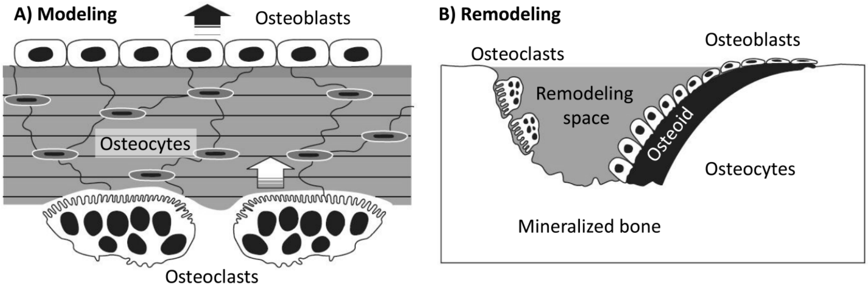

Figure 2.3: Schematic presentation of function of osteoblasts and osteoclasts during modeling A) and remodeling B). (Modified from [7].)

2.7 FRACTURE HEALING

Fracture healing mechanisms are similar to the developmental mechanism (see section 2.5) [11, 12]. Endochondral, intramembranous or appositional formation occur to varying degrees under different circumstances. Callus formation is a critical step for successful fracture healing [12]. When a fracture occurs, the local soft tissue integrity is typically disrupted, normal vascular function is interrupted and marrow architecture is disturbed [12]. This damage activates the non-specific wound healing pathways. Bleeding within the fracture site develops first into a hematoma which further clots into a fibrinous thrombus. Subsequently, the thrombus is reorganized into granulation tissue. A range of cytokines and growth factors coordinate the cellular responses and control the migration of mesenchymal stem cells that will differentiate into various cell types, depending on the mechanical environment. These can be fibroblasts, chondrocytes, or bone forming cells.

The cells form a semi-rigid avascular cartilaginous callus, *i.e. soft callus*, which confers mechanical support for the fracture [12]. Subsequently, the cartilaginous callus is replaced with woven bone as the vascular invasion takes place. The soft callus is somewhat random in its orientation.

After the soft callus formation, the osteoblast activity and the formation of mineralized bone matrix increase remarkably [12]. The soft callus is gradually removed as new mineralized bony callus, *i.e. hard callus*, bridges the fracture. Also the hard callus is irregular and under-remodeled. Hence in the last stage of fracture repair, the woven bone in the hard callus is remodeled into lamellar bone, which is finally resorbed to restore the original cortical or trabecular bone configuration [12]. By this last phase, the mechanical properties of the bone will approach those that it possessed prior to the fracture [12, 97].

BONE MORPHOGENETIC PROTEINS AND BISPHOSPHONATES

Bone morphogenetic proteins (BMPs) increase the callus size and the amount of new bone formation by stimulating the formation of osteoblasts that produce new bone matrix [13, 15]. They also provoke osteoclast formation (by stimulating the production of RANKL by osteoblasts) and thus increase bone resorption [13–15]. Thus, BMPs increase the speed of remodeling of the callus and bone tissue. Bisphosphonates (BPs) reduce the resorption of bone and callus tissue by inhibiting osteoclast activity [16]. BPs bind to bone mineral and after osteoclasts resorb the bone, they undergo apoptosis [13, 16]. Both BMPs and BPs are approved for clinical use and they have been shown to be valuable in the treatment of fractures in experimental models [13–15, 98, 99].

3 Bone diagnostics

Bone has been studied extensively from many different points of view *e.g.*, the shape, macro- and micro-architecture and structure, composition and mineral structure and their alterations with maturation and in different diseases. The shape, architecture and structure of bone can be evaluated by X-ray imaging methods, *e.g.* X-ray computed tomography (CT) and micro-computed tomography (µCT). Bone composition has traditionally been studied via biochemical analysis (BA) methods. However, different spectroscopic methods, *e.g.* Fourier transform infrared (FTIR) and Raman microspectroscopy, have also been increasingly used to study the molecular composition of bone. The mineral structure, *i.e.* the size and shape of HA crystals, has been investigated with small angle X-ray scattering (SAXS) or X-ray diffraction (XRD) techniques. The organization and orientation of collagen fibers can be studied with polarized light microscopy (PLM). The characteristics determined by these methods (Table 3.1) and their joint effect on the mechanical properties of bone, all contribute to *bone quality* [100–102].

Table 3.1: Bone analysis techniques, what they measure and extrapolated interpretation.

Technique	Measure	Extrapolation
BA	Content	-
FTIR	Chemistry and content	Mineral and collagen characteristics
Raman	Chemistry and content	Mineral and collagen characteristics
PLM	Light polarization in a sample	Collagen characteristics
µCT	Sequential X-ray absorption images	Indices of 3-dimensional microarchitecture
SAXS	X-ray scattering pattern	Mineral characteristics

3.1 BONE COMPOSITION

Traditionally, BA has been used to study the organic composition of bone. High-pressure liquid-chromatography (HPLC) has been used to evaluate the amount of collagen and different cross-links [77,103,104]. However, in BA the composition of the inorganic matrix is not studied. In contrast, FTIR and Raman spectroscopy provide compositional information of both the organic and the inorganic matrices of bone simultaneously.

3.1.1 Infrared spectroscopy

INFRARED RADIATION

Infrared spectroscopy is based on absorption of infrared (IR) radiation into the chemical bonds of molecules. The wavelength λ of IR radiation ranges from 700 nm to 1 mm. In IR spectroscopy, usually one refers to *wavenumber* $\bar{\nu}$ [cm^{-1}] instead of wavelength [105,106]. It is defined as follows:

$$\bar{\nu} = \frac{1}{\lambda} = \frac{\nu}{c} \quad , \tag{3.1}$$

where ν is the frequency of the radiation and c is the speed of light in a vacuum. The molecular bonds in bone tissue absorb IR radiation in a wavenumber range of 2000 - 800 cm^{-1} which corresponds to a wavelength range of 5000 - 12500 nm (Equation 3.1). The energy of the IR radiation can be calculated as:

$$E = h\nu = \frac{hc}{\lambda} = hc\bar{\nu} \quad , \tag{3.2}$$

where h is Planck's constant [105,106].

INFRARED ABSORPTION

Infrared radiation has enough energy to change the vibrational and rotational levels of a molecule. The total energy E_t of the molecule is

$$E_t = E_e + E_v + E_r \quad , \tag{3.3}$$

where E_e is the electronic, E_v is the vibrational and E_r is the rotational energy of the molecule [105]. The IR spectrum is generally composed of higher energy vibrational level changes whereas the rotational levels with smaller energeis are seen in the fine structure of the spectrum [107].

Molecular vibrations can be divided into stretching and bending vibrations. Stretching vibrations can be further divided into symmetric and asymmetric states. In stretching, the length of the molecular bond changes whereas in bending the angle of the bond changes (Figure 3.1) [105].

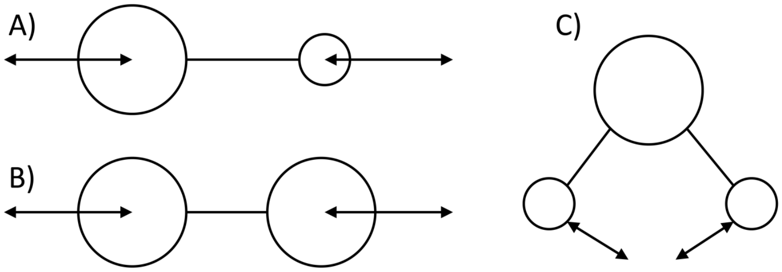

*Figure 3.1: Schematic presentation of a stretching heteronuclear diatomic molecule with a non-zero dipole moment A), stretching homonuclear diatomic molecule with a zero dipole moment B) and three atomic bending molecule (*e.g. *H_2O) with a non-zero dipole moment C).*

For a molecule to absorb IR radiation, two conditions must be fulfilled: 1) the energy of an IR radiation quantum has to be equal to the difference between the excited and the ground state of the molecule and 2) the electric dipole moment of the molecule has to change during vibration of the molecule. The molecule is *IR-active* when the electric dipole moment of the molecule is non-zero [105]. The electric dipole moment $\bar{p}$ is defined as:

$$\bar{p} = \sum_{i=1}^{N} Q_i \bar{r}_i \quad , \tag{3.4}$$

where $\bar{r}$ is the distance of the electric charge Q of i^{th} atom from the chosen reference point. N is the total number of atoms in the system. When both of these conditions are matched, the molecule will absorb IR radiation energy. For example, in a heteronuclear diatomic ($N = 2$) molecule, the dipole moment changes as the bond length changes (Figure 3.1A), thus the molecule is IR-active. In contrast, in a homonuclear diatomic molecule, the dipole moment remains always zero and is thus *IR-inactive* (Figure 3.1B) [105].

In the traditional transmission mode, IR radiation with a wide wavelength range passes into the sample and the energy loss at different wavelengths is recorded. The IR radiation intensity that passes through the sample can be described by transmittance $T(\bar{v})$. Transmittance is the ratio of the transmitted intensity of the radiation $I(\bar{v})$ to the incident intensity $I_0(\bar{v})$:

$$T(\bar{v}) = \frac{I(\bar{v})}{I_0(\bar{v})} = e^{-\sigma(\bar{v})cl} \quad , \tag{3.5}$$

where σ is the molecular absorption coefficient which describes the absorption properties of the molecule, c is the concentration of the absorbing molecule and l is the optical path length (the thickness of the material). In IR spectroscopy, absorbance is generally used instead of transmittance. The absorbance $A(\bar{v})$ is related to transmittance by the logarithmic operation:

$$A(\bar{v}) = -\ln(\frac{I(\bar{v})}{I_0(\bar{v})}) = \ln(\frac{1}{T(\bar{v})}) = \ln(e^{\sigma(\bar{v})cl}) \quad . \tag{3.6}$$

This results in the formula known as *Beer-Lambert's law*:

$$A(\bar{v}) = \sigma(\bar{v})cl \quad . \tag{3.7}$$

According to Beer-Lambert's law, the relation between the absorbance and the concentration of the absorbing material is linear, but this is valid only under ideal conditions [105]. In most situations, the tissues are heterogeneous and Beer-Lambert law is not directly applicable.

Quantum physics states that ideally the absorption peaks in a spectrum would be infinitely narrow. However, in reality, the peaks are spread because of collisions between molecules and the finite lifetime of the excited state of the molecule, for example. *Heisenberg* *uncertainty principle* states that the shorter the lifetime of the state, the less well defined will be the energy:

$$\Delta E \Delta t = \frac{\hbar}{2} \quad , \tag{3.8}$$

where ΔE is the uncertainty of the energy, Δt the uncertainty of time and $\hbar = \frac{h}{2\pi}$ [105, 107].

INSTRUMENTATION

The main components of a modern FTIR spectrometer are the radiation source, the beamsplitter, static and moving mirrors and the detector (Figure 3.2). IR radiation is generated when the radiation source is heated. The beamsplitter, a semi-reflecting film, at a 45° angle will reflect 50 % of the radiation into a static mirror with the other 50 % being passed to a moving mirror. The reflected radiation from both mirrors experiences interference back at the beamsplitter. The united beam is passed through the sample and the signal collected by the detector is called an *interferogram* (Figure 3.3A). When the Fourier transform of this interferogram is calculated, an IR absorption spectrum is obtained (Figure 3.3B).

FTIR microspectroscopy is currently the preferred method for IR spectroscopy since it combines the IR spectrometer with a microscope,and this makes it possible to map the sample with a spatial resolution of a few micrometers. When visible light is used with the IR microscope, the spatial measurement areas of the samples can be pre-defined visually.

FTIR MICROSPECTROSCOPY ON BONE

FTIR spectroscopy is a well-accepted and widely used method chosen by many investigators for characterizing the molecular composition of biological tissues [108]. This is true also for bone. FTIR spectroscopy makes it possible to evaluate changes in the molecular composition of bone in relation to animal age [20, 21, 39, 109–111], tissue age [24, 37–39], at the site of micro-cracks [112] and dur-

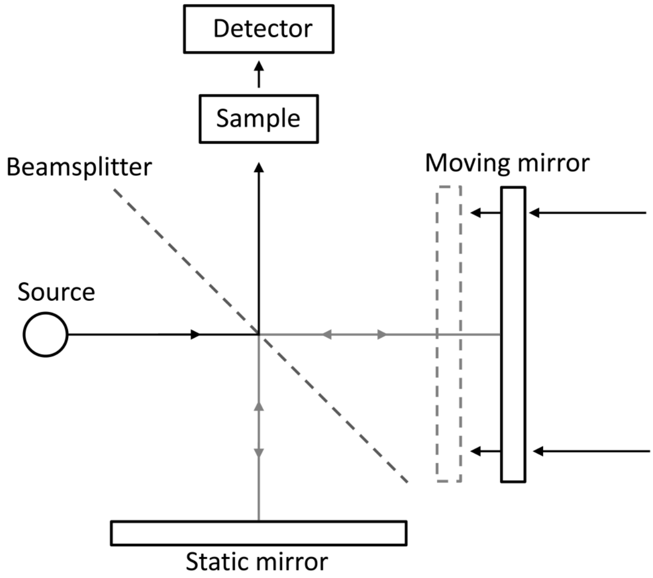

Figure 3.2: Schematic presentation of a FTIR spectrometer. IR radiation is generated in the source and then passed to the beamsplitter. 50 % of the radiation is reflected from the static mirror and 50 % from the moving mirror and combined again at the beamsplitter. After the interference the united radiation is passed through the sample to the detector.

ing fracture healing [113, 114]. In addition, the effect of different diseases [23, 81, 90, 92, 115–119] and treatments [28, 120–122] on the composition of bone have been investigated. Compositional effects on the bone mechanical properties have also been examined [22, 31, 123, 124]. It is clear that the molecular composition of bone is affected by many factors and some of those changes can be detected using FTIR microspectroscopy.

The most important FTIR parameters describing the composition of bone are presented in Table 3.2. Usually the composition is evaluated from the areas of the peaks in the spectra. The amide I peak area represents the collagen content, the phosphate peak area refers to the phosphate content and the carbonate peak area to the carbonate content (Figure 5.2). Peak-fitting techniques are also widely used and the areas of the sub-peaks are then calculated to describe the content, *e.g.* type-A carbonate and type-B carbonate or

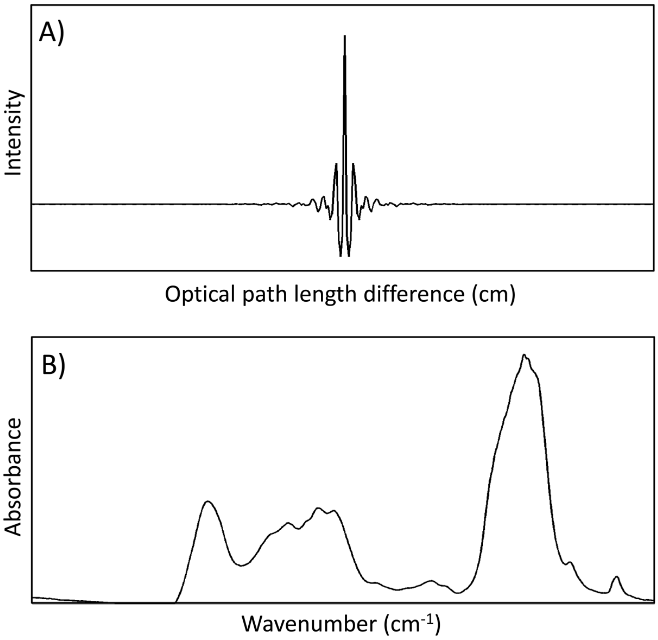

Figure 3.3: An interferogram A) and the corresponding IR spectrum of human trabecular bone B).

cross-link contents. However, since thin sections (1-5 μm) are used in transmission FTIR microspectroscopy and the absorption is directly proportional to the thickness of the sample, usually ratios of the peak areas or intensities are reported (Table 3.2).

The mineral/matrix ratio represents the degree of mineralization of the bone [17]. The carbonate/matrix ratio reveals information about the carbonate content in bone [18, 19]. Since carbonate content can change either as a function of mineral content or mineral maturity (crystallinity), the carbonate/matrix ratio should always be considered together with the carbonate/phosphate ratio if one wishes to gain a meaningful perspective. The carbonate/phosphate ratio describes the carbonate substitution into the HA [17], and similarly the type-A and type-B carbonate/phosphate ratios describe the type-A and type-B carbonate substitution into the HA. The type-B carbonate/phosphate ratio as calculated from

Table 3.2: Most important FTIR parameters of bone composition, the determination method (D "direct" and PF "peak fitting") and the wavenumbers. Given wavenumber range describes the area of the peak that was used to calculate the parameter. Wavenumber with a symbol ($\sim$) means that the area of the fitted sub-peak at that wavenumber was used to calculate the parameter. Exact wavenumber means that the intensity of the spectrum at that wavenumber was used. The Roman numerals indicate the parameters used for the first time in the publications in this Thesis.

Parameter	**Method**	**Wavenumbers [cm^{-1}]**
Amide I	D [17]	1720-1585
Phosphate	D [17]	1200-900
Total carbonate	D [17]	890-850
Type-A carbonate	PF [24]	$\sim$878
Type-B carbonate	PF [24]	$\sim$871
Labile carbonate	PF [24]	$\sim$866
Mineral/matrix	D [17]	(1200-900):(1720-1585)
Carbonate/matrix	D [18,19]	(890-850):(1720-1585)
Carbonate/phosphate	D [17]	(890-850):(1200-900)
Type-B carbonate/matrix	PF **I**	($\sim$871):(1720-1585)
Type-B carbonate/phosphate	PF **I**	($\sim$871):(1200-900)
Type-B carbonate/phosphate	PF **I**	($\sim$1044):(1200-900)
Type-A carbonate fraction	PF [24]	($\sim$878):(890-850)
Type-B carbonate fraction	PF [24]	($\sim$871):(890-850)
Labile carbonate fraction	PF [24]	($\sim$866):(890-850)
Collagen cross-linking ratio	D [22]	1660:1690
	PF [17,21]	($\sim$1660):($\sim$1690)
Crystallinity	D [27,28]	1030:1020
	PF [17,23]	($\sim$1030):($\sim$1020)
Acid phosphate substitution	D [26]	1127:1096
	PF [17]	($\sim$1106):($\sim$1030)
	PF [17]	($\sim$1106):($\sim$960)

the sub-peak at $\sim$1044 cm^{-1} to the phosphate peak area is believed to reflect the type-B carbonate fraction in the HA crystals [20,24]. Collagen cross-linking ratio, or *collagen maturity*, refers to the ratio of mature/immature cross-links in bone [17,21,22]. Crystallinity is related to the size and perfection of the HA crystals [17,23] and has been shown to correlate with HA crystal c-axis length determined with XRD [23–25]. The acid phosphate substitution ratio describes the acid phosphate (HPO_4) substitution into HA in mineralized tissues [17, 26]. Collagen maturity, crystallinity and acid phosphate substitution can be evaluated through peak-fitting [17, 21, 23], *i.e.* the ratio between the areas or intensities of the sub-peaks, or directly as the ratio of the intensities of the wavenumbers in the spectrum [22, 26–28]. Both methods yield similar results.

The mineral/matrix ratio, carbonate/matrix ratio, carbonate-/phosphate ratio, crystallinity and collagen maturity increase with tissue age [17,21,24,37,38]. Acid phosphate substitution decreases with tissue age [17], since higher acid phosphate substitution indicates new bone formation [110, 125, 126]. The same behavior in these parameters can be seen with animal age, but no clear changes in crystallinity have been shown [39].

In addition, FTIR has been used to investigate the variation in composition between different anatomical locations, however, the number of studies is rather limited. Donnelly *et al.* studied the composition of subtrochanteric femur, the iliac crest and greater trochanter [10]. They reported a greater mineral/matrix ratio in cortical bone in the subtrochanteric femur than in other locations. However, no other differences were observed in the cortical and trabecular bone between those locations.

The molecular composition of the fracture callus during fracture healing has also received very little attention. Yang *et al.* used FTIR to study the composition of the fracture callus and bone cortex during fracture healing in wild type and interleukin-6 knockout mice [114]. The cortex had a higher mineral/matrix ratio compared to callus, whereas they detected no differences in crystallinity between callus and cortex. Other FTIR compositional parameters were not reported in that study. Ouyang *et al.* evaluated the effects of estrogen and estrogen deficiency in fracture callus in rat femurs [113]. They found a lower mineral/matrix ratio, higher carbonate/phosphate ratio, lower collagen maturity and slightly reduced crystallinity in the fracture callus when this was compared to the fracture cortex.

3.1.2 Raman spectroscopy

RAMAN SCATTERING

Raman spectroscopy is based on light scattering from the molecules in the sample. A monochromatic light (laser), usually IR or ultraviolet (UV), is focused onto the sample and the Raman scattered photons are collected. The laser interacts with the molecules and most of the scattered photons undergo elastic *Rayleigh scattering*, where the scattered photons have the same wavelength as the incident photons (Figure 3.4). However, some of the photons interact with the molecules in such a way that the energy of the scattered photons becomes either shifted up, *i.e. Anti-Stokes Raman scattering*, or down, *i.e. Stokes Raman scattering* (Figure 3.4). The intensity of Rayleigh scattering is generally 10^{-3} of the intensity of the incident radiation, whereas only one in ten million photons is Raman scattered [106]. Based on equation (3.2), the energy in Anti-Stokes Raman scattering and Stokes Raman scattering can be expressed as

$$E = hc\bar{\nu} = hc(\bar{\nu}_0 \pm \bar{\nu}_M) \quad , \tag{3.9}$$

where $\bar{\nu}_0$ is the wavenumber of the incident photon and $\bar{\nu}_M$ the wavenumber of the scattered photon. For Anti-Stokes Raman scattering, the change in the wavenumber is positive $\bar{\nu}_0 + \bar{\nu}_M$, and for Stokes Raman scattering the change in the wavenumber is negative $\bar{\nu}_0 - \bar{\nu}_M$. When a molecule system interacts with radiation, it can make an upward transition from a lower energy level E_1 to a higher E_2 (Figure 3.4). The incident radiation must have the necessary energy

$$\Delta E = E_2 - E_1 = hc\bar{\nu}_M \tag{3.10}$$

to evoke this transition [106]. Thus, the wavenumber of the scattered photon is directly proportional to the difference in the energies between the two states. This shift in the energy, *i.e. Raman shift*, provides information about the vibrational and rotational modes in the molecular system. In Raman microspectroscopy, usually the Rayleigh scattered photons are filtered from the signal and only the (Stokes) Raman shifted radiation is analyzed.

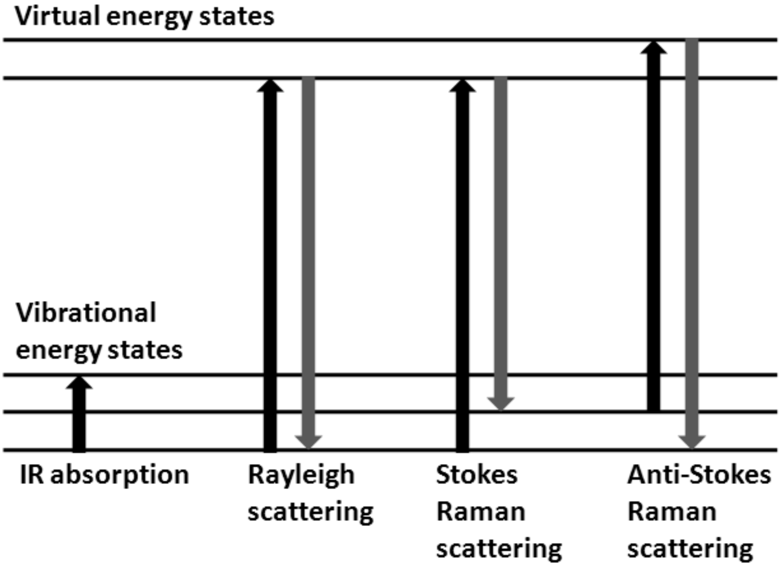

Figure 3.4: A schematic presentation of energy level transitions in IR absorption, Rayleigh and Raman scattering.

Raman-activity does not depend on the electric dipole moment in the same way as the IR-activity. The *polarizability* of a Raman-active molecule has to be non-zero. The polarizability is defined as

$$\vec{P} = \alpha \vec{E} \quad , \tag{3.11}$$

where $\vec{P}$ is the induced dipole moment by the electric field $\vec{E} = E_0 \cos(2\pi \bar{\nu}_0 t)$ when α is the electronic polarizability of the molecule. When $\bar{\nu}_M = 0$, the polarizability $\alpha = 1$ and no Raman scattering occurs, and the total induced dipole moment depends only on the electric field $\vec{E}$ leading to Rayleigh scattering. Thus, when $\bar{\nu}_M \neq 0$, the dipoles in the molecule oscillate which results in Anti-Stokes or Stokes Raman scattering [106].

The electric dipole moment of a homonuclear diatomic molecule is zero, *i.e.* the molecule is IR-inactive, but it has a non-zero polarizability, *i.e.* the molecule is Raman-active. A heteronuclear diatomic molecule has a non-zero electric dipole moment and is thus IR-active. It also has a non-zero polarizability and is also Raman-active [106]. As mentioned earlier, a molecule with a zero electric dipole moment is also non-polar. Since electric dipole moment does not affect Raman-activity, Raman spectroscopy detects both polar and non-polar molecular bonds. Generally, biochemical molecules have a relatively low symmetry. In these molecules, nearly all of the vibrations are both IR- and Raman-active. Only some molecules with very high symmetry contain vibrations that are both IR- and Raman-inactive [106].

INSTRUMENTATION

In a dispersive Raman microscope, the laser is first excited from a laser source. In some instruments, the wavelength and power of the laser can be chosen by the operator to obtain the best laser excitation. Usually the Raman microscope is coupled with a motorized stage to allow microscope guided movement of the sample. The laser beam is focused onto the sample through a microscope. The same microscope objective is used for the incident light as well as to collect the scattered photons. Usually a notch-filter is used to filter the Rayleigh scattered photons and the acquired data consists of only the Raman scattered photons. The Raman scattered photons are usually collected with a multichannel two-dimensional charge-coupled device (CCD), which provides high quantum efficiency, a low level of thermal noise and a high spectral range. Usually the CCD chip is cooled, *e.g.* with a Peltier thermoelectrical air cooled device, to under -50 °C. From the CCD matrix, the data is processed electronically as the Raman scattered photons where different wavelengths are counted and a Raman-spectrum is formed [127,128].

RAMAN MICROSPECTROSCOPY ON BONE

Raman microspectroscopy has been used to study the compositional changes in bone, *e.g.* during aging [29–36] and in different diseases [91,129,130]. It has also been used to study the bone composition through rat skin using time-resolved transcutaneous Raman spectroscopy [131] and to investigate the relationship between composition and mechanical properties of bone [31,132,133].

Similar compositional information of bone is obtained with Raman and FTIR microspectroscopy. Most of the parameters are the same and provide similar information, but the information of the two techniques are complementary. Since FTIR and Raman spectroscopy are based on different physical phenomena, the spectra are different and thus also the analyses differ. For example, the peak locations and some parameter definitions may vary. Additionally, the used peaks in the compositional analysis vary more than in FTIR spectroscopic analysis of bone. For example, as collagen content is usually determined from amide I peak area in FTIR analysis, in Raman analysis amide I, amide III or CH_2 wag peaks are typically used [134]. These and several other Raman peaks arise from the organic matrix [135,136]. In Raman spectroscopy, the peak intensities or the areas of the peaks are used to assess the molecular composition. Section thickness is not an issue in Raman spectroscopy, since the Raman scattering is usually recorded from the surface of the sample. The intensities of the peaks depend mainly on defined laser intensity and exposure time. Nonetheless, usually ratios of peak intensities or areas are used. Thus, bone compositional parameters derived from FTIR and Raman spectra are mostly comparable. The most important Raman parameters of composition of bone are presented in Table 3.3.

Similar changes in bone composition with age have been found with FTIR and Raman microspectroscopy, *e.g.* an increase in mineralization and type-B carbonate substitution and content [30–36]. Crystallinity has been found to remain relatively constant with animal age [30,35,36].

When a Raman spectroscope is coupled with a polarizer, it can be used to also determine the orientation of the mineral crystals and collagen fibers [33,140]. With a polarized Raman spectroscope, the orientation can be determined by changing the polarization direction. The polarization is greatly dependent on the numerical aper-

Table 3.3: Most important Raman parameters of bone composition, the determination method (D "direct" and PF "peak fitting") and the wavenumbers. Given wavenumber indicates the approximate location of the peak. Wavenumber with a symbol (∼) means that area of the fitted sub-peak at that wavenumber was used to calculate the parameter. Exact wavenumber means that the intensity of the spectrum at that wavenumber was used. The Roman numerals indicate the parameters used first time in the publications in this Thesis. Crystallinity is calculated as the inverse of the full width of half maximum (FWHM) of the phosphate peak.

Parameter	**Method**	**Wavenumbers [cm^{-1}]**
Amide I	D [135]	1720-1585
Amide III	D [137]	1345-1180
CH$_2$	D [35]	1490-1400
Phosphate	D [138]	990-903
Type-B carbonate	D [138]	1110-1046
	PF [139]	∼1070
Mineral/matrix	D [30]	(990-903):(1720-1585)
	D [137]	(1345-1180):(1720-1585)
	D [35]	(1490-1400):(1720-1585)
Type-B carbonate/matrix	D [30]	(1110-1046):(1720-1585)
Type-B carbonate/matrix	PF **I**	(∼1070):(1720-1585)
Type-B carbonate/phosphate	D [30]	(1110-104):(990-903)
Type-B carbonate/phosphate	PF [139]	(∼1070):(990-903)
Collagen cross-linking ratio	D [129]	1660:1690
	PF [137]	(∼1660):(∼1690)
Crystallinity	D [32]	1/(990-903 FWHM)

ture (NA) in use, yielding a higher polarization effect with high-NA objectives [140]. The parallel evolution of the tissue orientation and composition as a function of animal age, as well as tissue age has been observed [33].

3.2 BONE STRUCTURE

3.2.1 Polarized light microscopy

Polarized light microscopy (PLM) can be used to study the organization of collagen fibers in biological tissues, *e.g.* to determine the collagen network birefringence, *i.e.* a property of a material that causes the phase-shift of light [107], collagen fiber parallelism and orientation [43].

LIGHT POLARIZATION

Light from ordinary light sources is unpolarized. Unpolarized light is a mixture of linearly polarized waves in all possible transverse directions. If one starts with unpolarized light, then polarized light can be created by using a filter, *i.e. polarizer*, that passes through only one transverse wave of the light [107]. An ideal polarizing filter would pass 100 % of the incident light in the polarization direction, *i.e. polarizing axis*, and 0 % perpendicular to it. However, that kind of device cannot be built. A Polaroid filter, for example, transmits 80 % of the light in the polarizing axis but only 1 % or less of the waves polarized perpendicular to it. The intensity of polarized light after an ideal polarizer is exactly half of the unpolarized light [107].

If a second polarizer, or *analyzer*, is added after the first polarizer, then the linearly polarized light experiences another polarization. If ϕ is the angle between the polarizing axes of the polarizer and analyzer, then according to Malus's law

$$I = I_0 \cos^2\phi \quad , \tag{3.12}$$

where I is the intensity of the passed light and I_0 the incident linearly polarized light, with $\phi = 0^\circ : I = I_0$ and with $\phi = 90^\circ : I = 0$ [107].

Light can also have a circular polarization. It is a superposition of two linearly polarized waves with a quarter-cycle phase difference. When illustrated, this circular polarization light would appear as a rotating helix. A crystal called *quarter-wave plate*, or $\lambda/4$-phase shift plate, is just thick enough to introduce a quarter-cycle phase difference. This kind of crystal converts the linearly polarized light into circularly polarized light and *vice versa* [107].

INSTRUMENTATION

A typical PLM instrumentation is shown in Figure 3.5. In PLM, the light is generated by a light source, *e.g.* halogen lamp, which has a temperature that is regulated to keep it constant [43]. Monochromators (Figure 3.5B, mc) adjust the wavelength of the light so that it is in a narrow range. A depolarizer (Figure 3.5B, dp) ensures the unpolarized state of the entering light. The polarizers (Figure 3.5B, p) and $\lambda/4$-phase shift plates (Figure 3.5B, $\lambda/4$) are then used to allow the polarization at a certain wavelength. The images are captured with a camera attached to the microscope [43].

The data is collected by stepwise rotations of the polarizer pair. The images are taken with and without the sample in order to record the background images which are needed to undertake the background correction. In addition, images with the same polarizer pair orientations with $\lambda/4$-phase shift plate on the path are taken. These images are used to calculate the *Stokes parameters* from which one can calculate the orientation of *e.g.* collagen fibers. From the images, also birefringence and parallelism index can be calculated [43].

The Stokes parameters are calculated from the grayscale data at each pixel as follows [141]:

$$\begin{aligned} S_0 &= I_{(0^\circ)} + I_{(90^\circ)} \quad , \\ S_1 &= I_{(0^\circ)} - I_{(90^\circ)} \quad , \\ S_2 &= 2 \cdot I_{(45^\circ)} - S_0 \quad , \\ S_3 &= S_0 - I_{(90^\circ + \lambda/4)} \quad , \end{aligned} \tag{3.13}$$

where I is the light intensity, S_0 is the total intensity of light, S_1 is the amount of linear/horizontal polarization, S_2 is the amount

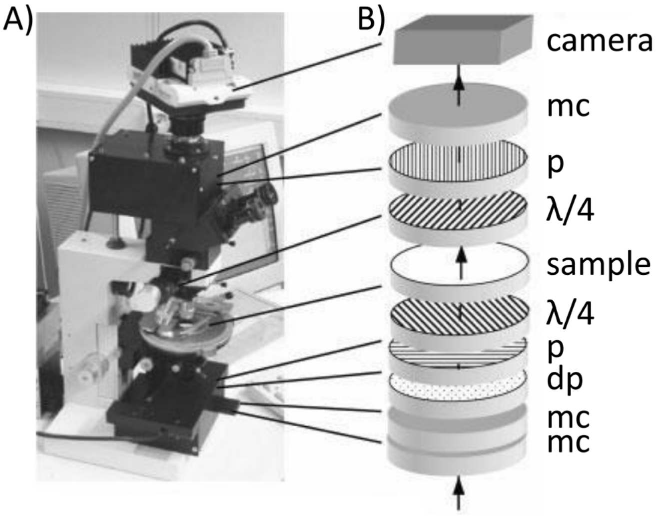

Figure 3.5: Leitz Ortholux BK II POL microscope A) in University of Eastern Finland, Department of Biomedicine, Kuopio, equipped with computer-controlled rotatable optical components and layout of the optical components B). Layout shows three monochromators (mc), a depolarizer (dp), two polarizers (p), two $\lambda/4$-phase shift plates and the location of the sample and the CCD-camera. (Modified from [43].)

of +45° or -45° polarization and S_3 is the amount of right or left circular polarization. The intensity subscripts indicate the background corrected 0°, 45°, 90° and the 90° images taken with the $\lambda/4$-phase shift plate. From the Stokes parameters (Equation 3.13), the orientation angle Ψ of the polarization ellipse can be calculated as follows [141]:

$$\Psi = \frac{\arctan(\frac{S_2}{S_1})}{2} \quad , \quad 0^\circ \leq \Psi \leq 90^\circ \quad . \tag{3.14}$$

The orientation angle of the polarization ellipse is directly related to collagen fiber orientation which is calculated in each pixel [43]. The pixel area is large when compared to the collagen fiber dimension. Therefore, each pixel is an average of the pixel area times the thickness of the sample and the orientation in each pixel represents the average orientation in that pixel area.

As the polarizer pair rotates, the observed signal intensity follows a sinusoidal function [43]

$$I = A + \sin^2(2\alpha + \omega) \quad , \tag{3.15}$$

where I is the signal intensity, A a specific constant for the microscope, α the rotation angle and ω the phase shift. This equation can be used to find the actual and theoretical signal minimum and maximum. The maximum signal (grayscale) intensity is then transformed to optical retardation by Fresnel equation as follows [43]

$$I = a + b \cdot I_0 \sin^2\alpha, \quad 0 \leq \alpha \leq \frac{\pi}{2} \quad , \tag{3.16}$$

where I_0 is the intensity of light illuminating the sample, I is the intensity of the passed light and a and b are constants which are specific for the optical system. The orientation-independent birefringence B can be calculated as follows [43]

$$B = \frac{\alpha \cdot \lambda}{\pi \cdot l} \quad , \tag{3.17}$$

where λ is the wavelength of the monochromatic light and l is the thickness of the microscopic section. The birefringence signal depends on the degree of collagen fibril organization [44].

Parallelism index (PI) represents the parallelism of the collagen fiber network in each pixel, *i.e.* anisotropy of the collagen matrix [43]. It is calculated using the minimum and maximum signal intensities (Equation 3.15). PI can be determined as Michelson's contrast parameter

$$\mathrm{PI} = \frac{I_{\mathrm{max}} - I_{\mathrm{min}}}{I_{\mathrm{max}} + I_{\mathrm{min}}} \quad . \tag{3.18}$$

In brief, PI is high when the fibers are parallel to each other and low when they are randomly oriented.

PLM ON BONE

PLM has been used to study the organization of collagen fibers in biological tissues. In particular, articular cartilage has been investigated extensively [40–45, 142], but also the organization of collagen matrix of bone has been examined [46–50]. In one study, PLM was used to investigate the collagen matrix organization in anterior and posterior quadrants in the mouse femur [46]. A greater fraction of collagen fibers was found to orientate along the longitudinal axis of the femur in the anterior quadrant than in the posterior quadrant. Another study used PLM to investigate the effects of growth and maturation on the collagen matrix organization of subchondral bone in horse metacarpophalangeal joint [47]. The basic orientation pattern of the collagen network was found to be established already at the age of 5 months and following loading of the joint subsequently modified the collagen orientation angle at least until the age of 11 months. PI decreased significantly between the ages of 11 months and 18 months. In another study, birefringence of the superior and interior femoral neck cortices of chimpanzee and human were determined using PLM [50]. They evaluated the loading patterns suggested by the anatomical structures of the femur necks. The birefringence of the cortices were found to be consistent with these loading patterns.

3.2.2 Micro-computed tomography

μCT has been used widely to study the microarchitecture of trabecular [51–62] and cortical bone [53,62,143,144]. From the sequential 2-dimensional images, obtained with a μCT system, quantitative indices describing the microarchitecture of bone in 3 dimensions can be calculated.

X-ray computed tomography

X-rays, like IR and visible light, are electromagnetic radiation that is generated in an X-ray tube as a result of *Bremsstrahlung*. X-ray tubes produce also monochromatic characteristic X-rays, which are used in various applications, *e.g.* in XRD. X-rays attenuate exponentially when they interact with matter. The attenuation, caused by photoelectric effect, Compton scattering and elastic scattering, follows the equation

$$I = I_0 e^{-\mu x} \quad , \tag{3.19}$$

where I is the intensity of the attenuated radiation, I_0 is the intensity of the incident radiation, x is the distance travelled in the matter and μ is the linear attenuation coefficient [145].

In computed tomography, 3-dimensional images are generated by reconstructing the projection images of the sample imaged from multiple directions. The projection images are taken at least 180° around the object. A 3-dimensional reconstruction of these 2-dimensional images is then obtained by using algorithms, such as filtered back projection or iterative reconstruction. In µCT, the sample is rotated between a stationary X-ray source and a detector, or the detector is rotated around the sample (*in vivo* µCT). The X-ray beam is magnified before it reaches the detector in order to create a magnified image of the object. This technique provides a voxel size (3-dimensional pixel) down to below one micrometer.

MICRO-COMPUTED TOMOGRAPHY ON TRABECULAR BONE

Quantitative parameters of the microarchitecture of trabecular bone can be obtained from the reconstructed µCT images (Table 3.4).

Table 3.4: Most common quantitative parameters of trabecular bone microarchitecture.

Parameter	**Abbreviation**	**Unit**
Bone volume fraction	BV/TV	%
Trabecular thickness	Tb.Th	µm
Trabecular separation	Tb.Sp	µm
Trabecular number	Tb.N	μm^{-1}
Structural model index	SMI	-
Degree of anisotropy	DA	-

BV/TV is calculated as the ratio between the bone volume and total volume in the region of interest (ROI). Tb.Th and Tb.Sp are the average thickness and separation of the trabeculae, respectively. Tb.N indicates the number of trabeculae encountered per µm. The structural model index (SMI) indicates the plate-rod-like structure of the trabeculae and ranges between values 0 and 3, which correspond to ideal plate- and rod-like structures, respectively [55, 63]. In Figure 2.2A the SMI is close to 0 and in Figure 2.2B the SMI is close to 3. The degree of anisotropy (DA) is defined as one minus the ratio between the minimal and maximal ratios of the mean intercept length of an ellipsoid fitted into the "empty space" between the trabeculae [55]. A value of 0 represents an ideal isotropic structure and a value of 1 a fully anisotropic structure.

μCT has been used to study *e.g.* the changes in trabecular bone microarchitecture during aging [51, 60, 61] and the anatomical location specific trabecular bone microarchitecture [51,56,60,61]. In one study, the microarchitecture of trabecular bone in the distal radius, T_{10} and L_2 vertebrae, iliac crest, femoral neck, greater trochanter and calcaneus of men and women aged 52-99 years were compared [60]. Additionally, the effect of aging on the microstructure of trabecular bone was evaluated. They found that in women the BV/TV decreased at most sites during aging. This change was associated with an increase in SMI and Tb.Sp and with a decrease in Tb.N. In men, the BV/TV of trabecular bone in greater trochanter was found to increase with age, but no other age related changes in trabecular bone microarchitecture were found. In another similar study, the microarchitecture of trabecular bone differed between men and women at some, but not all, sites [51]. The radius and femoral neck of men showed a more plate-like structure, higher Tb.Th, Tb.N and DA and a lower Tb.Sp compared to women. Both of the studies cited above, suggest that the trabecular bone microarchitecture is very heterogeneous throughout the skeleton.

3.2.3 Small angle X-ray scattering

X-RAY SCATTERING

When X-rays interact with an object, they may scatter from the electrons. X-ray radiation energy is much higher than the binding energy of an atom, thus the electrons behave as if they were free. The scattered waves are coherent. Incoherent Compton-scattering also occurs, but the scattering angle is greater and does not interfere with the X-rays scattered in small angles [146].

SAXS ON BONE

In SAXS, usually X-rays with a wavelength of $\sim$1 Å are used [146]. The sample is irradiated by a narrow collimated X-ray beam. The sample scatters the X-rays and those scattered in small angles are recorded. In bone, the scattering pattern is related to bone mineral structure, *i.e.* the spatial arrangement of mineral crystals. The 2-dimensional pattern is recorded with a detector behind the sample. Coupling SAXS with an automated scanning stage allows recording of spatial maps of the sample where each pixel contains a scattering pattern [68]. Parameters related to the bone mineral structure can be determined from the scattering pattern (Table 3.5). Mineral plate thickness should not be confounded with crystal size (length) determined with X-ray diffraction or crystallinity determined from IR or Raman spectra.

Table 3.5: Most common quantitative SAXS parameters of bone mineral structure.

Parameter	Explanation
Mineral plate thickness	The thickness of the mineral plates, *i.e.* size of the crystals.
Pre-dominant orientation	The orientation of the mineral plates (and collagen fibers).
Degree of orientation	The anisotropy of the orientation of the mineral plates (0 = no pre-dominant orientation, 1 = perfect alignment of the plates in pre-dominant orientation)

Mineral plate thickness, orientation and degree of orientation can be determined from the anisotropic 2-dimensional scattering pattern $I(q,\theta)$ (Figure 3.6A). First, the scattering pattern is averaged over 360° azimuthal range [64,65,67]. This results in a one-dimensional scattering pattern $I(q)$ where q is the q-range, usually around 0-0.5 Å^{-1} (Figure 3.6B) . From the one-dimensional scattering pattern, the mineral plate thickness, predominant orientation and degree of orientation can be evaluated by an approach suggested by Fratzl *et al.* [64–67]. In that approach, the bone is assumed to be a two component composite (mineral crystals in a collagen matrix). For large q-values, the scattered intensity $I(q)$ is expected to decay as Pq^{-4} according to Porod's law [146]. Porod constant P is given by

$$P = 2\pi\Delta\rho\frac{S}{V} \quad , \tag{3.20}$$

where $\Delta\rho$ is the scattering length density difference between the mineral and collagen, and $\frac{S}{V}$ is the total interfacial area per unit volume of the mineral crystals. For a binary mixture, the Porod invariant Q becomes

$$Q = \int q^2 I(q)\mathrm{d}q = 2\pi^2\Delta\rho^2\phi(1-\phi) \quad , \tag{3.21}$$

where ϕ is the volume fraction of *e.g.* mineral particles in the specimen [146]. The factor $(1-\phi)$ is the volume fraction of organic material in the specimen [65]. The thickness T of the thin plate like mineral particles is

$$T = \frac{2\phi}{S/V} \quad . \tag{3.22}$$

It can be estimated from the ratio between the Porod invariant and the Porod constant

$$T = \frac{2}{\pi(1-\phi)}\frac{Q}{P} \quad . \tag{3.23}$$

If $\phi = 0.5$ is assumed, then according to equation 3.22 $T = \frac{4}{S/V}$ which represents the average thickness of needle-shaped crystals [66]. With this assumption, from equations 3.23 and 3.21 the following equation can be formulated as

$$T = \frac{4}{\pi P}\int q^2 I(q)\mathrm{d}q \quad , \tag{3.24}$$

where the Porod constant is defined from the high q-values.

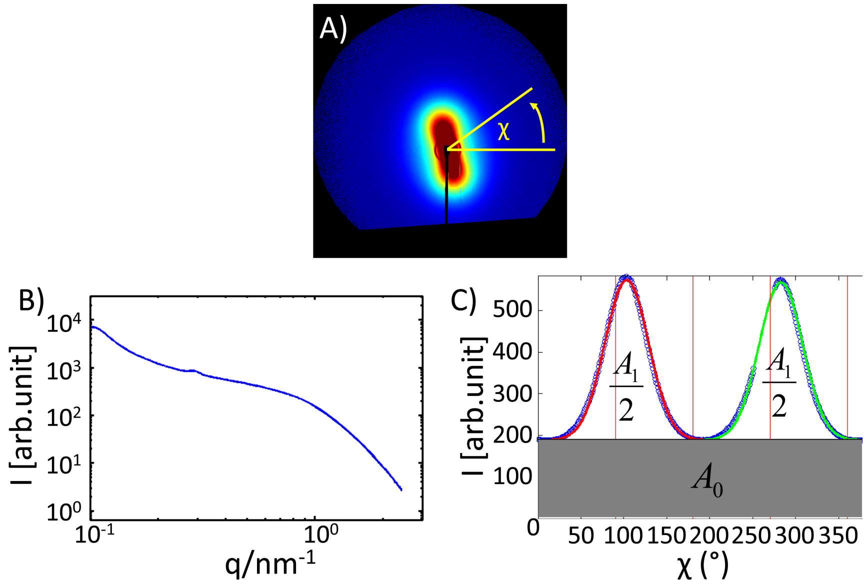

Figure 3.6: Typical SAXS 2D scattering pattern of bone A). The detector edges and the beamstop are masked away. Typical azimuthally integrated 1D scattering pattern of bone B). Q-averaged scattering intensity as a function of the scattering angle χ C).

Another approach to determine the mineral plate thickness was proposed by Bünger *et al.* [68]. It is based on a curve-fitting method where the mineral crystals are assumed to be plates with a finite thickness, T, in one dimension and infinite size in the other two dimensions. The scattering from one such plate is

$$P(q) = \frac{1}{q^2}\left|\frac{\sin(qT/2)}{qT/2}\right|^2 \quad , \tag{3.25}$$

where q is the q-range. Equation 3.25 is the *form factor* for a mineral crystal. The variation of the thickness of the mineral plates is taken into account by assuming the variation to follow a Schultz-Zimm distribution $D(T, T_{av})$. The average scattering then reads

$$P_{av}(q) = \frac{\int_0^\infty T^2 P(q) D(T, T_{av}) dT}{\int_0^\infty D(T, T_{av}) dT} \quad . \tag{3.26}$$

The equations 3.25 and 3.26 are valid for isolated particles. In bone, two crystals cannot occupy the same volume or location, which can be taken into account by using a random phase approximation (RPA)

$$P_{eff}(q) = \frac{P_{av}(q)}{1 + \nu P_{av}(q)} \quad , \tag{3.27}$$

where ν is an adjustable parameter which increases with elevating concentrations. Furthermore, large crystals are located close to each other and may even fuse. Thus, an effective structure factor $S_{frac}(q)$ is needed to describe the fractral fluctuations at low q values

$$S_{frac}(q) = 1 + Aq^{-\alpha} \quad , \tag{3.28}$$

where α is the fractral dimension of the fluctuations. The total intensity $I(q)$ of the model curve is then given by

$$I(q) = P_{eff}(q) S_{frac}(q) C \quad , \tag{3.29}$$

where C is the scale factor. The model curve in equation 3.29 is then fitted to the measured $I(q)$ data by an iterative weighted nonlinear least squares method by adjusting the mineral plate thickness T, the width of the Schultz-Zimm distribution, the RPA ν value, the scale factor C, and α and A.

The parameters related to orientation can be determined by calculating the q-averaged scattering intensity as a function of the scattering angle χ (Figure 3.6A) . The pre-dominant orientation can be calculated as $\Psi + 90^\circ$, where Ψ is the scattering angle χ where the intensity reaches its maximum [67, 147]. Degree of orientation φ can be determined by fitting Gaussian curves to both peaks (Figure 3.6C) and using the formula

$$\varphi = \frac{A_1}{A_0 + A_1} \quad . \tag{3.30}$$

Here A_1 is the sum area under the two Gaussian curves and A_0 the background area [67].

SAXS has been used to study the mineral structure of trabecular [67, 148, 149] and cortical bone [68, 148]. Callus tissue has received minor attention [150,151]. Here, a brief summary of selected publications is presented. In one study, FTIR and SAXS were used to study the composition and mineral structure of cortical and trabecular bone of on L-4 vertebra of a 14-month old girl [148]. The trabeculae were mapped and the results were compared to those of cortical bone. Mineral plate thickness and degree of orientation were lower in cortical bone than in trabecular bone. In another study, the effect of sodium fluoride and Alendronate (bisphosphonate) on the mineral structure of minipig vertebrae trabecular bone were studied [149]. In sodium fluoride treated animals, the mineral plate thickness was slightly increased, whereas no differences were found between alendronate treated animals and controls. Liu *et al.* studied the 3-dimensional orientation of the mineral crystals in callus tissue [150]. They analyzed five point regions of interest of callus tissue but did not report mineral plate thickness or degree of orientation analyses. They revealed that mineral particles are aligned in stacks and their predominant orientation lie in a single plane perpendicular to the fiber direction. In another study from the same group, the mineral plate thicknesses in fracture callus and fracture cortex were evaluated in sheep undergoing fracture healing [151]. They used the method proposed by Fratzl *et al.* and found a lower mineral plate thickness in fracture callus than in fracture cortex during fracture healing until 6 weeks. At 9 weeks after the fracture, the mineral plate thicknesses of the callus and the cortex were equal.

4 Aims of the present study

Bone tissue is constantly changing in response to maturation, aging and mechanical loading. New bone formation, such as that occurring in response to trauma and the subsequent fracture healing, can be regulated by different treatments. In this thesis, various methods were used to study the molecular composition, microarchitecture and mineral structure of bone and their contribution to bone quality during these events.

The specific aims of this thesis were:

- To study the normal changes in molecular composition and collagen architecture of rabbit cortical bone and microarchitecture of human trabecular bone during aging and maturation.
- To investigate the differences in molecular composition and microarchitecture of human trabecular bone at different anatomical locations with varying loading environments.
- To evaluate the molecular composition and mineral structure of newly formed callus tissue and previous existing cortical bone during long bone healing in rat femura.

5 Materials and methods

This thesis consists of four independent studies (**I-IV**). A summary of the materials and methods is presented in Table 5.1.

*Table 5.1: Materials and methods used in the studies **I-IV**. n = animals/cadavers.*

Study	Samples	n	Methods	Parameters
I	Rabbit humerus cortical bone, various ages	28	FTIR	M/M, C_B/M, C_B/P, XLR, Crystallinity
		28	Raman	M/M, C_B/M, C_B/P, Crystallinity
		28	µCT	BMD
		4	XRD	Crystal size
II	Rabbit femur cortical bone, various ages	50	FTIR	Amide I, XLR, 1660 cm^{-1}, 1690 cm^{-1}
		50	PLM	Retardation, orientation, parallelism index
		50	BA	Collagen content, HP
III	Male human trabecular bone, 3 anatomical sites	20	FTIR	M/M, C/M, C/P, XLR, Crystallinity
		20	µCT	BV/TV, Tb.Th, Tb.Sp, Tb.N, SMI, DA
		20	DXA	BMD
IV	Rat femur fractured and control cortex	12	FTIR	M/M, C/P, XLR, Crystallinity, APS
		12	SAXS	T, orientation, DoO
		12	µCT	Qualitative

M/M = Mineral/matrix ratio
C_B/M = Type-B carbonate/matrix ratio
C_B/P = Type-B carbonate/phosphate ratio
APS = Acid phosphate substitution
BV/TV = Bone volume fraction
Tb.Sp = Trabecular separation
SMI = Structural model index
T = Mineral plate thickness

C/M = Carbonate/matrix ratio
C/P = Carbonate/phosphate ratio
XLR = Collagen cross-link ratio
BMD = Bone mineral density
Tb.Th = Trabecular thickness
Tb.N = Trabecular number
DA = Degree of anisotropy
DoO = Degree of orientation

5.1 MATERIALS

5.1.1 Rabbit cortical bone

In studies **I** and **II**, the composition of cortical bone of female New Zealand White rabbits with varying ages was investigated [152]. The rabbits were euthanized as newborn, at the age of 11 days or 1, 3, 6 or 18 months. In study **I**, humeri from 11 days and 1-, 3- and 6-months old rabbits were used (n = 7 per group). In study **II**, femora from newborn, 1-, 3-, 6- and 18- months old rabbits were investigated (n = 10 per group).

In study **I**, the left and right humeri from each animal were harvested. The composition of the left humeri was assessed using FTIR and Raman microspectroscopy and the right humeri were subjected to μCT imaging and X-ray diffraction (XRD). The mid-diaphysis of the left humeri were dehydrated with ascending series of ethanolic solutions and subsequently embedded in polymethylmetacrylate (PMMA), *i.e.* bone cement. The embedded samples were cut in half. The first half was polished (Exact 400 CS, EXAKT Technologies Inc., Oklahoma City, OK) using silicon carbide paper with decreasing grit size. These samples were measured with Raman microspectroscopy (Figure 5.1 I). From the second half, 3 μm thick sections were cut with a microtome (Polycut S, Reichert-Jung, Germany). For FTIR microspectroscopic analyses (Figure 5.1 I), the sections were placed on Barium-Fluoride (BaF_2) windows. After the μCT imaging of the right humeri, the mid-diaphysis were dehydrated, defatted and ground to powder, using a ball mill and a mortar. The bone-powder was used in powder-XRD measurements to determine the HA crystal size.

In study **II**, the mid-diaphysis of the left femora had been subjected to 3-point-bending tests and subsequently decalcified using ethylene diaminotetraacetic acid (EDTA) [152]. The fractured site of the femora were cut and prepared for biochemical analysis (Figure 5.1 II). The adjacent 5 mm long fragments of cortical bone were embedded in paraffin and measured with FTIR and PLM (Figure 5.1 II). Five-μm-thick longitudinal sections were cut (LKB 2218 Historange microtome, Bromma, Sweden) and the paraffin was dissolved. The sections were placed on BaF_2 windows for FTIR measurements and on objective glasses for PLM. The PLM sections were covered with D.P.X (Difco, East Molesey, UK) and cover slips [43].

5.1.2 Human trabecular bone

In study **III**, trabecular bone samples from male human cadavers were harvested from the femoral neck, greater trochanter and calcaneus (Figure 5.1 III). The age range of the cadavers was 17-82 years of age (n = 20). Based on patient records, none of the cadavers had any known metabolic bone diseases. Dual energy X-ray absorption (DXA) measurements were conducted on the intact proximal femur and calcaneus. Thereafter, two trabecular bone samples (diameter 10 mm, length 10-15 mm) were taken from femoral neck, greater trochanter and calcaneus using a coring tool. The first samples were dehydrated and embedded in Technovit (EXAKT Technovit 7200 VLC, Heraeus Kulzer GmbH, Germany) and cut into 3 μm sections. The sections were placed on Zinc-Selenide (ZnSe) windows for FTIR measurements. The second samples were stored frozen in phosphate buffered saline (PBS) until imaging with μCT.

5.1.3 Rat cortical bone undergoing fracture healing

In study **IV**, 12 male Sprague-Dawley rats were anaesthetized with ketamine HCl (75 mg/mL, Parnell Laboratories, Roseberry Australia) and xylazine (10 mg/mL, Ilium, Smithfield, Australia) at 9 weeks of age [153, 154]. The right femurs were osteomized and the periosteum and muscle were stripped off. Thereafter the femurs were fixed with intramedullary 1.1 mm Kirschner wire. After the operation, BMP-7 was placed locally around the fracture and after 2 weeks zolendronate (ZO, bisphosphonate) or saline (sodium-chloride (NaCl)) was injected. Thus, the rats were divided into 4 groups with different treatments: A) NaCl, B) BMP-7 + NaCl, C) BMP-7 + ZO and D) ZO. After the operation, the rats received subcutaneous physiologic saline and buprenorphine (Temgesic, Reckitt and Colemann, Hull, UK) at 0.05 mg/kg twice a day. After 6 weeks the rats were sacrificed and both femora, fractured (right) and control (left), were harvested. The femora were stripped of the soft tissue, defatted, dehydrated and embedded in PMMA. From the PMMA embedded plugs, 3 μm thick longitudinal sections were cut and placed on SnZe windows for FTIR analyses and 300 μm sections were sawed (EXAKT 400 CS, Cutting grinding system, Hamburg, Germany) for SAXS analyses (Figure 5.1IV).

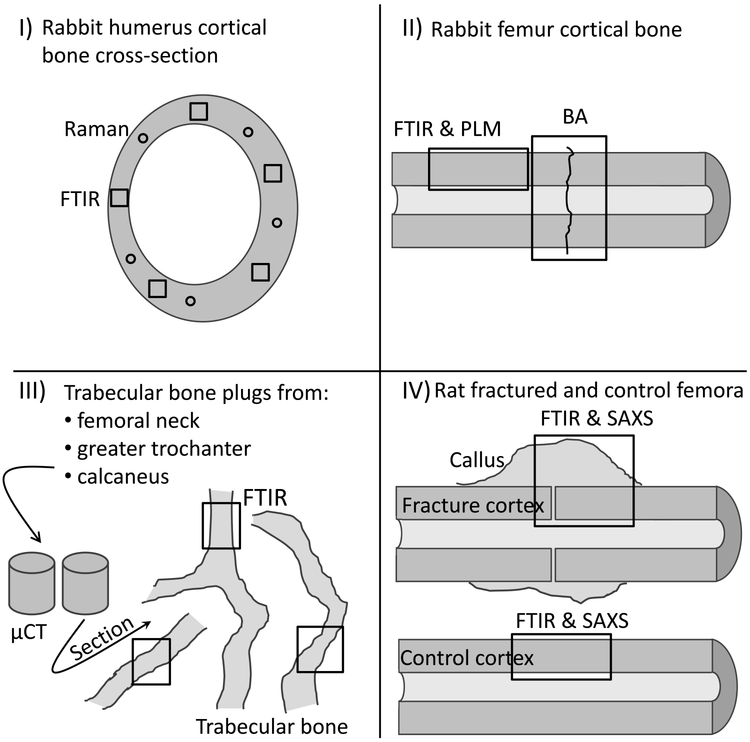

*Figure 5.1: Schematic presentation of the samples and measurement areas used in studies **I-IV**. In study **I**, the FTIR and Raman measurements were conducted in the center of cross-sectionally cut cortical bone I). In study **II**, the BA analyses were done on the site of the fracture (from 3-point bending test) and FTIR and PLM analyses adjacent to that II). In study **III**, trabecular bone plugs from femoral neck, greater trochanter and calcaneus were cored III). The FTIR measurements were done on sections cut from the plugs. In study **IV**, FTIR and SAXS spatial measurements were done on rat fracture callus and cortex and control cortex IV)*

5.2 METHODS

5.2.1 Analyses of bone composition

In studies **I-IV**, the composition of bone was evaluated using FTIR microspectroscopy (Perkin Elmer Spotlight 300, Waltham, MA), with a spatial resolution of 6.25 μm or 25 μm, spectral resolution of 4 cm^{-1} and 8 repeated scans in transmission mode. The background scan was performed for a clean IR window (BaF_2 or ZnSe) using the same measurement parameters, but with an average of 75 scans. Bone composition was analyzed using a wavenumber range of 2000-800 cm^{-1}. All FTIR and Raman compositional analyses were done using MatLab (The Mathworks, Inc., Natick, MA)

FTIR ON MINERALIZED BONE

In study **I**, spatial resolution of 6.25 μm was used for 5 areal measurements of cortical bone of each sample (Figure 5.1I). In addition, in study **III** spatial resolution of 6.25 μm was used for areal measurements on 3 trabeculae (Figure 5.1III). In study **IV**, spatial resolution of 25 μm was used for areal measurements consisting of the fracture callus and cortex or the control cortex (Figure 5.1IV). The background subtraction from the FTIR spectra is crucial, since the background interferes with the data. In studies **I**, **III** and **IV**, the effect of the embedding medium (PMMA in studies **I** and **IV**, and Technovit in study **III**) was minimized by normalizing the bone spectra using the spectrum of only the embedding medium [155]. Subsequently, the spectrum of the embedding medium was mathematically subtracted from the bone spectra [81,121]. Thus, the resulting spectra contained in principal only the data from the bone. Subsequently, pixels containing only embedding medium, *i.e.* pixels that had a spectrum close to zero after the subtraction, were masked from the maps. Mineral/matrix (M/M), carbonate/matrix (C/M) and carbonate/phosphate (C/P) ratios (using either total carbonate or type-B carbonate estimated through peak fitting) were determined from the respective peak areas in the bone spectra. Before the analyses, all peaks of interest were linearly baseline corrected (Figure 5.2). Collagen maturity, *i.e.* collagen cross-link ratio (XLR), and crystallinity were determined through peak fitting from the ratio of the underlying peaks at 1660 cm^{-1} and 1690 cm^{-1} [21], and 1030 cm^{-1} and 1020 cm^{-1} [23,24], respectively. Alternatively, in study **I**, the XLR was obtained directly from the spectrum as ratio of the intensities at 1660 cm^{-1} and 1690 cm^{-1} and compared to XLR determined through peak fitting. Additionally, in study **IV** the acid phosphate substitution (APS) was assessed as the ratio of the intensities at 1127 cm^{-1} and 1096 cm^{-1}. Furthermore, APS was determined also from the data in studies **I** and **III** (unpublished). The specific peak locations are presented in Table 3.2. In study **III**, three profiles per imaged trabecula were analyzed to evaluate the variation of the composition through the trabecular width. Subsequently, the individual profiles were averaged to obtain one profile per parameter per sample.

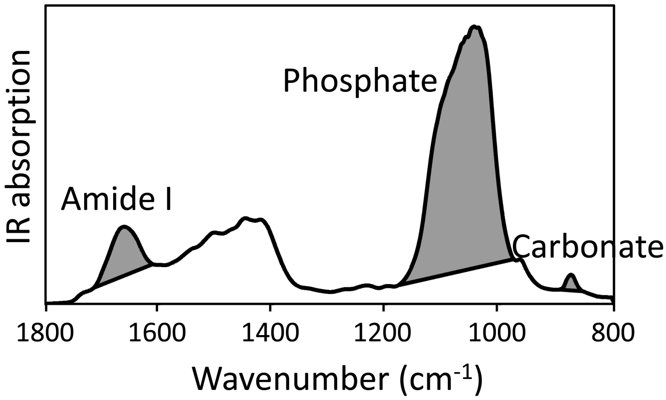

Figure 5.2: A typical IR spectrum of cortical bone in rabbit humerus. Linear baseline corrections and shaded peak areas indicate amide I, phosphate and carbonate peaks.

FTIR ON DEMINERALIZED RABBIT BONE

In study **II**, spatial resolution of 25 μm was used to image the cortex of each sample (Figure 5.1 II). The embedding medium (paraffin) was removed chemically before FTIR analyses, thus, in contrast to the analyses of mineralized bone, the spectrum of the embedding medium was not subtracted from the bone spectra, but the empty background, *i.e.* pixels with about zero spectra, was masked before the analyses. The organic matrix was analyzed from the amide I (1720-1585 cm^{-1}) and amide II (1585-1480 cm^{-1}) peak areas. The amide I peak area was used to evaluate the collagen content in bone [109]. XLR was determined through peak fitting as described earlier. Additionally, the peak areas of the underlying peaks at 1660 cm^{-1} (mature cross-links) and 1690 cm^{-1} (immature cross-links) [21] were studied. Furthermore, the spatial heterogeneity of the amide I and amide II maps were investigated by calculating a histogram of the map values and by fitting a Gaussian curve to the histogram (Figure 5.3A) [120]. The full width at half maximum (FWHM) of the fitted Gaussian curve was used as a parameter describing the spatial heterogeneity of the parameters, *e.g.* amide I map (Figure 5.3B). In brief, the FWHM is low when the spatial distribution is homogeneous and high when the spatial distribution is heterogeneous.

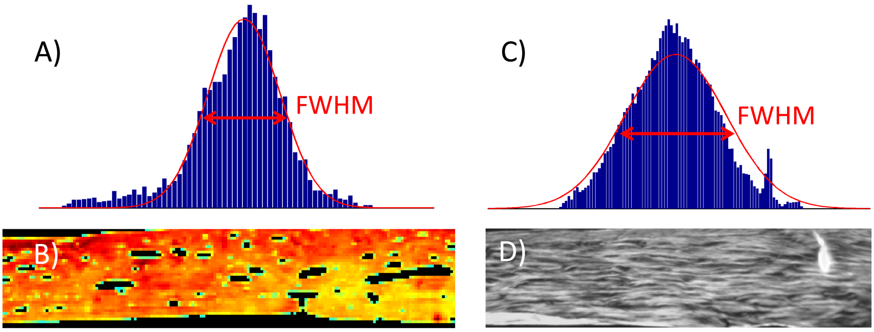

Figure 5.3: A histogram A) of the spatial distribution of a representative FTIR amide I map B) and a histrogram C) of the spatial distribution of a representative PLM optical retardation map D) of a 6 months old rabbit femur cortex. The FWHM is the indicator of spatial heterogeneity.

OTHER METHODS

RAMAN

In study **I**, the composition of bone was also evaluated with Raman microspectroscopy. The compositional parameters determined from the Raman bone spectra (Table 3.3, Figure 5.4) were compared with those of the FTIR bone spectra (Figure 5.2). The parameters were determined using the Raman peak intensities.

The measurements were conducted with a dispersive Raman microscope (Senterra 200LX, Bruker Optics GmbH, Ettlingen, Germany). The wavelength of the laser was 785 nm with a power of 100 mW. 20 × magnification and a numerical aperture (NA) of 0.5 were chosen. With the used magnification and NA, the polarization effect is relatively small [140]. Five point measurements per sample were performed and each determination was repeated five times with 60 s exposure time (Figure 5.1 I). The wavenumber range of the collected Raman scattered photons was 4000-127 cm^{-1}. The laser beam was focused 10 μm below the bone surface to ensure that the measured Raman scattered photons originated from the bone tissue. PMMA spectrum was also recorded using identical settings. Before the compositional analyses, the PMMA spectrum was subtracted from the bone spectra and the wavenumber band was limited to 2000-800 cm^{-1} and from this band, the cosmic spikes were removed. The fluorescence effect was subtracted by baseline correction according to an earlier study by iteratively fitting a fifth-degree polynomial baseline curve which was subsequently subtracted from the bone spectra [156].

BIOCHEMICAL ANALYSIS

In study **II**, high-pressure liquid chromatography (HPLC) was used to analyze the collagen content and the collagen cross-linking in bone (Figure 5.1 II). After demineralization, the excess EDTA was removed by washing the samples. The samples were weighed,

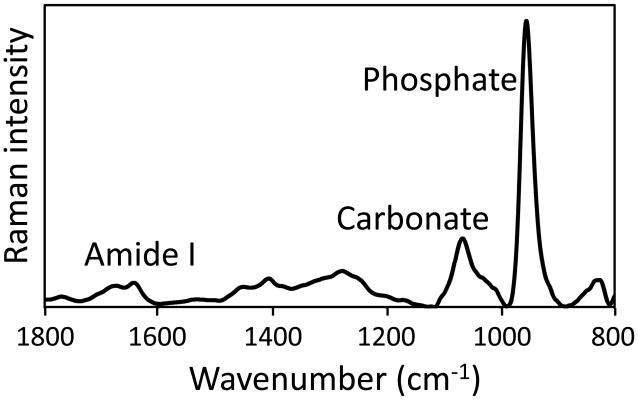

Figure 5.4: A typical Raman spectrum of cortical bone in rabbit humerus. Amide I, phosphate and carbonate peaks are indicated.

freeze-dried and hydrolyzed in 6 M HCl. The amount of collagen was calculated by assuming 300 mol of hydroxyproline per 1 mol of collagen [157]. A mature enzymatic collagen cross-link hydroxylysyl-pyridinoline (HP) was measured using reversed-phase HPLC analysis [152]. The collagen content was compared to the FTIR spectrum amide I peak area, which represents the collagen content, and HP content was compared with both underlying peaks at 1660 cm^{-1} (mature cross-links) and 1690 cm^{-1} (immature cross-links).

5.2.2 Analyses of bone structure

PLM ON DEMINERALIZED RABBIT BONE

In study **II**, two longitudinally cut sections of rabbit femur cortical bone from each sample were imaged with PLM (Leitz Orholux II POL, Leitz Wetzlar, Wetzlar, Germany) (Figure 5.1 II). Images were taken using monochromatic light (594 nm wavelength) that was guided through the system (Figure 3.5). Polarizers were rotated with computer-controlled tables and two monochromators (591.4 ± 10 nm, Schott, Germany and 594 ± 3 nm, XLK10, Omega Optical, Inc., Brattleboro, VT) were used to adjust the final wavelength of the light (594 ± 3 nm). Images were taken with a Peltier-cooled CCD camera (Photometrics SesSys, RoperScientific, Tuscon, AZ). The system was controlled on a computer using IpLab 3.5.5 software (Scanalytics, Inc., Fairfax, VA) [43].

The polarizer pair were rotated stepwise at 0, 15, 30, 45, 60, 75 and 90°. An additional image was taken at the 90° polarizer pair position after placing the $\lambda/4$ phase shift plate into the light path. The background was corrected for each polarizer pair angle. From the images, optical retardation (birefringence), orientation and parallelism index were calculated in each pixel as introduced in section 3.2.1. Optical retardation has been suggested to reflect the collagen content and anisotropy [43,44,158]. The orientation angle of the collagen fibers was determined against the normal to the bone surface, *i.e.* collagen fibers perpendicular and parallel to the bone surface had orientation angles of 0° and 90°, respectively. Additionally, the spatial heterogeneity of the orientation and parallelism index maps were investigated by obtaining a histogram of the map values and by fitting a Gaussian curve to the histogram (Figure 5.3C) [120]. The FWHM of the fitted Gaussian curve was used as a parameter describing the spatial heterogeneity of the parameters. All PLM maps were analyzed using MatLab (MatLab 7.6.0, The Mathworks, Inc., Natick, MA).

μCT ON HUMAN TRABECULAR BONE

In study **III**, the structural parameters of trabecular bone were determined using a high resolution μCT system (SkyScan 1172, Aartselaar, Belgium) (Figure 5.1 III). The samples were thawed just prior to imaging. Images were acquired with an isotropic voxel size of 14 μm, using settings of 100 kV, 100 μA, a 0.5 mm aluminum filter and 10 repeated scans. For mineralized bone tissue, a grayscale threshold value range of 65-255 was used. A ROI of 8 mm was selected and typical structural parameters describing the microarchitecture of trabecular bone were quantified (Table 3.4). All analyses were performed in CTAn (v. 1.11.10.0, SkyScan, Aartselaar, Belgium).

5.2.3 Analyses of bone mineral structure

SAXS on fractured rat femora

In study **IV**, the mineral structure of fracture callus and cortex of rat femora where studied using SAXS (Figure 5.1 IV). The measurements were conducted at the I911-SAXS beamline at the 1.5 GeV ring (MAX II) of the MAX IV Laboratory (Lund University, Lund, Sweden) (Figure 5.5) [159].

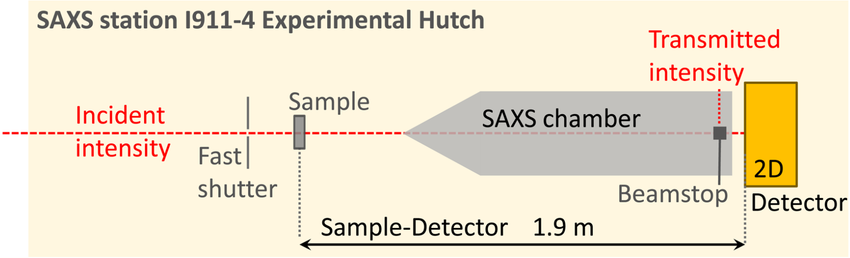

Figure 5.5: Layout of the I911-SAXS beamline experimental hutch in the MAX IV Laboratory.

Monochromatic radiation with a wavelength of 0.91 Å was obtained from a Si(111) crystal. The size of the collimated synchrotron X-ray beam at the sample was approximately 0.2×0.2 mm^2. The detector (MarCCD, Rayonix, L.L.C.) had a 165 mm active area and 79 µm pixel size. The detector was placed 1911 mm behind the sample and the exposure time was 5 s per measurement point. The detected q-range was 0.01 - 0.30 Å^{-1}. Bone sections were mounted in a sample holder that was placed in a motorized x-y scanning stage. The samples were mapped with a step size of 0.2 mm in both directions. The measurement areas included the fracture callus and cortex or the control cortex (Figure 5.1 IV). The mineral plate thickness, predominant orientation and degree of orientation were determined at each measurement point (Figure 5.6) as introduced in section 3.2.3. The mineral plate thickness was measured using the methods proposed by Fratzl *et al.* [64,65,67] and Bünger *et al.* [68].

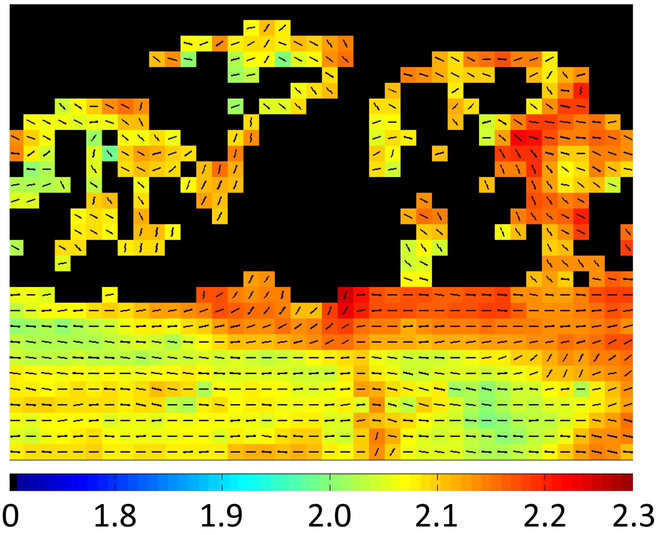

Figure 5.6: Point-by-point measured SAXS maps of fracture callus and cortex. In each pixel, the color map indicates the mineral plate thickness (T) determined using the method proposed by Fratzl et al. *[64, 65, 67], the line orientation indicates the orientation of the crystals, and the length of the line indicates the degree of orientation of the crystals. The line lengths are scaled as a line covering the whole pixel width represents a degree of orientation of 1.*

XRD ON RABBIT BONE

In study **I**, the size of the HA crystals was determined using powder-XRD. The powdered bone was spread on a sample holder (Siemens D5000 diffractometer). Copper K_α radiation at 40 kV and 40 mA was used. The HA crystal size was evaluated by scanning the c-axis (002) and cross section (310) at 2θ range of 24.8° - 27° and 38.4° - 41.5°, respectively [69, 70], with a step size of 0.040°. Scans were performed at a speed of 100 s per step, and duplicate measurements were conducted for the sample in each age group.

The size of the HA crystals is associated with the broadening of the apatite peaks and thus the HA crystal size was evaluated from the FWHM of the relative peaks. Instrument broadening can affect the peak broadening ($\beta_{1/2}$, FWHM of the peak). Thus a highly crystalline mineral fluoroapatite was used as a standard to correct for any peak broadening caused by the instrument itself. The corrected $\beta_{1/2}$ values were used in the Scherrer equation [71]

$$D = \frac{k\lambda}{\beta_{1/2}\cos\theta} \quad , \tag{5.1}$$

to calculate D values, which relate to the size of the HA crystal , *i.e.* the length of the HA crystal (002), and the cross-section of the HA crystal (310) [70]. In equation 5.1, k is a constant approximately equal to unity, λ is the X-ray wavelength and θ is the diffraction angle.

5.2.4 Analyses of BMD

Bone mineral density can be evaluated using different X-ray based methods, *e.g.* CT, μCT and DXA. Generally, with increasing density, the X-ray absorption increases and the BMD can be determined from the intensity images after the calibration of the system.

In study **I**, the BMD was estimated using μCT (Skyscan 1172, v. 1.5, Skyscan, Aarselaar, Belgium). The right humeri of the rabbits were imaged using an isotropic voxel size of 15 μm. After the reconstruction of the images, the mid-diaphysis was identified and the ROI was located at approximately 1 mm proximal and distal to the mid-diaphysis. The BMD distribution was calculated on each 2D image between the proximal and distal boundaries. The calibration of the BMD was done according to the manufacturer's protocol using water and two HA phantoms of known density (0.25 and 0.75 g/cm^3). A threshold of 0.20 g/cm^3 was assigned for mineralized bone. The average BMD of each sample was calculated using the voxels that exceeded the threshold.

In study **III**, the BMD of the human proximal femur and calcaneus was evaluated with DXA (Lunar Prodigy Advance, GE Healthcare, Madison, WI), using a clinical hip measurement protocol. The soft tissue was simulated by immersing the bones into 10 liter of PBS in a plastic container. The samples were positioned according to the *in vivo* anatomy and all measurements were done in duplicate. The BMDs of femoral neck, greater trochanter and calcaneus were determined from the DXA images.

The BMD evaluated with DXA yields areal BMD values while µCT provides volumetric BMD values. Thus, these two values are not directly comparable.

5.2.5 Statistical analyses

The statistical analyses in studies **I-IV** were conducted using the SPSS software (SPSS Inc., Chicago, IL) or MatLab (MatLab 7.6.0, The Mathworks, Inc., Natick, MA). The limit of statistical significance in all statistical tests was set to $p < 0.05$.

In study **I**, the non-parametric Mann-Whitney U-test was used to compare the parameters between consecutive age groups. The non-parametric Kruskall-Wallis post-hoc test was used to study the changes in the parameters over the whole maturation period. Pearson's correlation test was used to evaluate the associations and matching of similar parameters determined from FTIR and/or Raman spectra and between M/M ratio and BMD.

In study **II**, the non-parametric Kruskall-Wallis post-hoc test was used to compare each parameter between the age groups. Pearson's correlation test was used to evaluate the association between FTIR and BA determined parameters. The root mean square (RMS) coefficient of variation (CV%) were calculated for all parameters. The correlation coefficients were compared to each other using the statistical analysis for dependent correlation elements according to Steiger [160]. Linear regression analysis was used to determine the contributors to optical retardation.

In study **III**, Wilcoxon signed ranks test was used to test the differences between the compositional and structural parameters from the three anatomical locations. Pearson's correlation test was used to evaluate the age-dependency of the parameters and the associations between the parameters in different anatomical locations. A linear regression model was used to estimate the explanation level of composition and microarchitecture to the BMD of trabecular bone.

In study **IV**, the average ± standard deviation (SD) values were compared between the measurement locations. Wilcoxon signed ranks test was used to compare each parameter at the locations when all measurements from each location were pooled and to compare the mineral plate thicknesses determined with the analysis methods proposed by Fratzl *et al.* [64, 65, 67] and Bünger *et al.* [68]. Pearson's correlation test was used to evaluate the linear correlation between the parameters recorded by SAXS and FTIR.

6 Results

The main results from studies **I-IV** are summarized in this chapter. All the results can be found in the original articles **I-IV**.

6.1 AGE RELATED CHANGES IN BONE

6.1.1 Composition

Mineralized bone

Generally, the M/M ratio, C/M ratio and C/P ratio are expected to increase with aging of bone. In study **I**, these parameters increased in rabbit humerus cortical bone with age when studied with FTIR and Raman microspectrospy (Figure 6.1A_R, B_R and C_R, respectively). Moreover, significant correlations were revealed between the parameters determined from IR and Raman spectra (indicated in Figure 6.1A_R, B_R and C_R). In study **III**, M/M ratio and C/M ratio were found to increase with aging (Figure 6.1A_H and B_H, respectively) in trabecular bone in human greater trochanter and calcaneus, whereas C/P ratio showed no significant change during aging (Figure 6.1C_H). Additionally, APS decreased significantly during the maturation of rabbit humerus (Figure 6.1D_R) and decreased with age in trabecular bone in human calcaneus but not in greater trochanter (Figure 6.1D_H). Crystallinity showed no significant changes with rabbit age (Figure 6.2A) or human age (Figure 6.2B) although HA crystal size, determined with powder-XRD, clearly increased from young to mature rabbits (Figure 6.2C).

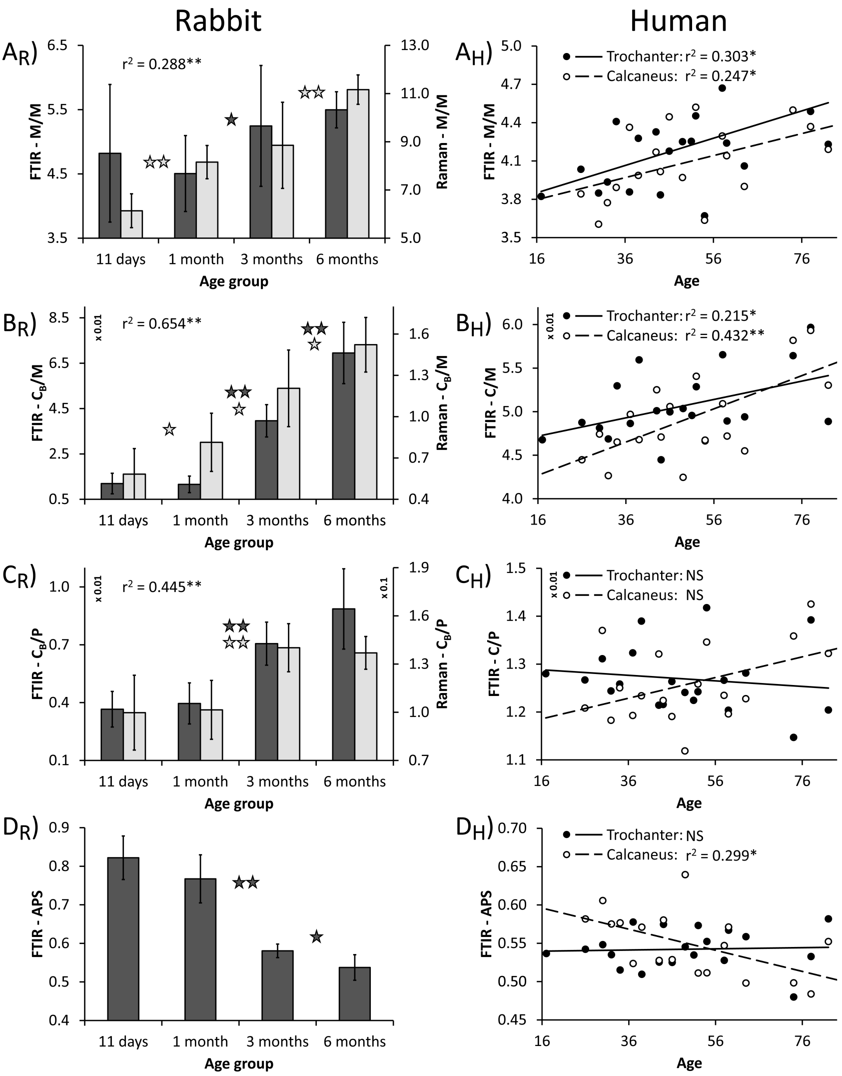

*Figure 6.1: Changes in composition of rabbit cortical bone with FTIR (dark gray) and Raman (light gray) and human trabecular bone with FTIR. In rabbit, the effect of maturation on degree of mineralization (M/M ratio) A_{R}), type-B carbonate to matrix ratio (C_{B}/M) B_{R}), type-B carbonate substitution (C_{B}/P ratio) C_{R}) and acid phosphate substitution (APS) D_{R}) are shown by comparing consecutive age groups (Mann-Whitney U-test). In human, the effect of aging to the similar parameters is revealed by correlating (Pearson's correlation) the parameter values with age. Unlike for rabbits, for human data the total carbonate to matrix ratio (C/M ratio) B_{H}), and total carbonate substitution (C/P ratio) C_{H}) were determined. The significance of the differences between age groups and the correlations are indicated *** $p < 0.01$, *** $p < 0.05$, NS = *not significant.*

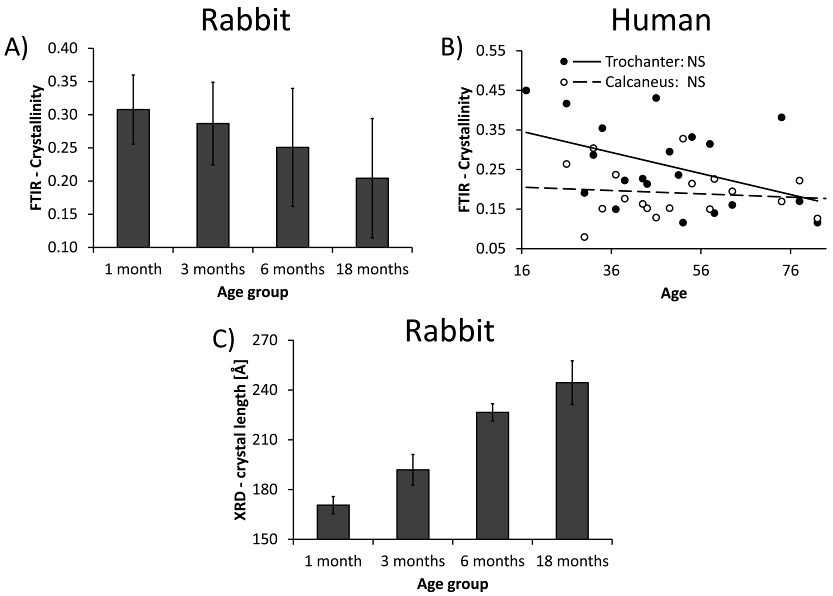

Figure 6.2: Changes in crystallinity in cortical bone in rabbit humerus A) and trabecular bone in human greater trochanter and calcaneus B). No significant differences were found in crystallinity during maturation of rabbits and no significant correlations (Pearson's correlation) were observed between crystallinity and human age. c-axis length of the HA crystals, determined with XRD, clearly increased during maturation of rabbit bone C). Since only two samples per age group were measured, no statistical analyses could be performed. In Pearson's correlations NS = *not significant.*

DEMINERALIZED RABBIT BONE

In study **II**, collagen content in demineralized cortical bone of rabbit femura was determined with BA and using the amide I peak area in the IR spectra. Based on both methods, collagen content increased significantly from newborn to skeletally mature rabbits (Figure 6.3A). Furthermore, optical retardation, a possible indicator of collagen content and anisotropy, increased significantly from newborn to 1 month old rabbits (Figure 6.3B). From the IR spectra determined amide I peak area correlated significantly with collagen content determined with BA (r^2 = 0.446, $p < 0.01$) and with optical retardation determined from PLM images (r^2 = 0.740, $p < 0.01$). Correlation between optical retardation and collagen content was also significant (r^2 = 0.377, $p < 0.01$). The HP content, determined with BA, increased with age from newborn until 6 months old rabbits (Figure 6.3C) and correlated significantly with 1690 cm^{-1} (r^2 = 0.233, $p < 0.01$) and 1660 cm^{-1} (r^2 = 0.269, $p < 0.01$) peak areas determined from IR spectra (Figure 6.3D). XLR was found to increase significantly until 3 months of age in rabbit femur and humerus (Figure 6.3E). Furthermore, the spatial heterogeneity of amide I and amide II maps decreased significantly from newborn until 3 month old rabbits (Figure 6.4) indicating a more homogeneous spatial distribution of these components with age.

6.1.2 Collagen fiber organization

In addition, the heterogeneity of orientation and parallelism index of collagen fibers, determined with PLM, decreased significantly from newborn until 3 months old rabbits (Figure 6.4). The actual orientation increased until 3 months of age (data not shown), whereas no significant changes with age were observed in the actual parallelism index (data not shown).

6.1.3 Microarchitecture

Some µCT parameters of the microarchitecture of human trabecular bone changed with age. According ton the linear correlations, it seemed that the SMI (Figure 6.5A) in greater trochanter increased whereas DA (Figure 6.5B) decreased significantly with age (r^2 = 0.375, p < 0.01 and r^2 = 0.256, p < 0.05, respectively). This result indicates a more isotropic rod-like structure with increasing age.

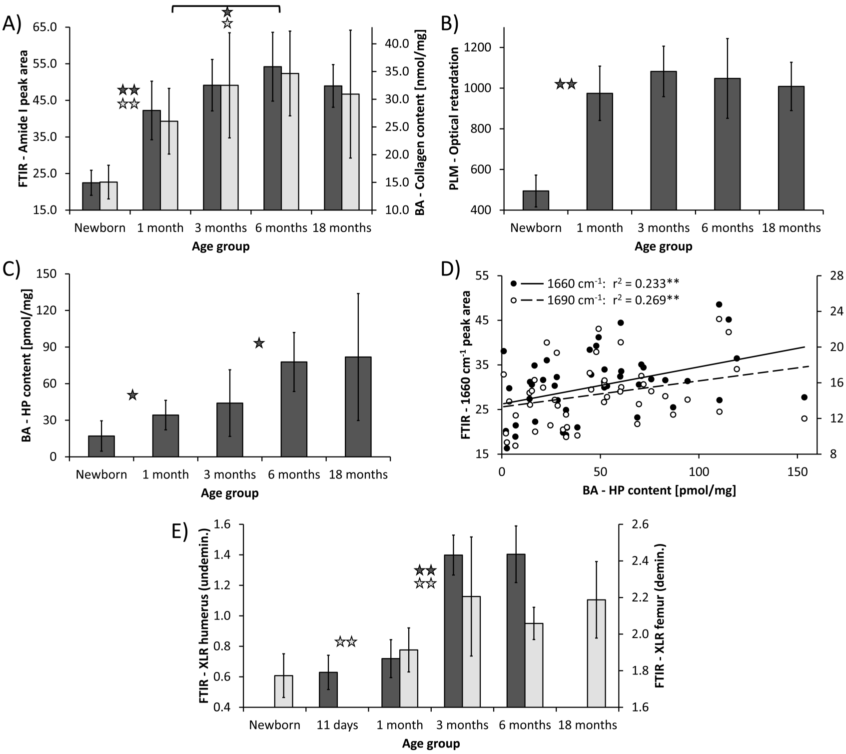

*Figure 6.3: Changes in collagen content (light gray) and amide I peak area (dark gray) A), optical retardation B), HP collagen cross-links C) and mature to immature collagen cross-linking ratio E) during maturation of rabbit. Additionally, a correlation plot between HP cross-links and from IR spectra determined mature (1660 cm^{-1}) and immature (1690 cm^{-1}) cross-links is presented D). Changes in collagen cross-linking ratio in undemineralized (dark gray) and demineralized (light gray) rabbit bone. Significant differences between age groups, based on the Kruskall-Wallis post hoc test, and significant (Pearson's) correlations are indicated, *** $p < 0.01$, * $p < 0.05$.

6.2 DIFFERENCES BETWEEN ANATOMICAL LOCATIONS

Human femoral neck, greater trochanter and calcaneus are found in different anatomical locations in human body. They experience different loading environments and the remodeling rates may vary [4,161–165]. Thus, the composition and microarchitecture and subsequently the density of trabecular bone might vary between the anatomical locations. Indeed, the BMD of femoral neck was signif-

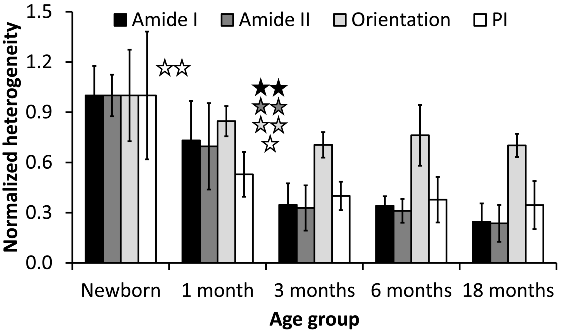

*Figure 6.4: Spatial heterogeneity of amide I and amide II maps, measured with FTIR, and orientation and parallelism index (PI) from PLM images. The normalized (to maximum) means ± SD for age group are presented. Significant differences between age groups are indicated (stars between adjacent groups), (Kruskall-Wallis post-hoc test, *** $p < 0.01$, *** $p < 0.05$.)

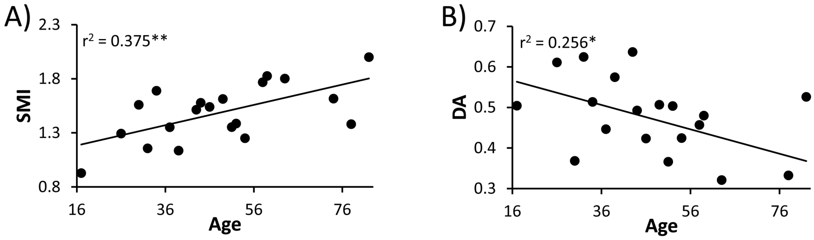

*Figure 6.5: Linear correlation between SMI A) and DA B) in greater trochanter with age. Pearson's correlation *** $p < 0.01$, *** $p < 0.05$.

icantly higher than in greater trochanter and calcaneus ($p < 0.01$ in both) and BMD in greater trochanter was higher than in calcaneus ($p < 0.01$) (Table 6.1).

6.2.1 Trabecular bone composition

The compositional results of trabecular bone in the femoral neck, greater trochanter and calcaneus are presented in Table 6.1. The M/M ratio was higher in greater trochanter than in femoral neck (non-sig.) and calcaneus ($p < 0.05$). No significant differences were found in C/M ratio and C/P ratio between the locations when the whole measured trabeculea were analyzed. XLR was significantly

*Table 6.1: Mean ± SD values of BMD and compositional and microarchitectural parameters of trabecular bone in femoral neck, greater trochanter (Trochanter) and calcanues. Significant differences between parameters of anatomical locations are based on Wilcoxon signed ranks test, *** $p < 0.01$, ** $p < 0.05$*. * between femoral neck and greater trochanter, ${}^{\#}$ between femoral neck and calcaneus and † between greater trochanter and calcaneus.*

Method	Parameter	Femoral neck	Trochanter	Calcaneus
DXA	BMD	$0.92\pm0.18^{**\#\#}$	$0.87\pm0.20^{\dagger\dagger}$	0.61 ± 0.15
FTIR	M/M ratio	4.1 ± 0.2	$4.2\pm0.3^{\dagger}$	4.1 ± 0.3
	C/M ratio	0.049 ± 0.004	0.051 ± 0.004	0.049 ± 0.005
	C/P ratio	0.012 ± 0.001	0.012 ± 0.001	0.012 ± 0.001
	XLR	$2.4\pm0.1^{**}$	$2.2\pm0.2^{\dagger}$	2.3 ± 0.2
	Cryst	$0.3\pm0.1^{\#}$	0.3 ± 0.1	0.2 ± 0.1
	APS	$0.51\pm0.4^{**\#}$	0.54 ± 0.3	0.55 ± 0.04
μCT	BV/TV	$18\pm7^{**}$	$12\pm3^{\dagger\dagger}$	17 ± 4
	Tb.Th	$180\pm33^{**\#}$	147 ± 18	157 ± 20
	Tb.N	$1.0\pm0.2^{**\#\#}$	$0.8\pm0.1^{\dagger\dagger}$	1.1 ± 0.2
	Tb.Sp	$789\pm106^{\#\#}$	$771\pm100^{\dagger\dagger}$	637 ± 116
	SMI	$0.9\pm0.5^{**\#\#}$	$1.5\pm0.3^{\dagger}$	1.2 ± 0.2
	DA	$0.58\pm0.09^{**\#\#}$	$0.48\pm0.10^{\dagger\dagger}$	0.64 ± 0.12

lower in greater trochanter than in femoral neck and calcaneus ($p < 0.01$ and $p < 0.05$, respectively). Crystallinity was lowest in calcaneus and a significant difference was observed between calcaneus and femoral neck ($p < 0.05$). APS was significantly lower in femoral neck than in greater trochanter and calcaneus ($p < 0.01$ and $p < 0.05$, respectively). The cross-sectional profiles of the C/P ratio and the C/M ratio were significantly lower in the center (40-80 % of the cross-sectional profile) of the trabeculae in the femoral neck in comparison to the calcaneus ($p < 0.05$ in both parameters) (Figure 6.6).

6.2.2 Trabecular bone microarchitecture

The microstructural results of trabecular bone in the femoral neck, greater trochanter and calcaneus are presented in Table 6.1. BV/TV was lower in greater trochanter than in femoral neck and calcaneus

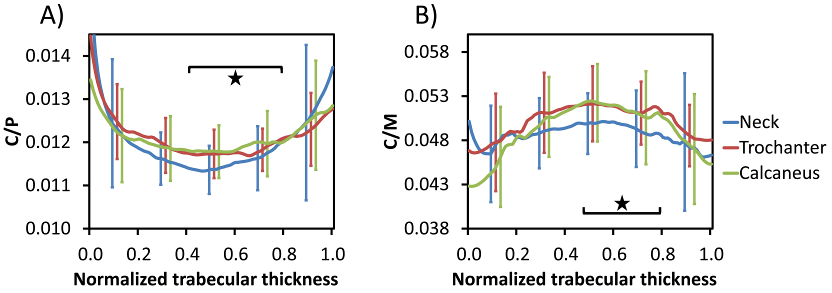

*Figure 6.6: C/P ratio A) and C/M ratio B) profiles over trabeculae in femoral neck, greater trochanter and calcaneus. Mean values with SD are presented. Both profiles are significantly lower in the center of the profile (middle of the trabecula, older bone) in femoral neck than in calcaneus. Wilcoxon signed ranks test * p < 0.05.*

($p < 0.01$ in both). Tb.Th was higher in femoral neck than in greater trochanter ($p < 0.01$) and calcaneus ($p < 0.05$). Tb.N was higher and Tb.Sp was lower in calcaneus compared to femoral neck (Tb.N: $p < 0.05$ and Tb.Sp: $p < 0.01$) and greater trochanter (Tb.N and Tb.Sp: $p < 0.01$). A lower Tb.N was also found in greater trochanter compared to femoral neck ($p < 0.01$). SMI was lower in femoral neck than in greater trochanter and calcaneus ($p < 0.01$ and $p < 0.05$, respectively) and lower in calcaneus compared to greater trochanter ($p < 0.05$). DA was highest in calcaneus, second highest in femoral neck and lowest in greater trochanter ($p < 0.01$ between all pairs).

6.3 BMD, COMPOSITION AND MICROARCHITECTURE

BMD describes the overall mineral density in bone. The density is affected by the structure of bone but also by the amount of mineral in the bone. BMD is insufficient to distinguish the effects of structural density and mineral amount.

In study **I**, the BMD of cortical bone in rabbit humerus was determined with μCT. The BMD was found to increase significantly with age and it correlated significantly with M/M ratio, *i.e.* the degree of mineralization, determined from IR ($r^2 = 0.232$, $p < 0.05$) and Raman bone spectra ($r^2 = 0.503$, $p < 0.01$).

In study **III**, the BMD of trabecular bone in human femoral neck, greater trochanter and calcaneus were determined using DXA. Linear regression models explaining the BMD using structural and compositional parameters revealed that only BV/TV and Tb.N exhibited significant partial correlations in the models (Table 6.2). When M/M ratio was added to the model, the explanatory power increased, although partial correlation of the M/M ratio was not significant by itself. The highest explanatory power of the BMD was obtained from the combination of BV/TV and M/M ratio, and Tb.N and M/M ratio. Both models yielded similar results in all anatomical locations, but the R^2 value was greatest in femoral neck.

Table 6.2: Linear regression models for explaining the variation in BMD in the different anatomical locations. Explanatory power (R^2*) is shown in bold. Partial correlations of the model parameters are also presented. *** $p < 0.01$, *** $p < 0.05$.

Model		**Femoral neck**	**Trochanter**	**Calcaneus**
BV/TV, M/M ratio	R^2	**0.592**	**0.447**	**0.401**
BV/TV	Part. corr.	0.762**	0.667**	0.527*
M/M ratio	Part. corr.	0.446	-0.088	0.095
Tb.N, M/M ratio	R^2	**0.654**	**0.414**	**0.384**
BV/TV	Part. corr.	0.802**	0.641**	0.508*
M/M ratio	Part. corr.	0.393	-0.085	0.067

6.4 FRACTURE CALLUS AND CORTEX

In study **IV**, only small amounts of new callus tissue was found in NaCl group, based on the μCT images. In this animal model, untreated fractures result in 50 % non-union [153]. Some mineralized callus tissue was forming between the fracture ends but the union was not complete. Based on the μCT images, all fractures in the BMP-7+NaCl and BMP-7+ZO groups were judged as completely healed. The callus size in the BMP-7+ZO group was larger than in the other groups.

The parameters describing the composition and mineral structure were averaged in the fracture callus, fracture cortex and control cortex in each treatment group. Additionally, all treatment groups were pooled and the parameters were averaged for each location.

6.4.1 Composition

The results of the tissue composition in the control cortex, fracture cortex and fracture callus are presented in Figure 6.7. When all samples were pooled, the M/M ratio (Figure 6.7A) and XLR (Figure 6.7C) were significantly lower in fracture callus than in fracture cortex (p < 0.01 and p < 0.05, respectively) and control cortex (p < 0.05 and p < 0.01, respectively). Crystallinity (Figure 6.7D) was significantly lower in control cortex than in the fracture cortex and callus (p < 0.01 in both). APS (Figure 6.7E) was significantly higher in the fracture callus as compared to control and fracture cortices (p < 0.05 and p < 0.01, respectively).

In all treatment groups, M/M ratio was lower in callus tissue than in the cortices (data not shown). The M/M ratio was similar in the fracture and control cortices. The C/P ratio was similar in all samples regardless of the location. In animals treated with BMP-7 and/or ZO, the XLR tended to be lower in callus tissue than in the cortex bone, whereas no differences were observed in the NaCl group. Crystallinity was higher in the fracture cortex and callus tissue than in the control cortex. This was seen especially in the BMP-7 and/or ZO treated samples. ASP was higher in fracture callus than in the fracture and control cortices in all treatment groups.

6.4.2 Mineral structure

The results of the mineral plate thickness determined using the different methods are presented in Figure 6.8A. The results were dependent on the method used for analysis. No differences between the locations were observed when analyzed using the method proposed by Fratzl *et al.* (Figure 6.8A). The curve fitting technique resulted in higher (12 %, p < 0.01) values of mineral plate thickness than the method proposed by Fratzl *et al.* (Figure 6.8A). The curve fitting results showed that the fracture cortex had a lower mineral plate thickness than the control cortex and the fracture callus. The

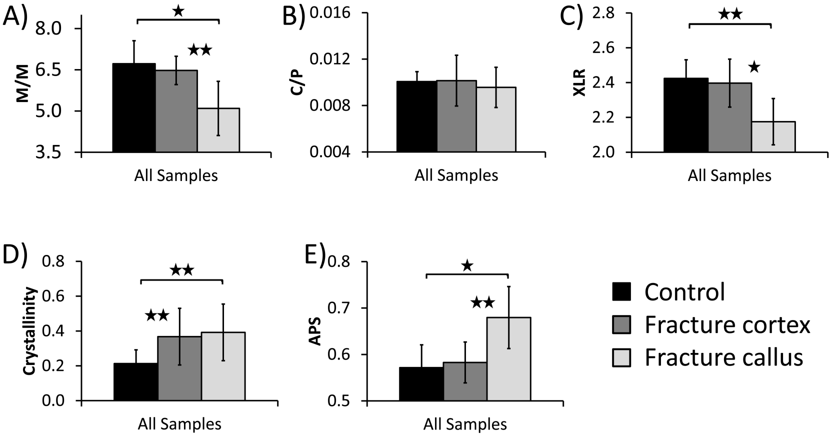

*Figure 6.7: Results of FTIR compositional analyses of M/M ratio A), C/P ratio B), XLR C), crystallinity D) and APS E) in control cortex, fracture cortex and fracture callus for all samples. Non-parametric Wilcoxon signed rank test ** $p < 0.01$, * p 0.05.*

difference between fracture callus and fracture cortex was statistically significant ($p < 0.05$) (Figure 6.8A).

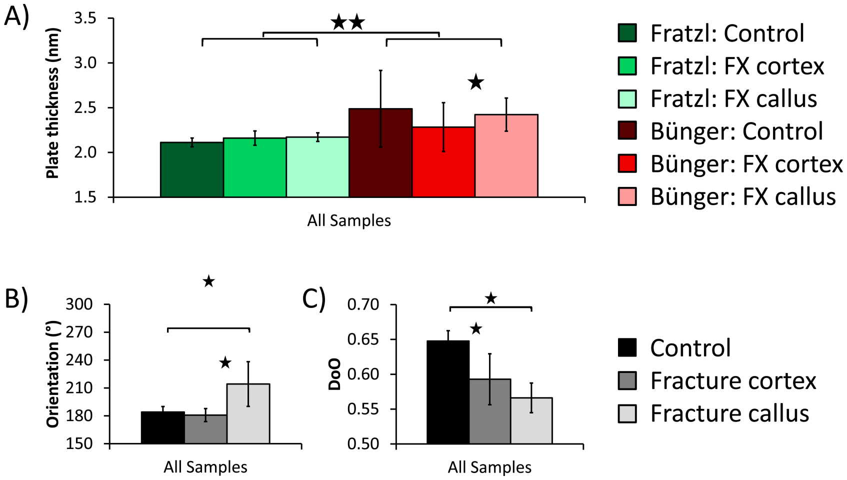

Figure 6.8: Results of mineral plate thickness determined using the methods proposed by Fratzl et al. *and Bünger* et al. *A), pre-dominant orientation B) and degree of orientation C) in control cortex, fracture cortex and fracture callus for all samples. Non-parametric Wilcoxon signed rank test ** $p < 0.01$, * $p < 0.05$.*

The pre-dominant orientation (Figure 6.8B) was significantly different in the callus tissue compared to the fracture and control cortices ($p < 0.05$ in both). DoO (Figure 6.8C) was significantly higher in the control cortex than in the fracture cortex and callus ($p < 0.05$ in both). The pre-dominant orientation of the mineral crystals was along the long axis of the bone in the cortices, whereas in the callus tissue the orientation was more random (Figure 6.8B). DoO was higher in the control cortices as compared to fracture cortices and calluses (Figure 6.8C).

Additionally, when the data from all treatment groups and locations were pooled, the mineral plate thickness determined using the method proposed by Fratzl *et al.* [64,65,67] from SAXS data correlated significantly with the crystallinity from FTIR ($r^2 = 0.489$, $p < 0.01$) (Figure 6.9). However, mineral plate thickness determined with the curve fitting method proposed by Bünger *et al.* [68] displayed no correlations with any of the compositional parameters determined from the IR spectra.

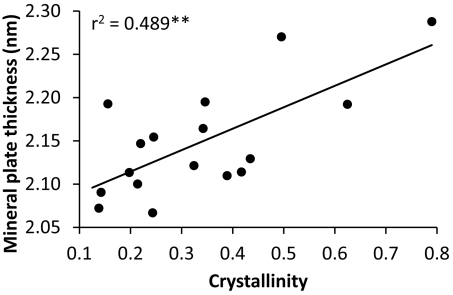

Figure 6.9: Linear correlation between the mineral plate thickness determined with the method proposed by Fratzl et al. *from SAXS and crystallinity from FTIR. Pearson's correlation* ** $p < 0.01$.

7 Discussion

7.1 BONE CHANGES WITH AGE

Studies **I-III** examined the compositional and/or structural changes in rabbit cortical bone (**I-II**) or human trabecular bone (**III**).

Composition

When new immature bone is formed, osteoblasts synthesize organic matrix which is mostly collagen [1, 7]. Thus, the collagen content increases rapidly during bone formation, especially during early skeletal growth in animals. This was observed in study **II**, as the collagen content was evaluated with BA. The amide I peak in the bone IR spectrum is attributable mainly to collagen. Although it is not a direct measure of the collagen content, it has been used to estimate collagen content in articular cartilage [43,142,166] and decalcified bone [111]. Optical retardation, calculated from PLM images, is an indicator of collagen content and anisotropy [43, 167]. Since collagen fibers run almost perfectly along the long axis of the cortical bone shaft, the anisotropy is low and thus the optical retardation may be an indication of collagen content. In study **II**, the amide I peak area (FTIR) and optical retardation (PLM) both yielded similar results as BA and the correlations between each parameter pair was significant. Thus, the findings support the concept that collagen content increases quickly during early maturation (from newborn until 1 month of aged rabbits) and continues to increase at a slower pace until skeletal maturity has been achieved, *i.e.* 6-9 months in rabbits [93, 152]. As the bone matures, it becomes spatially more homogenous. This is supported by the finding that the spatial heterogeneity of amide I (and amide II) decreased until the age of 3 months.

As the collagen content increases, the amount of collagen cross-linking also begins to rise. First, immature cross-links connect the collagen fibers and then with time, they are reduced to mature cross-links [77]. In study **II**, the mature HP cross-link content was evaluated biochemically. As expected, the HP content increased with maturation until skeletal maturity was reached. Paschalis *et al.* analyzed the IR spectra of peptides linked by Pyr (mature) and deH-DHLNL (immature) cross-links [21]. They found major peaks at ~ 1660 cm^{-1} for Pyr and at ~ 1690 cm^{-1} for deH-DHLNL, whereas no peak at ~ 1660 cm^{-1} was observed for deH-DHLNL. The ratio of these peaks has been utilized to describe the collagen maturity [21, 22, 28, 112]. A significant correlation was found between the mature cross-links determined from IR spectra and by BA. The results from studies **I** and **II** reveal that the collagen maturity in rabbits increased significantly until 3 months of age but thereafter remain stable until 18 months of age. This is consistent with the reported changes in bovine bone based on FTIR microspectroscopy [21] and BA [168].

When the collagen network is formed, mineralization begins when the HA crystals start to appear between the collagen fibers [1, 83]. The mineralization can be evaluated using IR or Raman spectra of bone [22,24,29,30,38,39,91,92,112,115,117,130–132,137,169,170]. The M/M ratio reflects the degree of mineralization and has been shown to correlate with ash weight in bone [17,116]. In agreement with earlier reports [17,21,24,37,38], the results in studies **I** and **III** indicate that the M/M ratio increases during maturation from very young to skeletally mature rabbits, but that it continues to increase also throughout the human adult life. The C_B/M ratio and the C/M ratio additionally reveal information about the carbonate content in bone. These parameters also increased significantly during maturation of rabbit bone and during the human adult life. These changes are consistent with earlier reports that described higher mineralization and carbonate content with increasing age in cortical [39] and trabecular bone [91]. Mineralization, collagen maturity and crystallinity are all properties that affect the mechanical properties of bone. As the mineralization increases, the bone becomes stiffer and thus more brittle, which partly can increase the fracture risk [31]. In addition, an increase in collagen maturity and crystallinity has been postulated to contribute to bone weakening and increased fracture risk [171].

With time, the HA crystals undergo changes as carbonate substitutes to the hydroxide (type-A substitution) or phosphate (type-B substitution) site of the HA crystal. It has been suggested that carbonate substitution occurs randomly over time and Raman spectroscopy studies have shown that carbonate substitution increases with increasing age [30,34,35]. In study **I**, the type-B carbonate substitution was found to increase in rabbit bone until 3 months of age but no clear changes where found in the C/P ratio (total carbonate substitution) in human bone during adult life (study **III**). The increase of the type-B carbonate substitution with age is consistent with earlier Raman studies [34, 35]. The C/P ratio has been speculated to relate to bone remodeling and turnover [92] and also the size of the mineral crystals, *i.e.* crystallinity, in bone tissue [90, 91]. In studies **I** and **III**, no significant changes were found in crystallinity with age in rabbits or humans. As the composition was assessed outwards from the osteon center [17, 24, 38], crystallinity was found to increase with tissue age, but no significant changes with animal age have been observed [39].

The precise lattice location of the acid phosphate substitution (APS) into the HA crystals has not been assessed [172] but it is known to associate with new mineral deposition [20, 22, 24]. Thus, greater acid phosphate substitution has been detected in newly formed bone as compared to older bone [110, 125, 126]. Hypothetically, a decrease in APS with maturation should be expected. The APS calculated from the data in studies **I** and **III** were consistent with this hypothesis. APS decreased in rabbit bone until skeletal maturity and a decline was also found in human calcaneus during adult life.

COLLAGEN STRUCTURE AND TRABECULAR BONE MICROARCHITECTURE

As the collagen matrix is initially formed, it is random in its orientation. When the bone becomes more mature, the collagen fibers orientate mainly in the main loading direction, *e.g.* longitudinally in the cortex of the long bones. In study **II**, this was observed using PLM, *i.e.* the orientation changed significantly (approached the orientation of the cortex) from newborn until 3 month old rabbits. With the material in study **II**, however, it is not possible to distinguish whether these changes are due to reorientation of existing collagen fibers or to the formation of new fibers, *i.e.* an increase in the collagen content. The spatial heterogeneity of the collagen fiber orientation and parallelism index, *i.e.* the anisotropy of the collagen fiber organization, decreased until 3 months of age. Hence, the bone collagen network becomes more regularly organized as maturation proceeds.

The age dependent changes in microarchitecture of trabecular bone in different anatomical locations have been studied in older men and women using μCT [51,60]. The BV/TV in greater trochanter has been found to increase in men with increasing age [60]. In study **III**, no significant correlations were detected between BV/TV and age. Instead, SMI and DA showed significant correlations with age as they increased and decreased, respectively. Previously, a higher BMD in the femoral neck compared to greater trochanter has been reported [60], which is consistent with the findings in study **III**. This is consistent also with the higher BV/TV and Tb.Th and lower SMI values found in study **III** in the femoral neck compared to greater trochanter. Recently, it was reported that Tb.Sp was lowest and Tb.N highest in calcaneus in men and women over 52 years of age [51]. The data in study **III** is generally in agreement with the reported data, except for DA which was found to be highest in the calcaneus in study **III**.

7.2 TRABECULAR BONE DIFFERS BETWEEN ANATOMICAL SITES

In study **III**, the microarchitecture and composition of femoral neck, greater trochanter and calcaneus were investigated.

MICROARCHITECTURE

In study **III**, significant differences in the microarchitecture of trabecular bone were demonstrated between the different anatomical locations. The greater trochanter showed the lowest BV/TV, Tb.Th, Tb.N and DA and the highest SMI. These are an indication of a more rod-like rather than plate-like structure. In a rod-like structure, the BV/TV is lower, the Tb.Th is reduced and the Tb.Sp is relatively high (more empty space between rods than plates). The DA is also lower, which is evidence of a more isotropic structure. The greater trochanter is exposed mainly to tensile stresses and presumably the structure presented above is better equipped to allow the tissue to resist these forces.

The femoral neck and calcaneus exhibit denser trabecular structures than the greater trochanter. In the femoral neck, the Tb.Th and BV/TV are high. These point to a well organized matrix capable of withstanding high compressive and shear stresses [161]. In calcaneus, both high compressive and tensile stresses are present [162]. The trabecular bone in calcaneus is dense (high BV/TV) with a high number (high Tb.N) of thin trabeculae (low Tb.Th) close to each other (low Tb.Sp). This could be interpreted to signify that there is a mixture of structures present in femoral neck and greater trochanter which is probably optimal for resisting the high impact compressive and tensile stresses.

COMPOSITION

The previous study by Donnelly *et al.* examined the compositional variation between subtrochanteric femur, the iliac crest and the greater trochanter [10]. The M/M ratio was found to be highest in cortical bone in subtrochanteric femur. However, no other differences were observed in the cortical and trabecular bone between those locations. When compared to the data in study **III**, it can be noted that the values of M/M ratio were similar ($\sim$ 4.2), whereas the previous study reported a slightly lower C/P ratio compared to the data in study **III**. Collagen maturity and crystallinity were lower in study **III** than in the work of Donnelly *et al.* [10]. These differences most likely originate from the differences in analysis methods (peak-fitting vs. intensity ratio [10]) for collagen maturity and crystallinity, and different instruments as well as sample gender [10]. Another recent study investigated the mineral content (calcium content) with scanning electron microscopy [173]. They found that the mineral content was higher in greater trochanter than in trochanter minor.

In study **III**, the M/M ratio was highest in greater trochanter. When analyzing the composition across the trabeculae, the C/M ratio and the C/P ratio were lowest in the middle of the trabeculae, *i.e.* the oldest bone in a trabecula, in the femoral neck. The M/M ratio and the C/M ratio reflect the degree of mineralization of bone, whereas the C/P ratio reflects the carbonate substitution and accumulation in bone, which is lower in bone with a high turnover rate [18, 92]. Crystallinity was lower in the calcaneus than in the femoral neck and greater trochanter. It has been observed that the crystallinity is lower near the sites of micro-damage [112]. In addition to the compressive and tensile stresses that the calcaneus experiences [162], this bone is also prone to impact loads [162], *e.g.* during running and jumping, which might evoke micro-damage in the trabecular bone and might partly explain the low crystallinity in the calcaneus.

INTER-RELATIONSHIP BETWEEN COMPOSITION AND MICROARCHITECTURE

In study **III**, significant correlations were found between compositional and structural parameters in the greater trochanter and calcaneus. This highlights the inter-relationship between the composition and microarchitecture. Both are affected by the loading environment and both are involved in controllingl the bone quality. However, a detailed evaluation of the contribution to each other would require compositional, structural and biomechanical data of the individual trabeculae, which was not possible in study **III**.

Linear regression models explaining the BMD in terms of microarchitecture and composition were studied. It was found that the BMD is affected more by the microarchitecture than by composition. BV/TV and Tb.N were the most important determinants of BMD, whereas no significant partial correlations were found in the compositional parameters in the models. Since BMD combines the structural and compositional variation into one single value, this is not unexpected. When the bone microarchitecture was dense, it reflected in a higher BMD value in the ROI. Thus, most probably the BMD is not sensitive enough to detect the more subtle changes in the mineral content of individual trabeculae.

7.3 FRACTURE CALLUS TISSUE

In study **IV**, it was demonstrated that FTIR and SAXS combined can be used to identify the differences in composition and mineral structure between the newly formed callus tissue and cortical bone tissue. Due to the low number of samples, the emphasis was on the comparison between the types of tissues, independent of the treatment. Additionally, the mineral plate thickness results obtained from the method proposed by Fratzl *et al.* [64, 65, 67] and Bünger *et al.* [68] were compared.

Lower degree of mineralization, collagen maturity and degree of orientation of the mineral crystals and higher APS are indicators of new, immature and less organized bone. As expected, this was found in study **IV** when newly formed callus tissue was compared with the cortices. In addition, the larger spread of orientation angles in the callus tissue reflects the disordered woven nature of the forming bone. This is as expected, since the orientation of the collagen fibers and mineral crystals in cortical bone are oriented primarily in the direction of the long axis of the bone [1, 2], *i.e.* the main loading direction. In the NaCl group, the calluses were smaller *e.g.* when compared to BMP-treated calluses. This seems to be reflected in the orientation parameters, where the NaCl treated samples displayed a more similar orientation to the cortical bone, compared to the large calluses in BMP-treated bones.

In the NaCl group, no union was achieved despite some sparse bone formation in the gap area. In contrast, all samples in the BMP-7 + ZO group were judged to be completely healed. These findings are consistent with previous studies using the same animal model with larger number of animals per group [153, 154].

COMPOSITION

The compositional (FTIR) results in study **IV** are mainly consistent with earlier reports where the composition of callus tissue and cortex has been evaluated [113, 114]. The M/M ratio was higher in the cortex compared to callus tissue [113,114], the collagen maturity was also higher in the cortex than in the callus tissue [113]. Crystallinity has been found to be similar [114] or slightly reduced [113] in fracture callus. In contrast to those findings, the results in study **IV** indicated a higher crystallinity in the callus tissue and fracture cortex compared to control cortex, but no significant differences were found between the callus tissue and fracture cortex. APS is associated with new mineral deposition [20, 26, 174] and a high APS value has been shown to indicate areas of new bone formation [125,126]. In study **IV**, a higher APS was observed in the callus tissue than in the cortices in line with the previous studies.

MINERAL STRUCTURE

Fracture callus tissue has received only minor attention in the SAXS literature [150, 151]. In these studies, the mineral plate thickness has been determined using the method proposed by Fratzl *et al.* [64,65,67]. In sheep, mineral plate thickness has been found to be lower in the callus tissue than in the fracture cortex during fracture healing [151]. The difference diminished 9 weeks after the fracture. The healing time of 6 weeks in a rat model, used in study **IV**, is comparable to a 9 week healing time in the sheep model, and thus these present results are consistent with the cited study. However, mineral plate thickness evaluated using the curve fitting method tended to be higher in control cortex compared to the fracture cortex and callus. Hypothetically, with a higher number of samples, the curve fitting method would have revealed a significantly higher mineral plate thickness in control cortex than in fracture cortex and callus even at this stage of fracture healing, although this was not observed with the method proposed by Fratzl *et al.* [64,65,67]. This would be expected since the turnover is higher at the fracture site due to remodeling of the woven bone compared to the intact bone.

7.4 VALIDATION

7.4.1 Compositional parameters

IR and Raman microspectroscopic techniques provide powerful tools with which to investigate the composition of the organic and inorganic phases in bone. Since the peaks in IR and Raman spectra are not unambiguous and are usually sum peaks of multiple molecular bond vibrations, the validity of the used peaks is critical. Today most of the parameters are validated and widely accepted to describe the composition of bone. In IR and Raman bone spectra, the analyzed peaks are based on various validations as the bone spectra have been compared to those of pure or synthetic compounds [20,21,23,89,110].

MINERALIZATION

M/M ratio, probably the most important and widely used compositional parameter, is an indicator of mineralization of bone. It has been shown to correlate with ash weight of bone [17,116]. The C/M ratio provides similar information as M/M ratio, with the difference that in M/M ratio the phosphate content is evaluated, whereas in the C/M ratio it is the carbonate content that is estimated. Both yield information about the mineral content in the bone and are reliable indicators of the mineralization, especially after the collagen network has formed, *i.e.* when the collagen content remains relatively stable.

CARBONATE SUBSTITUTION

C/P ratio is an indicator of carbonate substitution into the HA crystal. The carbonate substitution can occur in the hydroxide (type-A) or phosphate (type-B) site of the crystal. Usually from IR spectra, the total C/P ratio (type-A + type-B + labile) is determined because the carbonate peaks are close to each other, but it is possible to evaluate also type-A and type-B carbonate substitution through peak-fitting [24]. From Raman spectra, commonly only the type-B carbonate substitution is determined, although also type-A carbonate can be measured through curve fitting techniques.

COLLAGEN MATURITY

XLR, the ratio of mature and immature cross-links, has been increasingly used to describe the collagen maturity of bone in spectroscopic studies [21,22,28,39,81,92,109,113,115,119,120,171]. It has been proposed by Paschalis *et al.* to describe the ratio of Pyr (mature) and deH-DHLNL (immature) cross-links [21]. It is calculated as the ratio of areas (or intensities) of two sub-peaks at $\sim$ 1660 cm^{-1} and $\sim$ 1690 cm^{-1}, if peak-fitting is used, or as the ratio of the intensities at 1660 cm^{-1} and 1690 cm^{-1} in the actual bone spectrum.

Although the sub-peak areas (or spectrum intensities) are not actual indicators of the deH-DHLNL or Pyr cross-links, the ratio has been commonly accepted as the indicator of the mature/immature cross-link ratio or collagen maturity [21, 22, 28, 39, 81, 92, 109, 113, 115, 119, 120, 171]. Generally, it has been found to increase during maturation and with aging and it appears to be a valid indicator of the developmental stage of the collagen network. The peak-fitting method requires extensive calculation and is relatively time consuming compared to the time and effort needed to calculate the ratio directly from the spectrum. In study **I**, interestingly, the XLR results obtained with these two methods correlated significantly ($r^2 = 0.880$, $p < 0.01$).

The collagen maturity parameter determined as discussed above, has also been subjected to criticism. A recent study indicated that the ratio of $\sim$ 1660 cm^{-1} and $\sim$ 1690 cm^{-1} was not related to the ratio of Pyr and deH-DHLNL cross-links [175]. They stated that the changes in this parameter might be due to modifications in the collagen secondary structure which is related to the age-dependent mineralization process. However, according to their conclusion the ratio may still be attributable to age-related changes in the collagen secondary structure. Therefore, the assignation of the term *collagen maturity* to the ratio may still be valid.

CRYSTALLINITY

Crystallinity has been shown to correlate with the c-axis length of the HA crystal, as determined with XRD, with increasing tissue age [24, 38, 169]. In study **I**, a similar trend was seen since the crystallinity increased with age as determined from Raman spectra. However, this age dependent increase of crystallinity with animal age was not observed in studies **I** or **III** or in the literature elsewhere when FTIR has been utilized [39].

Acid phosphate substitution

APS has been evaluated using various intensities of the IR spectrum of bone [22, 117, 174, 176]. It is known to be higher in newly formed bone [110,125,126] which makes it a good indicator of bone formation. The recent study of Spevak *et al.* further validated the parameter; these investigators concluded that it was calid to use the ratio of intensities at 1127 cm^{-1} and 1096 cm^{-1} as an indicator of acid phosphate content or acid phosphate substitution [26].

FTIR vs. Raman

The findings from IR and Raman based studies of bone are often compared and believed to be interchangeable [91, 112, 130, 131, 170]. However, many spectral features of bone, especially differences between IR and Raman spectra, are still poorly understood. A few studies have compared the similar IR and Raman compositional parameters [39,177–180]. However, usually these have been conducted on selected biochemical molecules rather than on biological tissues with their more complex molecular structure. Gourion-Arsiquaud *et al.* [39] compared the IR and Raman compositional parameters in baboon bone in terms of tissue aging but they did not compare the parameters with different ages of animals. In general, they observed significant correlations between IR and Raman spectroscopic parameters. In study **I**, where IR and Raman compositional parameters were compared with animal age, the results were mostly consistent with the findings by Gourion-Arsiquaud *et al.* However, caution is required when performing a comparison between compositional parameters determined from IR and Raman spectra, especially when related to carbonate (total vs. type-B).

Clustering

The differences in bone, or other tissues during aging or diseases can be evaluated by calculating the compositional parameters described as above. Another approach is clustering; in clustering, the whole spectrum, or parts of it, is taken into account and the spectral features, like shape, are used to classify the spectra in different categories. In this way, no compositional parameters are directly calculated and a larger amount of information is utilized in the classification. For example, clustering has been used in bone analyses where newborn, immature and mature bone were successfully classified into the correct categories [109, 111]. Furthermore, clustering would be very useful when trying to distinguish cancer tissue and normal tissue in sections where traditional staining will not work.

7.4.2 Structural parameters

The microstructural parameters of trabecular bone, as calculated from the μCT reconstructed images, are well validated. The structural parameters can be determined reliably as long as the resolution of the μCT is good enough to separate the individual trabeculae. Previous studies have shown that the structural parameters are greatly dependent on the image resolution [59, 181–183]. The μCT parameters are average indices describing the structure in the actual geometry. For example, BV/TV is calculated as the fraction of bone in the measurement area and Tb.Th [μm] and Tb.N [μm^{-1}] are the average thickness and number of trabeculae in the measurement area. SMI has been assigned to indicate the plate-like or rod-like character of the trabeculae The ideal plate-like structure has a SMI of 0 and the ideal cylindrical rod-like structure has a SMI of 3 [63]. In trabecular bone, usually both are present and the average SMI is between 0 and 3. DA can be defined using the mean intercept length (MIL) method [55, 184, 185]. The MIL is dependent solely on the interface between the bone and marrow, which might mean that clearly anisotropic structures may appear isotropic when examined with the MIL method [55, 186].

7.4.3 Mineral structure parameters

In study **IV**, the mineral plate thickness values were significantly higher (12 %, $p < 0.01$) when analyzed with the curve fitting methods in comparison to the values calculated with the method proposed by Fratzl *et al.* The assumption of the mineral phase fraction of 50 % in the method proposed by Fratzl *et al.* might not be valid when evaluating the mineral plate thickness of newly formed bone or bone under high turnover. In equation 3.23, it can be seen that the calculated mineral plate thickness increases with increasing mineral plate fraction ϕ. Thus, it may underestimate the mineral plate thickness (if the real $\phi > 0.5$) in cortex bone, whereas in newly formed bone it might provide an overestimation since presumably $\phi < 0.5$ in newly formed bone. In one SAXS study, the mineral fraction was found to vary within dentin [187] and similar variation could be expected also in bone. Thus, a curve fitting approach in the evaluation of the mineral plate thickness, especially in newly formed bone and bone under high turnover, is recommended.

7.5 STRENGTHS AND LIMITATIONS

7.5.1 Compositional analyses of bone

Biochemical analysis has been the golden standard when assessing the organic composition of tissues. However, it is not possible to investigate the spatial inorganic composition of bone using BA. In the evaluation of the mineral content in bone, the sample can be burned and the ash weight can provide an approximation of the mineral content in the bone. In both methods, the other phase has eventually been removed and thus both organic and inorganic composition cannot be studied in the same sample. Additionally, often in BA (HPCL), small samples are used that may introduce uncertainty, *e.g.* due to weighing, and high variability (CV%) in the results, as seen in study **II**.

With FTIR and Raman microspectroscopic techniques, both organic and inorganic composition can be evaluated from the same sample without destroying either phase. However, the measured peaks do not arise directly from the components that they have been assigned to represent. For example, the collagen content is evaluated from the peak found at ~ 1650 cm^{-1} which mainly arises from the molecular bonds in the amide I chain. However, other organic proteins in bone also contain amide I bonds. Furthermore, since collagen has a lot of amide I, and is the major contributor to the organic phase in bone, the peak can be used as an indicator of the amount of collagen. Another problem with the Raman and FTIR spectra is the overlapping of the small peaks, *i.e.* basically all visible peaks in the bone spectrum are sum of peaks with energies close to each other. Fortunately, peaks close to each other arise from similar molecules and the analyzed sum peak represents the composition of the molecules of interest relatively well. If a more detailed analyses of the fine structure of the spectrum is needed, peak fitting techniques, for example, can be used to break up the measured sum spectrum into the different components, *i.e.* sub peaks.

In FTIR and Raman microspectroscopy the measurement areas are relatively small. For example, when studying the composition of trabecular bone in study **III**, three representative areas of 0.053 ± 0.013 mm^2 of trabeculae from one bone section of each sample were measured. In study **I**, five Raman point measurements of cortical bone were made around the cortex. Thus, since relatively small measurement areas compared to the size of the bone are used in FTIR and Raman studies of bone, the results must always be interpreted with caution. Indeed, they may not be fully representative.

The sample preparation for FTIR and Raman microspectroscopy is different. In FTIR, bone sections of 1-5 μm are used. The absorption of the IR light is directly proportional to the sample thickness. As the section thickness can vary within and between the sections, ratios of peaks are usually used to describe the composition. Naturally, the thicker the sample, the smaller the relative variation in the sample thickness. Thus, in study **II** where the section thickness was 5 μm, the amide I and amide II peak areas were directly used as an indicator of the collagen content. In Raman, the sample preparation is more straightforward, since the measurements can be done from the surface of the sample. However, in order to optimize the signal, the surface is usually polished and care needs to be taken to carefully clean the polished bone and embedding medium dust which could potentially interfere the measurements.

7.5.2 Structural analyses of bone

Polarized light microscopy can provide information about the collagen fiber content, orientation and heterogeneity. It is based on visible light images which makes it an effective tool with which to evaluate large areas of multiple samples. In bone, relatively large samples, *e.g.* in study **II** half of the length of a fully grown rabbit femurs, could be easily imaged at once. However, since PLM is limited by the light wavelength, it is impossible to study individual collagen fibers. Evaluation of the collagen content, orientation and heterogeneity is based on collagen bundles. Another limitation is that in order for light to penetrate the bone samples, they have to be decalcified. Thus, the bone mineral phase cannot be studied.

μCT has been used widely to evaluate the trabecular and cortical bone microarchitecture. Since the indices are average physical measures of the bone, they are reliable. However, as the indices are averaged in the whole ROI, possible variations within the ROI may not be detected. For example, when approaching the cortex from the center of the proximal femur, the trabecular structure changes significantly and care should be taken to exclude areas close to the cortex from the ROI. Another limitation might be the resolution. One has to concider carefully what level of resolution is needed to detect the smallest details in trabecular bone, for example, to obtain reliable information about the structure [92].

7.5.3 Analyses of bone mineral structure

When combined with a moving x-y stage, SAXS provides a powerful tool to determine the spatial information about mineral plate thickness and orientation of the crystals in bone without destroying the sample. Powder XRD provides similar information about the average size of the mineral crystals, but the orientation information is lost since the sample is powderized. In XRD, the actual length and width of the crystal can be determined easily (from the broadening of the peak), whereas in SAXS more complicated approaches are needed (discussed in section 7.4.3). However, in addition to the crystal size, the XRD peak widths are also sensitive to disorders and strains, which possibly impairs the accuracy of the size estimation. In SAXS, the resolution is also important, *i.e.* the size of the focus of the beam and the step size of the stage. When studying small objects, smaller focus and step size are needed in order to obtain spatial information. A larger focus and step size would presumably provide similar bulk information but miss the detailed structure. Additionally, the data is also averaged over the sample thickness. The optimal thickness of SAXS samples ranges from below 100 μm upto 600 μm [65]. In study **IV**, the sample thickness was 300 μm. Although being somewhat thicker than the beamsize used (200 μm), it is still within these limits.

8 Summary and conclusions

In this thesis, characteristic changes in composition and microarchitecture of bone during growth, maturation and aging were evaluated using a wide range of techniques and analysis methods. In addition, the composition and mineral structure of newly formed bone in fracture callus were studied. All these results contribute to the conception of bone quality. The validity of the parameters and the output of each used technique were critically discussed and an extensive comparison was performed between the similar parameters obtained from different techniques.

The main conclusions from this thesis may be summarized as follows:

- Spectroscopic techniques were able to describe the rapid compositional changes during early maturation of bone.
- Bone composition continues to change with aging, although at a slower pace, even after skeletal maturity has been reached.
- The composition and microarchitecture of trabecular bone varies between anatomical locations. This may be linked to differences in the loading environments.
- The composition and mineral structure of newly formed callus tissue during long bone healing differs from cortical bone tissue.
- FTIR and SAXS represent as techniques sensitive enough to assess the composition and mineral structure of newly formed callus tissue.
- Caution is required when one attempts to compare similar parameters of bone composition obtained with different techniques.

Bibliography

[1] J. A. Buckwalter, M. J. Glimcher, R. R. Cooper, and R. Recker, "Bone biology. I: Structure, blood supply, cells, matrix, and mineralization," *Instructional course lectures* **45,** 371–386 (1996).

[2] J. A. Buckwalter, M. J. Glimcher, R. R. Cooper, and R. Recker, "Bone biology. II: Formation, form, modeling, remodeling, and regulation of cell function," *Instructional course lectures* **45,** 387–399 (1996).

[3] J. J. Wolff, "Das Gesetz der Transformation der Knochen," *Hirschwald, Berlin, Germany.* (1892).

[4] C. H. Turner, "Three rules for bone adaptation to mechanical stimuli," *Bone* **23,** 399–407 (1998).

[5] B. Busa, L. M. Miller, C. T. Rubin, Y. X. Qin, and S. Judex, "Rapid establishment of chemical and mechanical properties during lamellar bone formation," *Calcified tissue international* **77,** 386–394 (2005).

[6] M. Nordin and V. H. Frankel, *Basic Biomechanics of the Musculoskeletal System*, 3 ed. (Lippincott Williams & Wilkins, Baltimore, Maryland, USA, 2001).

[7] U.S. Department of Health and Human Services, "Bone Health and Osteoporosis: A Report of the Surgeon General," *Rockville, MD: U.S. Department of Health and Human Services, Office of the Surgeon General,* (2004).

[8] M. C. van der Meulen, K. J. Jepsen, and B. Mikic, "Understanding bone strength: size isn't everything," *Bone* **29,** 101–104 (2001).

[9] J. D. Currey, "The many adaptations of bone," *Journal of Biomechanics* **36,** 1487–1495 (2003).

[10] E. Donnelly, D. S. Meredith, J. T. Nguyen, and A. L. Boskey, "Bone tissue composition varies across anatomic sites in the proximal femur and the iliac crest," *Journal of orthopaedic research* **30,** 700–706 (2012).

[11] T. A. Einhorn, "The science of fracture healing," *Journal of orthopaedic trauma* **19,** S4–6 (2005).

[12] A. Schindeler, M. M. McDonald, P. Bokko, and D. G. Little, "Bone remodeling during fracture repair: The cellular picture," *Seminars in cell & developmental biology* **19,** 459–466 (2008).

[13] Y. Doi, M. Miyazaki, T. Yoshiiwa, K. Hara, M. Kataoka, and H. Tsumura, "Manipulation of the anabolic and catabolic responses with BMP-2 and zoledronic acid in a rat femoral fracture model," *Bone* **49,** 777–782 (2011).

[14] D. G. Little, M. McDonald, R. Bransford, C. B. Godfrey, and N. Amanat, "Manipulation of the anabolic and catabolic responses with OP-1 and zoledronic acid in a rat critical defect model," *Journal of bone and mineral research* **20,** 2044–2052 (2005).

[15] A. K. Harding, P. Aspenberg, M. Kataoka, D. Bylski, and M. Tägil, "Manipulating the anabolic and catabolic response in bone graft remodeling: synergism by a combination of local BMP-7 and a single systemic dosis of zoledronate," *Journal of orthopaedic research* **26,** 1245–1249 (2008).

[16] M. J. Rogers, J. C. Crockett, F. P. Coxon, and J. Mönkkönen, "Biochemical and molecular mechanisms of action of bisphosphonates," *Bone* **49,** 34–41 (2011).

[17] A. Boskey and N. Pleshko Camacho, "FT-IR imaging of native and tissue-engineered bone and cartilage," *Biomaterials* **28,** 2465–2478 (2007).

[18] R. Y. Huang, L. M. Miller, C. S. Carlson, and M. R. Chance, "Characterization of bone mineral composition in the proximal tibia of cynomolgus monkeys: effect of ovariectomy and nandrolone decanoate treatment," *Bone* **30,** 492–497 (2002).

[19] L. M. Miller, W. Little, A. Schirmer, F. Sheik, B. Busa, and S. Judex, "Accretion of bone quantity and quality in the developing mouse skeleton," *Journal of bone and mineral research* **22,** 1037–1045 (2007).

[20] C. Rey, M. Shimizu, B. Collins, and M. J. Glimcher, "Resolution-enhanced Fourier transform infrared spectroscopy study of the environment of phosphate ion in the early deposits of a solid phase of calcium phosphate in bone and enamel and their evolution with age: 2. Investigations in the ν_3PO_4 domain," *Calcified tissue international* **49,** 383–388 (1991).

[21] E. P. Paschalis, K. Verdelis, S. B. Doty, A. L. Boskey, R. Mendelsohn, and M. Yamauchi, "Spectroscopic characterization of collagen cross-links in bone," *Journal of bone and mineral research* **16,** 1821–1828 (2001).

[22] H. W. Courtland, P. Nasser, A. B. Goldstone, L. Spevak, A. L. Boskey, and K. J. Jepsen, "Fourier transform infrared imaging microspectroscopy and tissue-level mechanical testing reveal intraspecies variation in mouse bone mineral and matrix composition," *Calcified tissue international* **83,** 342–353 (2008).

[23] N. Pleshko, A. Boskey, and R. Mendelsohn, "Novel infrared spectroscopic method for the determination of crystallinity of hydroxyapatite minerals," *Biophysical journal* **60,** 786–793 (1991).

[24] E. P. Paschalis, E. DiCarlo, F. Betts, P. Sherman, R. Mendelsohn, and A. L. Boskey, "FTIR microspectroscopic analysis of human osteonal bone," *Calcified tissue international* **59,** 480–487 (1996).

[25] S. J. Gadaleta, E. P. Paschalis, F. Betts, R. Mendelsohn, and A. L. Boskey, "Fourier transform infrared spectroscopy of the solution-mediated conversion of amorphous calcium phosphate to hydroxyapatite: new correlations between X-ray diffraction and infrared data," *Calcified tissue international* **58,** 9–16 (1996).

[26] L. Spevak, C. R. Flach, T. Hunter, R. Mendelsohn, and A. Boskey, "Fourier Transform Infrared Spectroscopic Imaging Parameters Describing Acid Phosphate Substitution in Biologic Hydroxyapatite," *Calcified tissue international* (2013).

[27] C. Marcott, R. C. Reeder, E. P. Paschalis, D. N. Tatakis, A. L. Boskey, and R. Mendelsohn, "Infrared microspectroscopic imaging of biomineralized tissues using a mercury-cadmium-telluride focal-plane array detector," *Cellular and molecular biology (Noisy-le-Grand, France)* **44,** 109–115 (1998).

[28] E. Durchschlag, E. P. Paschalis, R. Zoehrer, P. Roschger, P. Fratzl, R. Recker, R. Phipps, and K. Klaushofer, "Bone material properties in trabecular bone from human iliac crest biopsies after 3- and 5-year treatment with risedronate," *Journal of bone and mineral research* **21,** 1581–1590 (2006).

[29] J. W. Ager, R. K. Nalla, K. L. Breeden, and R. O. Ritchie, "Deep-ultraviolet Raman spectroscopy study of the effect of aging on human cortical bone," *Journal of Biomedical Optics* **10,** 034012 (2005).

[30] O. Akkus, F. Adar, and M. B. Schaffler, "Age-related changes in physicochemical properties of mineral crystals are related to impaired mechanical function of cortical bone," *Bone* **34,** 443–453 (2004).

[31] E. Donnelly, A. L. Boskey, S. P. Baker, and M. C. van der Meulen, "Effects of tissue age on bone tissue material composition and nanomechanical properties in the rat cortex," *Journal of biomedical materials research.Part A* **92,** 1048–1056 (2010).

[32] J. J. Freeman, B. Wopenka, M. J. Silva, and J. D. Pasteris, "Raman spectroscopic detection of changes in bioapatite in mouse femora as a function of age and in vitro fluoride treatment," *Calcified tissue international* **68,** 156–162 (2001).

[33] S. Gamsjaeger, A. Masic, P. Roschger, M. Kazanci, J. W. Dunlop, K. Klaushofer, E. P. Paschalis, and P. Fratzl, "Cortical bone composition and orientation as a function of animal and tissue age in mice by Raman spectroscopy," *Bone* **47,** 392–399 (2010).

[34] C. P. Tarnowski, M. A. I. Jr, and M. D. Morris, "Mineralization of developing mouse calvaria as revealed by Raman microspectroscopy," *Journal of bone and mineral research* **17,** 1118–1126 (2002).

[35] J. S. Yerramshetty, C. Lind, and O. Akkus, "The compositional and physicochemical homogeneity of male femoral cortex increases after the sixth decade," *Bone* **39,** 1236–1243 (2006).

[36] J. Burket, S. Gourion-Arsiquaud, L. M. Havill, S. P. Baker, A. L. Boskey, and M. C. van der Meulen, "Microstructure and nanomechanical properties in osteons relate to tissue and animal age," *Journal of Biomechanics* **44,** 277–284 (2011).

[37] R. Mendelsohn, E. P. Paschalis, and A. L. Boskey, "Infrared spectroscopy, microscopy, and microscopic imaging of mineralizing tissues: spectra-structure correlations from human iliac crest biopsies," *Journal of Biomedical Optics* **4,** 14–21 (1999).

[38] E. P. Paschalis, F. Betts, E. DiCarlo, R. Mendelsohn, and A. L. Boskey, "FTIR microspectroscopic analysis of normal human cortical and trabecular bone," *Calcified tissue international* **61,** 480–486 (1997).

[39] S. Gourion-Arsiquaud, J. C. Burket, L. M. Havill, E. DiCarlo, S. B. Doty, R. Mendelsohn, M. C. van der Meulen, and A. L. Boskey, "Spatial variation in osteonal bone properties relative to tissue and animal age," *Journal of bone and mineral research* **24,** 1271–1281 (2009).

[40] J. Rieppo, J. Töyräs, M. T. Nieminen, V. Kovanen, M. M. Hyttinen, R. K. Korhonen, J. S. Jurvelin, and H. J. Helminen, "Structure-function relationships in enzymatically modified articular cartilage," *Cells, tissues, organs* **175,** 121–132 (2003).

[41] X. Bi, G. Li, S. B. Doty, and N. P. Camacho, "A novel method for determination of collagen orientation in cartilage by Fourier transform infrared imaging spectroscopy (FT-IRIS)," *Osteoarthritis and cartilage* **13,** 1050–1058 (2005).

[42] Y. Xia, J. B. Moody, H. Alhadlaq, and J. Hu, "Imaging the physical and morphological properties of a multi-zone young articular cartilage at microscopic resolution," *Journal of magnetic resonance imaging* **17,** 365–374 (2003).

[43] J. Rieppo, J. Hallikainen, J. S. Jurvelin, I. Kiviranta, H. J. Helminen, and M. M. Hyttinen, "Practical considerations in the use of polarized light microscopy in the analysis of the collagen network in articular cartilage," *Microscopy research and technique* **71,** 279–287 (2008).

[44] J. P. Arokoski, M. M. Hyttinen, T. Lapveteläinen, P. Takacs, B. Kosztaczky, L. Modis, V. Kovanen, and H. Helminen, "Decreased birefringence of the superficial zone collagen network in the canine knee (stifle) articular cartilage after long distance running training, detected by quantitative polarised light microscopy," *Annals of the Rheumatic Diseases* **55,** 253–264 (1996).

[45] D. Mittelstaedt, Y. Xia, A. Shmelyov, N. Casciani, and A. Bidthanapally, "Quantitative determination of morphological and territorial structures of articular cartilage from both perpendicular and parallel sections by polarized light microscopy," *Connective tissue research* **52,** 512–522 (2011).

[46] J. G. Ramasamy and O. Akkus, "Local variations in the micromechanical properties of mouse femur: the involvement of collagen fiber orientation and mineralization," *Journal of Biomechanics* **40,** 910–918 (2007).

[47] J. T. Holopainen, P. A. Brama, E. Halmesmäki, T. Harjula, J. Tuukkanen, P. R. van Weeren, H. J. Helminen, and M. M. Hyttinen, "Changes in subchondral bone mineral density and collagen matrix organization in growing horses," *Bone* **43,** 1108–1114 (2008).

[48] M. Martiniakova, I. B. Ova, R. Omelka, B. Grosskopf, R. Stawarz, and R. Toman, "Structural changes in femoral bone tissue of rats after subchronic peroral exposure to selenium," *Acta Veterinaria Scandinavica* **55,** 8 (2013).

[49] X. Rodriguez, X. Vela, J. L. Calvo-Guirado, J. Nart, and C. F. Stappert, "Effect of platform switching on collagen fiber orientation and bone resorption around dental implants: a preliminary histologic animal study," *The International journal of oral & maxillofacial implants* **27,** 1116–1122 (2012).

[50] J. K. Kalmey and C. O. Lovejoy, "Collagen fiber orientation in the femoral necks of apes and humans: do their histological structures reflect differences in locomotor loading?," *Bone* **31,** 327–332 (2002).

[51] F. Eckstein, M. Matsuura, V. Kuhn, M. Priemel, R. Müller, T. M. Link, and E. M. Lochmüller, "Sex differences of human trabecular bone microstructure in aging are site-dependent," *Journal of bone and mineral research* **22,** 817–824 (2007).

[52] G. Diederichs, T. M. Link, M. Kentenich, K. Schwieger, M. B. Huber, A. J. Burghardt, S. Majumdar, P. Rogalla, and A. S. Issever, "Assessment of trabecular bone structure of the calcaneus using multi-detector CT: correlation with microCT and biomechanical testing," *Bone* **44,** 976–983 (2009).

[53] C. Chappard, A. Marchadier, and C. L. Benhamou, "Side-to-side and within-side variability of 3D bone microarchitecture by conventional micro-computed tomography of paired iliac crest biopsies," *Bone* **43,** 203–208 (2008).

[54] K. Verdelis, L. Lukashova, E. Atti, P. Mayer-Kuckuk, M. G. Peterson, S. Tetradis, A. L. Boskey, and M. C. van der Meulen, "MicroCT morphometry analysis of mouse cancellous bone: intra- and inter-system reproducibility," *Bone* **49,** 580–587 (2011).

[55] A. Odgaard, "Three-dimensional methods for quantification of cancellous bone architecture," *Bone* **20,** 315–328 (1997).

[56] E. Nägele, V. Kuhn, H. Vogt, T. M. Link, R. Müller, E. M. Lochmüller, and F. Eckstein, "Technical considerations for microstructural analysis of human trabecular bone from specimens excised from various skeletal sites," *Calcified tissue international* **75,** 15–22 (2004).

[57] T. Hildebrand, A. Laib, R. Müller, J. Dequeker, and P. Ruegsegger, "Direct three-dimensional morphometric analysis of human cancellous bone: microstructural data from spine, femur, iliac crest, and calcaneus," *Journal of bone and mineral research* **14,** 1167–1174 (1999).

[58] H. Isaksson, V. Tolvanen, M. A. Finnilä, J. Iivarinen, A. Turunen, T. S. Silvast, J. Tuukkanen, K. Seppänen, J. P. Arokoski, P. A. Brama, J. S. Jurvelin, and H. J. Helminen, "Long-term voluntary exercise of male mice induces more beneficial effects on cancellous and cortical bone than on the collagenous matrix," *Experimental gerontology* **44,** 708–717 (2009).

[59] H. Isaksson, J. Töyräs, M. Hakulinen, A. S. Aula, I. Tamminen, P. Julkunen, H. Kröger, and J. S. Jurvelin, "Structural parameters of normal and osteoporotic human trabecular bone are affected differently by microCT image resolution," *Osteoporosis international* **22,** 167–177 (2011).

[60] E. M. Lochmüller, M. Matsuura, J. Bauer, W. Hitzl, T. M. Link, R. Müller, and F. Eckstein, "Site-specific deterioration of trabecular bone architecture in men and women with advancing age," *Journal of bone and mineral research* **23,** 1964–1973 (2008).

[61] M. Amling, S. Herden, M. Posl, M. Hahn, H. Ritzel, and G. Delling, "Heterogeneity of the skeleton: comparison of the trabecular microarchitecture of the spine, the iliac crest, the femur, and the calcaneus," *Journal of bone and mineral research* **11,** 36–45 (1996).

[62] H. Chen, X. Zhou, S. Shoumura, S. Emura, and Y. Bunai, "Age- and gender-dependent changes in three-dimensional microstructure of cortical and trabecular bone at the human femoral neck," *Osteoporosis international* **21,** 627–636 (2010).

[63] T. Hildebrand and P. Ruegsegger, "Quantification of Bone Microarchitecture with the Structure Model Index," *Computer methods in biomechanics and biomedical engineering* **1,** 15–23 (1997).

[64] P. Fratzl, "Statistical Model of the Habit and Arrangement of Mineral Crystals in the Collagen of Bone," *Journal of Statistical Physics* **77,** 125–143 (1994).

[65] P. Fratzl, S. Schreiber, and K. Klaushofer, "Bone mineralization as studied by small-angle x-ray scattering," *Connective tissue research* **34,** 247–254 (1996).

[66] P. Fratzl, N. Fratzl-Zelman, K. Klaushofer, G. Vogl, and K. Koller, "Nucleation and growth of mineral crystals in bone studied by small-angle X-ray scattering," *Calcified tissue international* **48,** 407–413 (1991).

[67] S. Rinnerthaler, P. Roschger, H. F. Jakob, A. Nader, K. Klaushofer, and P. Fratzl, "Scanning small angle X-ray scattering analysis of human bone sections," *Calcified tissue international* **64,** 422–429 (1999).

[68] M. H. Bünger, H. Oxlund, T. K. Hansen, S. Sorensen, B. M. Bibby, J. S. Thomsen, B. L. Langdahl, F. Besenbacher, J. S. Pedersen, and H. Birkedal, "Strontium and bone nanostructure in normal and ovariectomized rats investigated by scanning small-angle X-ray scattering," *Calcified tissue international* **86,** 294–306 (2010).

[69] J. M. Burnell, E. J. Teubner, and A. G. Miller, "Normal maturational changes in bone matrix, mineral, and crystal size in the rat," *Calcified tissue international* **31,** 13–19 (1980).

[70] L. T. Kuhn, M. D. Grynpas, C. C. Rey, Y. Wu, J. L. Ackerman, and M. J. Glimcher, "A comparison of the physical and chemical differences between cancellous and cortical bovine bone mineral at two ages," *Calcified tissue international* **83,** 146–154 (2008).

[71] H. P. Klug and L. E. Alexander, *X-ray Diffraction Procedures for Polycrystalline and Amorphous Materials*, 2 ed. (John Wiley & Sons, New York, NY, 1974).

[72] R. R. Cooper, J. W. Milgram, and R. A. Robinson, "Morphology of the osteon. An electron microscopic study," *The Journal of bone and joint surgery.American volume* **48,** 1239–1271 (1966).

[73] P. J. Kelly, "Anatomy, physiology, and pathology of the blood supply of bones," *J.Bone Joint Surg.Am.* **50,** 766–783 (1968).

[74] F. L. Bach-Gansmo, S. C. Irvine, A. Bruel, J. S. Thomsen, and H. Birkedal, "Calcified cartilage islands in rat cortical bone," *Calcified tissue international* **92,** 330–338 (2013).

[75] M. C. van der Meulen, X. Yang, T. G. Morgan, and M. P. Bostrom, "The effects of loading on cancellous bone in the rabbit," *Clinical orthopaedics and related research* **467,** 2000–2006 (2009).

[76] J. S. Nyman, M. Reyes, and X. Wang, "Effect of ultrastructural changes on the toughness of bone," *Micron (Oxford, England : 1993)* **36,** 566–582 (2005).

[77] L. Knott and A. J. Bailey, "Collagen cross-links in mineralizing tissues: a review of their chemistry, function, and clinical relevance," *Bone* **22,** 181–187 (1998).

[78] D. R. Sell and V. M. Monnier, "Structure elucidation of a senescence cross-link from human extracellular matrix. Implication of pentoses in the aging process," *The Journal of biological chemistry* **264,** 21597–21602 (1989).

[79] S. P. Robins, A. Duncan, N. Wilson, and B. J. Evans, "Standardization of pyridinium crosslinks, pyridinoline and deoxypyridinoline, for use as biochemical markers of collagen degradation," *Clinical chemistry* **42,** 1621–1626 (1996).

[80] D. R. Eyre, M. A. Paz, and P. M. Gallop, "Cross-linking in collagen and elastin," *Annual Review of Biochemistry* **53,** 717–748 (1984).

[81] E. P. Paschalis, E. Shane, G. Lyritis, G. Skarantavos, R. Mendelsohn, and A. L. Boskey, "Bone fragility and collagen cross-links," *Journal of bone and mineral research* **19,** 2000–2004 (2004).

[82] N. C. Avery and A. J. Bailey, "Enzymic and non-enzymic cross-linking mechanisms in relation to turnover of collagen: relevance to aging and exercise," *Scandinavian Journal of Medicine & Science in Sports* **15,** 231–240 (2005).

[83] M. J. Glimcher, "The nature of the mineral component of bone and the mechanism of calcification," *Instructional course lectures* **36,** 49–69 (1987).

[84] J. Mahamid, A. Sharir, L. Addadi, and S. Welner, "Amorphous calcium phosphate is a major component of the forming fin bones of zebrafish: Indications for an amorphous precursor phase," *PNAS* **105,** 12748–12753 (2008).

[85] J. Mahamid, B. Aichmayer, E. Shimoni, R. Ziblat, C. Li, S. Siegel, O. Paris, P. Fratzl, S. Weiner, and L. Addadi, "Mapping amorphous calcium phosphate transformation into crystalline mineral from the cell to the bone in zebrafish fin rays," *PNAS* **107,** 6316–6321 (2010).

[86] A. Boskey, "Bone mineral crystal size," *Osteoporosis international* **14 Suppl 5,** S16–20; discussion S20–1 (2003).

[87] R. G. Handschin and B. Stern, "X-Ray Diffraction Studies on the Lattice Perfection of Human Bone Apatite (Crista Iliaca)," *Bone* **16,** 355S–363S (1995).

[88] B. Wopenka and J. D. Pasteris, "A mineralogical perspective on the apatite in bone," *Materials Science and Engineering C* **25,** 131–143 (2005).

[89] C. Rey, B. Collins, T. Goehl, I. R. Dickson, and M. J. Glimcher, "The carbonate environment in bone mineral: a resolution-enhanced Fourier Transform Infrared Spectroscopy Study," *Calcified tissue international* **45,** 157–164 (1989).

[90] D. Faibish, S. M. Ott, and A. L. Boskey, "Mineral changes in osteoporosis: a review," *Clinical orthopaedics and related research* **443,** 28–38 (2006).

[91] B. R. McCreadie, M. D. Morris, T. C. Chen, D. S. Rao, W. F. Finney, E. Widjaja, and S. A. Goldstein, "Bone tissue compositional differences in women with and without osteoporotic fracture," *Bone* **39,** 1190–1195 (2006).

[92] H. Isaksson, M. J. Turunen, L. Rieppo, S. Saarakkala, I. S. Tamminen, J. Rieppo, H. Kröger, and J. S. Jurvelin, "Infrared spectroscopy indicates altered bone turnover and remodeling activity in renal osteodystrophy," *Journal of bone and mineral research* **25,** 1360–1366 (2010).

[93] D. B. Burr, "The contribution of the organic matrix to bone's material properties," *Bone* **31,** 8–11 (2002).

[94] X. Wang, R. A. Bank, J. M. TeKoppele, and C. M. Agrawal, "The role of collagen in determining bone mechanical properties," *Journal of orthopaedic research* **19,** 1021–1026 (2001).

[95] X. Wang, X. Shen, X. Li, and C. M. Agrawal, "Age-related changes in the collagen network and toughness of bone," *Bone* **31,** 1–7 (2002).

[96] H. Isaksson, V. Tolvanen, M. A. Finnilä, J. Iivarinen, J. Tuukkanen, K. Seppänen, J. P. Arokoski, P. A. Brama, J. S. Jurvelin, and H. J. Helminen, "Physical exercise improves properties of bone and its collagen network in growing and maturing mice," *Calcified tissue international* **85,** 247–256 (2009).

[97] B. Preininger, S. Checa, F. L. Molnar, P. Fratzl, G. N. Duda, and K. Raum, "Spatial-temporal mapping of bone structural and elastic properties in a sheep model following osteotomy," *Ultrasound in medicine & biology* **37,** 474–483 (2011).

[98] S. Govender, C. Csimma, H. K. Genant, A. Valentin-Opran, Y. Amit, R. Arbel, H. Aro, D. Atar, M. Bishay, M. G. Borner, P. Chiron, P. Choong, J. Cinats, B. Courtenay, R. Feibel, B. Geulette, C. Gravel, N. Haas, M. Raschke, E. Hammacher, D. van der Velde, P. Hardy, M. Holt, C. Josten, R. L. Ketterl, B. Lindeque, G. Lob, H. Mathevon, G. McCoy, D. Marsh, R. Miller, E. Munting, S. Oevre, L. Nordsletten, A. Patel, A. Pohl, W. Rennie, P. Reynders, P. M. Rommens, J. Rondia, W. C. Rossouw, P. J. Daneel, S. Ruff, A. Ruter, S. Santavirta, T. A. Schildhauer, C. Gekle, R. Schnettler, D. Segal, H. Seiler, R. B. Snowdowne, J. Stapert, G. Taglang, R. Verdonk, L. Vogels, A. Weckbach, A. Wentzensen, T. Wisniewski, and B.-. E. in Surgery for Tibial Trauma (BESTT) Study Group, "Recombinant human bone morphogenetic protein-2 for treatment of open tibial fractures: a prospective, controlled, randomized study of four hundred and fifty patients," *The Journal of bone and joint surgery.American volume* **84-A,** 2123–2134 (2002).

[99] T. J. Blokhuis, P. Buma, N. Verdonschot, M. Gotthardt, and T. Hendriks, "BMP-7 stimulates early diaphyseal fracture healing in estrogen deficient rats," *Journal of orthopaedic research* **30,** 720–725 (2012).

[100] C. J. Hernandez and T. M. Keaveny, "A biomechanical perspective on bone quality," *Bone* **39,** 1173–1181 (2006).

[101] E. Donnelly, "Methods for assessing bone quality: a review," *Clinical orthopaedics and related research* **469,** 2128–2138 (2011).

[102] D. Chappard, M. F. Basle, E. Legrand, and M. Audran, "New laboratory tools in the assessment of bone quality," *Osteoporosis international* **22,** 2225–2240 (2011).

[103] D. R. Eyre, T. J. Koob, and K. P. V. Ness, "Quantitation of hydroxypyridinium crosslinks in collagen by high-performance liquid chromatography," *Analytical Biochemistry* **137,** 380–388 (1984).

[104] M. Yamauchi, G. S. Chandler, H. Tanzawa, and E. P. Katz, "Cross-linking and the molecular packing of corneal collagen," *Biochemical and biophysical research communications* **219,** 311–315 (1996).

[105] B. Stuart, *Infrared spectroscopy: fundamentals and applications* (J. Wiley, Chichester, West Sussex, England, 2004).

[106] D. A. Long, *Raman spectroscopy* (McGraw-Hill International Book Company, Maidenhead, Great-Britain, 1977).

[107] H. D. Young and R. A. Freedman, *University physics with modern physics*, 11 ed. (Addison-Wesley, San Francisco, California, USA, 2004).

[108] Z. Movasaghi, S. Rehman, and I. Rehman, "Fourier Transform Infrared (FTIR) Spectroscopy of Biological Tissues," *Applied Spectroscopy Reviews* **43(2),** 134–179 (2008).

[109] Y. Kobrina, H. Isaksson, M. Sinisaari, L. Rieppo, P. A. Brama, R. van Weeren, H. J. Helminen, J. S. Jurvelin, and S. Saarakkala, "Infrared spectroscopy reveals both qualitative and quantitative differences in equine subchondral bone during maturation," *Journal of Biomedical Optics* **15,** 067003 (2010).

[110] C. Rey, M. Shimizu, B. Collins, and M. J. Glimcher, "Resolution-enhanced Fourier transform infrared spectroscopy study of the environment of phosphate ions in the early deposits of a solid phase of calcium-phosphate in bone and enamel, and their evolution with age. I: Investigations in theν_3PO_4 domain," *Calcified tissue international* **46,** 384–394 (1990).

[111] Y. Kobrina, M. J. Turunen, S. Saarakkala, J. S. Jurvelin, M. Hauta-Kasari, and H. Isaksson, "Cluster analysis of infrared spectra of rabbit cortical bone samples during maturation and growth," *The Analyst* **135,** 3147–3155 (2010).

[112] M. E. Ruppel, D. B. Burr, and L. M. Miller, "Chemical makeup of microdamaged bone differs from undamaged bone," *Bone* **39,** 318–324 (2006).

[113] H. Ouyang, P. J. Sherman, E. P. Paschalis, A. L. Boskey, and R. Mendelsohn, "Fourier transform infrared microscopic imaging: effects of estrogen and estrogen deficiency on fracture healing in rat femurs," *Applied Spectroscopy* **58,** 1–9 (2004).

[114] X. Yang, B. F. Ricciardi, A. Hernandez-Soria, Y. Shi, N. Pleshko Camacho, and M. P. Bostrom, "Callus mineralization and maturation are delayed during fracture healing in interleukin-6 knockout mice," *Bone* **41,** 928–936 (2007).

[115] D. Faibish, A. Gomes, G. Boivin, I. Binderman, and A. Boskey, "Infrared imaging of calcified tissue in bone biopsies from adults with osteomalacia," *Bone* **36,** 6–12 (2005).

[116] A. Boskey and R. Mendelsohn, "Infrared analysis of bone in health and disease," *Journal of Biomedical Optics* **10,** 031102 (2005).

[117] A. L. Boskey, E. DiCarlo, E. Paschalis, P. West, and R. Mendelsohn, "Comparison of mineral quality and quantity in iliac crest biopsies from high- and low-turnover osteoporosis: an FT-IR microspectroscopic investigation," *Osteoporosis international* **16,** 2031–2038 (2005).

[118] N. Pleshko Camacho, W. J. Landis, and A. L. Boskey, "Mineral changes in a mouse model of osteogenesis imperfecta detected by Fourier transform infrared microscopy," *Connective tissue research* **35,** 259–265 (1996).

[119] J. C. Burket, D. J. Brooks, J. M. MacLeay, S. P. Baker, A. L. Boskey, and M. C. van der Meulen, "Variations in nanomechanical properties and tissue composition within trabeculae from an ovine model of osteoporosis and treatment," *Bone* **52,** 326–336 (2013).

[120] A. L. Boskey, L. Spevak, and R. S. Weinstein, "Spectroscopic markers of bone quality in alendronate-treated postmenopausal women," *Osteoporosis international* **20,** 793–800 (2009).

[121] S. J. Gadeleta, A. L. Boskey, E. Paschalis, C. Carlson, F. Menschik, T. Baldini, M. Peterson, and C. M. Rimnac, "A physical, chemical, and mechanical study of lumbar vertebrae from normal, ovariectomized, and nandrolone decanoate-treated cynomolgus monkeys (Macaca fascicularis)," *Bone* **27,** 541–550 (2000).

[122] E. P. Paschalis, A. L. Boskey, M. Kassem, and E. F. Eriksen, "Effect of hormone replacement therapy on bone quality in early postmenopausal women," *Journal of bone and mineral research* **18,** 955–959 (2003).

[123] E. Donnelly, D. X. Chen, A. L. Boskey, S. P. Baker, and M. C. van der Meulen, "Contribution of mineral to bone structural behavior and tissue mechanical properties," *Calcified tissue international* **87,** 450–460 (2010).

[124] E. P. Paschalis, R. Mendelsohn, and A. L. Boskey, "Infrared assessment of bone quality: a review," *Clinical orthopaedics and related research* **469,** 2170–2178 (2011).

[125] L. M. Miller, V. Vairavamurthy, M. R. Chance, R. Mendelsohn, E. P. Paschalis, F. Betts, and A. L. Boskey, "In situ analysis of mineral content and crystallinity in bone using infrared micro-spectroscopy of the nu(4) PO(4)(3-) vibration," *Biochimica et biophysica acta* **1527,** 11–19 (2001).

[126] J. E. Roberts, L. C. Bonar, R. G. Griffin, and M. J. Glimcher, "Characterization of very young mineral phases of bone by solid state ^{3}1phosphorus magic angle sample spinning nuclear magnetic resonance and X-ray diffraction," *Calcified tissue international* **50,** 42–48 (1992).

[127] H. Boyer and J. Oswalt, "Dispersive Raman microscopy," *Analusis* **28(1),** 3–10 (2000).

[128] H. Gremlich and B. Yan, *Infrared and Raman spectroscopy of biological materials* (Marcel Dekker, New York, NY, USA, 2001).

[129] Y. Iwasaki, J. J. Kazama, H. Yamato, and M. Fukagawa, "Changes in chemical composition of cortical bone associated with bone fragility in rat model with chronic kidney disease," *Bone* **48,** 1260–1267 (2011).

[130] J. Shen, L. Fan, J. Yang, A. G. Shen, and J. M. Hu, "A longitudinal Raman microspectroscopic study of osteoporosis induced by spinal cord injury," *Osteoporosis international* **21,** 81–87 (2010).

[131] E. R. Draper, M. D. Morris, N. Pleshko Camacho, P. Matousek, M. Towrie, A. W. Parker, and A. E. Goodship, "Novel assessment of bone using time-resolved transcutaneous Raman spectroscopy," *Journal of bone and mineral research* **20,** 1968–1972 (2005).

[132] J. S. Yerramshetty and O. Akkus, "The associations between mineral crystallinity and the mechanical properties of human cortical bone," *Bone* **42,** 476–482 (2008).

[133] A. Carden, R. M. Rajachar, M. D. Morris, and D. H. Kohn, "Ultrastructural changes accompanying the mechanical deformation of bone tissue: a Raman imaging study," *Calcified tissue international* **72,** 166–175 (2003).

[134] J. A. Timlin, A. Carden, and M. D. Morris, "Chemical Microstructure of Cortical Bone Probed by Raman Transects," *Applied spectroscopy* **53,** 1429–1435 (1999).

[135] B. G. Frushour and J. L. Koenig, "Raman scattering of collagen, gelatin, and elastin," *Biopolymers* **14,** 379–391 (1975).

[136] A. G. Walton, M. J. Deveney, and J. L. Koenig, "Raman spectroscopy of calcified tissue," *Calcified tissue research* **6,** 162–167 (1970).

[137] S. R. Goodyear, I. R. Gibson, J. M. Skakle, R. P. Wells, and R. M. Aspden, "A comparison of cortical and trabecular bone from C57 Black 6 mice using Raman spectroscopy," *Bone* **44,** 899–907 (2009).

[138] G. Penel, G. Leroy, C. Rey, and E. Bres, "MicroRaman spectral study of the PO_4 and CO_3 vibrational modes in synthetic and biological apatites," *Calcified tissue international* **63,** 475–481 (1998).

[139] A. Awonusi, M. D. Morris, and M. M. Tecklenburg, "Carbonate assignment and calibration in the Raman spectrum of apatite," *Calcified tissue international* **81,** 46–52 (2007).

[140] M. Raghavan, N. D. Sahar, R. H. Wilson, M. A. Mycek, N. Pleshko, D. H. Kohn, and M. D. Morris, "Quantitative polarized Raman spectroscopy in highly turbid bone tissue," *Journal of Biomedical Optics* **15,** 037001 (2010).

[141] E. Collett, *Polarized light: Fundamentals and applications* (Marcel Dekker, New York, 1992).

[142] J. Rieppo, M. M. Hyttinen, E. Halmesmäki, H. Ruotsalainen, A. Vasara, I. Kiviranta, J. S. Jurvelin, and H. J. Helminen, "Changes in spatial collagen content and collagen network architecture in porcine articular cartilage during growth and maturation," *Osteoarthritis and cartilage* **17,** 448–455 (2009).

[143] A. Basillais, S. Bensamoun, C. Chappard, B. Brunet-Imbault, G. Lemineur, B. Ilharreborde, M. C. H. B. Tho, and C. L. Benhamou, "Three-dimensional characterization of cortical bone microstructure by microcomputed tomography: validation with ultrasonic and microscopic measurements," *Journal of orthopaedic science* **12,** 141–148 (2007).

[144] F. Particelli, L. Mecozzi, A. Beraudi, M. Montesi, F. Baruffaldi, and M. Viceconti, "A comparison between micro-CT and histology for the evaluation of cortical bone: effect of polymethylmethacrylate embedding on structural parameters," *Journal of microscopy* **245,** 302–310 (2012).

[145] W. A. Kalender, *Computed Tomography; Fundamentals, System Technology, Image Quality Applications*, 3 ed. (Publicis Publishing, Erlangen, 2011).

[146] O. Glatter and O. Kratky, *Small Angle X-ray Scattering* (Academic Press, London, 1982).

[147] P. Fratzl, M. Groschner, G. Vogl, H. P. Jr, J. Eschberger, N. Fratzl-Zelman, K. Koller, and K. Klaushofer, "Mineral crystals in calcified tissues: a comparative study by SAXS," *Journal of bone and mineral research* **7,** 329–334 (1992).

[148] N. Pleshko Camacho, S. Rinnerthaler, E. P. Paschalis, R. Mendelsohn, A. L. Boskey, and P. Fratzl, "Complementary information on bone ultrastructure from scanning small angle X-ray scattering and Fourier-transform infrared microspectroscopy," *Bone* **25,** 287–293 (1999).

[149] P. Fratzl, S. Schreiber, P. Roschger, M. H. Lafage, G. Rodan, and K. Klaushofer, "Effects of sodium fluoride and alendronate on the bone mineral in minipigs: a small-angle X-ray scattering and backscattered electron imaging study," *Journal of bone and mineral research* **11,** 248–253 (1996).

[150] Y. Liu, I. Manjubala, P. Roschger, H. Schell, G. N. Duda, and P. Fratzl, "Mineral crystal alignment in mineralized fracture callus determined by 3D small-angle X-ray scattering," (2010).

[151] Y. Liu, I. Manjubala, H. Schell, D. R. Epari, P. Roschger, G. N. Duda, and P. Fratzl, "Size and habit of mineral particles in bone and mineralized callus during bone healing in sheep," *Journal of bone and mineral research* **25,** 2029–2038 (2010).

[152] H. Isaksson, T. Harjula, A. Koistinen, J. Iivarinen, K. Seppänen, J. P. Arokoski, P. A. Brama, J. S. Jurvelin, and H. J. Helminen, "Collagen and mineral deposition in rabbit cortical bone during maturation and growth: effects on tissue properties," *Journal of orthopaedic research* **28,** 1626–1633 (2010).

[153] M. Tägil, M. M. McDonald, A. Morse, L. Peacock, K. Mikulec, N. Amanat, C. Godfrey, and D. G. Little, "Intermittent PTH(1-34) does not increase union rates in open rat femoral fractures and exhibits attenuated anabolic effects compared to closed fractures," *Bone* **46,** 852–859 (2010).

[154] P. Bosemark, H. Isaksson, M. M. McDonald, D. G. Little, and M. Tägil, "Augmentation of autologous bone graft by a combination of Bone Morphogenic Protein and bisphosphonate increased both callus volume and strength," *Acta Orthopaedica* **84,** 106–111 (2013).

[155] J. Rieppo, M. M. Hyttinen, J. S. Jurvelin, and H. J. Helminen, "Reference sample method reduces the error caused by variable cryosection thickness in Fourier transform infrared imaging," *Applied Spectroscopy* **58,** 137–140 (2004).

[156] C. A. Lieber and A. Mahadevan-Jansen, "Automated method for subtraction of fluorescence from biological Raman spectra," *Applied Spectroscopy* **57,** 1363–1367 (2003).

[157] E. J. Miller, A. J. Narkates, and M. A. Niemann, "Amino acid analysis of collagen hydrolysates by reverse-phase high-performance liquid chromatography of 9-fluorenylmethyl chloroformate derivatives," *Analytical Biochemistry* **190,** 92–97 (1990).

[158] T. K. Langsjo, J. Rieppo, A. Pelttari, N. Oksala, V. Kovanen, and H. J. Helminen, "Collagenase-induced changes in articular cartilage as detected by electron-microscopic stereology, quantitative polarized light microscopy and biochemical assays," *Cells, tissues, organs* **172,** 265–275 (2002).

[159] A. Labrador, Y. Cerenius, C. Svensson, K. Theodor, and T. Plivelic, "The yellow minihutch for SAXS experiments at MAX IV Laboratory," *J. Phys.: Conf. Ser.* **In press** (2013).

[160] J. H. Steiger, "Tests for comparing elements of a correlation matrix," *Psychological Bulletin* **87(2),** 245–251 (1980).

[161] J. C. Lotz, E. J. Cheal, and W. C. Hayes, "Stress distributions within the proximal femur during gait and falls: implications for osteoporotic fracture," *Osteoporosis international* **5,** 252–261 (1995).

[162] V. L. Giddings, G. S. Beaupre, R. T. Whalen, and D. R. Carter, "Calcaneal loading during walking and running," *Medicine and science in sports and exercise* **32,** 627–634 (2000).

[163] T. Sugiyama, L. B. Meakin, W. J. Browne, G. L. Galea, J. S. Price, and L. E. Lanyon, "Bones' adaptive response to mechanical loading is essentially linear between the low strains associated with disuse and the high strains associated with the lamellar/woven bone transition," *Journal of bone and mineral research* **27,** 1784–1793 (2012).

[164] R. L. D. Souza, M. Matsuura, F. Eckstein, S. C. Rawlinson, L. E. Lanyon, and A. A. Pitsillides, "Non-invasive axial loading of mouse tibiae increases cortical bone formation and modifies trabecular organization: a new model to study cortical and cancellous compartments in a single loaded element," *Bone* **37,** 810–818 (2005).

[165] D. H. Kohn, N. D. Sahar, J. M. Wallace, K. Golcuk, and M. D. Morris, "Exercise alters mineral and matrix composition in the absence of adding new bone," *Cells, tissues, organs* **189,** 33–37 (2009).

[166] L. Rieppo, S. Saarakkala, T. Närhi, J. Holopainen, M. Lammi, H. J. Helminen, J. S. Jurvelin, and J. Rieppo, "Quantitative analysis of spatial proteoglycan content in articular cartilage with Fourier transform infrared imaging spectroscopy: Critical evaluation of analysis methods and specificity of the parameters," *Microscopy research and technique* **73,** 503–512 (2010).

[167] R. Oldenbourg, E. D. Salmon, and P. T. Tran, "Birefringence of single and bundled microtubules," *Biophysical journal* **74,** 645–654 (1998).

[168] K. Otsubo, E. P. Katz, G. L. Mechanic, and M. Yamauchi, "Cross-linking connectivity in bone collagen fibrils: the COOH-terminal locus of free aldehyde," *Biochemistry* **31,** 396–402 (1992).

[169] E. P. Paschalis, F. Betts, E. DiCarlo, R. Mendelsohn, and A. L. Boskey, "FTIR microspectroscopic analysis of human iliac crest biopsies from untreated osteoporotic bone," *Calcified tissue international* **61,** 487–492 (1997).

[170] M. Kazanci, H. D. Wagner, N. I. Manjubala, H. S. Gupta, E. Paschalis, P. Roschger, and P. Fratzl, "Raman imaging of two orthogonal planes within cortical bone," *Bone* **41,** 456–461 (2007).

[171] S. Gourion-Arsiquaud, D. Faibish, E. Myers, L. Spevak, J. Compston, A. Hodsman, E. Shane, R. R. Recker, E. R. Boskey, and A. L. Boskey, "Use of FTIR spectroscopic imaging to identify parameters associated with fragility fracture," *Journal of bone and mineral research* **24,** 1565–1571 (2009).

[172] M. Mathew and S. Takagi, "Structures of Biological Minerals in Dental Research," *J. Res. Natl. Inst. Stand. Technol.* **106,** 1035–1044 (2001).

[173] M. A. Brennan, J. P. Gleeson, M. Browne, F. J. O'Brien, P. J. Thurner, and L. M. McNamara, "Site specific increase in heterogeneity of trabecular bone tissue mineral during oestrogen deficiency," *European cells & materials* **21,** 396–406 (2011).

[174] K. Verdelis, Y. Ling, T. Sreenath, N. Haruyama, M. MacDougall, M. C. van der Meulen, L. Lukashova, L. Spevak, A. B. Kulkarni, and A. L. Boskey, "DSPP effects on in vivo bone mineralization," *Bone* **43,** 983–990 (2008).

[175] D. Farlay, M. E. Duclos, E. Gineyts, C. Bertholon, S. Viguet-Carrin, J. Nallala, G. D. Sockalingum, D. Bertrand, T. Roger, D. J. Hartmann, R. Chapurlat, and G. Boivin, "The ratio 1660/1690 cm(-1) measured by infrared microspectroscopy is not specific of enzymatic collagen cross-links in bone tissue," *PloS one* **6,** e28736 (2011).

[176] A. L. Boskey, S. Gadaleta, C. Gundberg, S. B. Doty, P. Ducy, and G. Karsenty, "Fourier transform infrared microspectroscopic analysis of bones of osteocalcin-deficient mice provides insight into the function of osteocalcin," *Bone* **23,** 187–196 (1998).

[177] F. Eker, X. Cao, L. Nafie, and R. Schweitzer-Stenner, "Tripeptides adopt stable structures in water. A combined polarized visible Raman, FTIR, and VCD spectroscopy study," *Journal of the American Chemical Society* **124,** 14330–14341 (2002).

[178] J. S. Singh, "FTIR and raman spectra compared with ab initio calculated frequency modes for 5-aminouracil," *Journal of Biological Physics* **34,** 569–576 (2008).

[179] T. Kiviniemi, E. Hulkko, T. Kiljunen, and M. Pettersson, "Iodine-benzene complex as a candidate for a real-time control of a bimolecular reaction. Spectroscopic studies of the properties of the 1:1 complex isolated in solid krypton," *The journal of physical chemistry.A* **113,** 6326–6333 (2009).

[180] B. Yan, H. Gremlich, S. Moss, G. M. Coppola, Q. Sun, and L. Liu, "A Comparison of Various FTIR and FT Raman Methods: Applications in the Reaction Optimization Stage of Combinatorial Chemistry," *Journal of combined chemistry* **1,** 46–54 (1999).

[181] D. G. Kim, G. T. Christopherson, X. N. Dong, D. P. Fyhrie, and Y. N. Yeni, "The effect of microcomputed tomography scanning and reconstruction voxel size on the accuracy of stereological measurements in human cancellous bone," *Bone* **35,** 1375–1382 (2004).

[182] M. Sode, A. J. Burghardt, R. A. Nissenson, and S. Majumdar, "Resolution dependence of the non-metric trabecular structure indices," *Bone* **42,** 728–736 (2008).

[183] M. Kothari, T. M. Keaveny, J. C. Lin, D. C. Newitt, H. K. Genant, and S. Majumdar, "Impact of spatial resolution on the prediction of trabecular architecture parameters," *Bone* **22,** 437–443 (1998).

[184] A. Odgaard, J. Kabel, B. van Rietbergen, M. Dalstra, and R. Huiskes, "Fabric and elastic principal directions of cancellous bone are closely related," *Journal of Biomechanics* **30,** 487–495 (1997).

[185] T. P. Harrigan and R. W. Mann, "Characterization of microstructural anisotropy in orthotropic materials using a second rank tensor," *Journal of material science* **19,** 761–767 (1984).

[186] A. Odgaard, E. B. Jensen, and H. J. Gundersen, "Estimation of structural anisotropy based on volume orientation. A new concept," *Journal of microscopy* **157,** 149–162 (1990).

[187] A. Märten, P. Fratzl, O. Paris, and P. Zaslansky, "On the mineral in collagen of human crown dentine," *Biomaterials* **31,** 5479–5490 (2010).

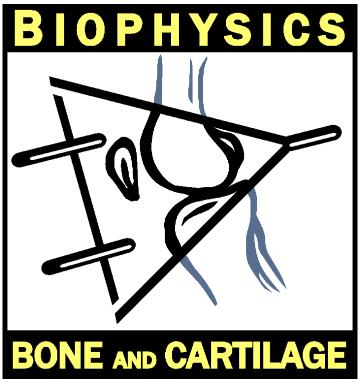

MIKAEL TURUNEN

Spectroscopic Characterization of Bone Composition

Alterations during Bone Formation, Maturation and Aging

Bone composition and architecture constantly change, especially during the process of bone maturation, aging and under altered mechanical loading. Thus, bone is a dynamic tissue with continuous changes in its quality. In this thesis, these changes were evaluated by using several quantitative techniques, *e.g.* Fourier transform infrared and Raman microspectroscopy, polarized light microscopy, micro computed tomography and small angle x-ray scattering. The methods can be used to improve the assessment of bone quality in the future and increase the understanding of characteristics of bone diseases, *e.g.* osteoporosis.

UNIVERSITY OF
EASTERN FINLAND

PUBLICATIONS OF THE UNIVERSITY OF EASTERN FINLAND
Dissertations in Forestry and Natural Sciences

ISBN 978-952-61-1194-0